Analytical Development and Application of Optical Microcavities

By

Sarah M. Wildgen

Submitted to the graduate degree program in Chemistry and the Graduate Faculty of the University of Kansas in partial fulfillment of the requirements for the degree of Doctor of Philosophy.

_____

Chairperson: Dr. Robert C. Dunn

_____

Dr. Cindy Berrie

_____

Dr. Susan Lunte

_____

Dr. Heather Desaire

_____

Dr. Rongqing Hui

Date Defended: September 16th, 2015

The Dissertation Committee for Sarah M. Wildgen

certifies that this is the approved version of the following dissertation:

Analytical Development and Application of Optical Microcavities

_____

Chairperson: Dr. Robert C. Dunn

Date approved: September 16th, 2015

Abstract

Optical microcavities are desirable label-free sensors due to their sensitive detection capabilities. In particular, microsphere resonators achieve high sensitives by confining and recirculating light within their spherical cavity. Recirculation of light within these small, compact resonators amplifies sample-light interactions, contributing to improved sensing performance. By taking advantage of their desirable performance metrics, we have developed a variety of innovative label-free analytical platforms. For label-free biosensing, we have integrated whispering gallery mode (WGM) resonators with fluorescence imaging for the simultaneous analysis of multiple microspheres. Using this approach, we have demonstrated multiplexed detection of protein biomarkers.

Current clinical tools used to diagnose ovarian cancer lack specificity and sensitivity required to achieve an accurate early diagnosis. Label-free platforms provide an opportunity to detect identified protein and non-protein disease biomarkers in order to improve diagnostic capabilities. Whispering gallery mode resonators offer a sensitive, multiplexed detection scheme to accomplish this. Specifically, our developed imaging approach allows multiple targets to be analyzed in a single assay by simultaneously monitoring WGM resonances of numerous microspheres. Microsphere resonators of particular sizes are functionalized for the detection of specific biomarkers. Putative ovarian cancer biomarkers CA-125, osteopontin, and prolactin were simultaneously quantified using WGM imaging. Additionally, the label-free platform was utilized for the detection of non-protein ovarian cancer target microRNA miR-142-3p.

For biosensing applications, the small, compact size of microsphere resonators is also advantageous for integration with small volume systems. We demonstrate the incorporation of hundreds of WGM resonators in a 10 μL droplet. By incorporating WGM resonators in small volume systems, such as microfluidic platforms, on-chip detection capabilities can be improved. In particular, digital microfluidic systems provide an analytical tool for precise control of discrete volume droplets, improving assay fluidics. In order to integrate WGM resonators with these small volume droplet systems, initial studies demonstrate real-time WGM detection in 10 μL droplets. After determining evaporation was not an

interferent, picomolar protein concentrations were measured by WGM resonators. Ultimately, these measurements can be extended to improve on-chip multiplexed immunoassay capabilities.

To further explore WGM sensing applications, we developed a new analytical technique for label-free analysis of surfaces. Scanning resonator microscopy (SRM) utilizes a modified probe tip to analyze optical and topographic surface features. This novel scanning probe technique provides a label-free, non-invasive approach to investigate a variety of sample types. For material science applications, we demonstrate analysis of thin polymer films patterned by UV light using SRM. Additionally, we are interested in extending SRM measurements for the investigation of biological samples. Scanning resonator microscopy provides a label-free technique to measure protein coated surfaces, such as protein microarrays. Furthermore, for cell-based assays, label-free approaches allow for real time analysis of native biological systems. Initial investigations indicate SRM is a promising analytical tool for improving pre-clinical analysis methods for drug development and for applications in clinical diagnostics. Overall, WGM resonators are demonstrated as sensitive label-free detectors for the development of a variety of analytical tools.

Acknowledgements

When I first started graduate school, I had no idea what challenges and accomplishments lied ahead. The past five years have included numerous significant events which I could not have taken on without the support and encouragement of many individuals. From my high school friends who were always willing to catch up over coffee, to the always helpful Chemistry Department staff, I am thankful to so many people for their assistance, kindness and support throughout my graduate school experience. I'd like to briefly acknowledge some key individuals who were instrumental to my graduate school career.

During my graduate career, my mentor Dr. Bob Dunn provided continuous support and encouragement while challenging me to expand my knowledge and scientific abilities. His guidance has allowed me to gain valuable problem solving skills and enabled me to succeed as a scientist and as a professional. As a "Type A", I appreciate Dr. Dunn's lightheartedness and enthusiasm for science and new ideas. He always reminded me not to get lost in the details and to think about the big picture. I truly have had a great experience in the Dunn lab and have been honored to learn from, work with and get to know Dr. Dunn and his family. He has been, and will continue to be, a great mentor, teacher and friend.

For the past four years, I have been fortunate to be supported by the Madison and Lila Self Graduate Fellowship. I am extremely grateful for the financial support, training and educational opportunities I was privileged to experience as a Fellow. I am very thankful to Al and Lila Self for their generous financial support and vision for young students. Their passion for education and science is truly inspiring and something I will always be grateful for. The skills I have learned and strengthened as a Fellow will be extremely useful to me in my career and I am very thankful for the numerous unique experiences I had throughout my four years in the Fellowship program. I have enjoyed working with and learning from my fellowship classmates as well as the many other fellows in the program. Additionally, I appreciate the support and encouragement from Dean Roberts and both current and past fellowship staff members including Cathy Dwigans, Stefani Buchwitz, Patty Dannenberg, and Sharon Graham.

I would also like to thank all current and past members of the Dunn lab. I am very thankful and appreciative for the help, guidance and friendship of Dr. Heath Huckabay. He was patient and willing to

train me in the lab prior to his graduation. I appreciate his help while I got established as a member of the Dunn lab. I would like to thank Daniel Kim for his willingness to have scientific discussions, brainstorming sessions and for always being willing to help me with LabView and computer issues. It has been a pleasure to work with you in the lab on our whispering gallery mode projects. Additionally, I would like to thank lab members Lin Zeng and Judith Flores who have been positive and supportive members of our lab. Judith Flores was a productive and motivated summer REU student who assisted with fabricating and characterizing new resonators.

I could not have survived graduate school without the endless support of my friends and family. Thank you to Rachel Saylor for your support as a friend and colleague. Since day one, we have challenged each other in classes and our research which I think has only helped us to be better scientists. Your listening ear and helpful advice has gotten me though many rough days in the lab, which I am very grateful for.

Living in Lawrence during the last five years has allowed me to create great memories with my family. My family in Lawrence, including my sister, cousins, aunt and uncle, have been instrumental in providing support and much needed lab breaks. Thank you to my in-laws and nephews who have all been a great support system and a wonderful distraction throughout graduate school. To my parents, thank you for guiding and raising me to be curious, creative and scholastic. Your support and guidance has been instrumental in helping me set and achieve my goals. Last but not least, I would like to thank my husband for his constant love and support. You have seen my good days and my not so good days, and always remind me to not sweat the small stuff. I am so appreciative of your unconditional support and love. Thank you for being by my side throughout this experience and I cannot wait to start our next adventure together.

Table of Contents

Chapter 1: Introduction and Overview 1

1.1 Ovarian Cancer 1

1.2 Ovarian Cancer Diagnostic Methods 2

1.2.1 Tissue Biopsy 3

1.2.2 Diagnostic Imaging 3

1.2.3 Cancer Antigen 125 (CA-125) Blood Test 3

1.2.4 Limitations of Current Diagnostic Methods 4

1.2.5 Desired Performance Metrics for an Ovarian Cancer Screening Test 5

1.3 Ovarian Cancer Biomarkers 6

1.3.1 Ovarian Cancer Protein Biomarker Panels 8

1.3.2 MicroRNA as Promising Non-Protein Ovarian Cancer Biomarkers 10

1.4 Enzyme-Linked Immunosorbent Assay (ELISA) 11

1.5 Label-Free Biosensing Platforms 13

1.5.1 Electrochemical-Based Label-Free Biosensors 14

1.5.2 Mechanical-Based Label-Free Biosensors 15

1.5.3 Optical-Based Label-Free Biosensors 15

1.6 Motivation of Dissertation 17

1.7 References 18

Chapter 2: Whispering Gallery Mode Resonators for Label-Free Biosensing 23

2.1 Introduction 23

2.1.1 Total Internal Reflection and the Evanescent Wave 24

2.2 Whispering Gallery Mode Resonators 26

2.2.1 Whispering Gallery Mode Resonators for Biosensing *29*

2.3 Performance Metrics of Whispering Gallery Mode Resonators 30

2.3.1 Quality Factor *30*

2.3.2 Effective Path Length *31*

2.3.3 Mode Volume *32*

2.3.4 Finesse *33*

2.4 Implementation and Application of High-Q Whispering Gallery Mode Resonators 34

2.4.1 Liquid Core Optical Ring Resonators (LCORR) *35*

2.4.2 Microtoroid Resonators *36*

2.4.3 Planar Ring Resonators *36*

2.4.4 Microspheres *37*

2.5 Opportunities for Microsphere Whispering Gallery Mode Resonators 37

2.6 Overview of Dissertation 39

2.7 References 41

Chapter 3: Whispering Gallery Mode Imaging for the Multiplexed Detection of Putative Ovarian Cancer Biomarkers 43

3.1 Introduction 43

3.1.1 Development of Whispering Gallery Mode Imaging *44*

3.2 Materials and Methods 48

3.2.1 Materials *48*

3.2.2 Preparation of Microsphere WGM Sensors *49*

3.2.3 WGM Imaging Measurements *49*

3.3 Results and Discussion 50

3.3.1 Label-Free Sensing Using Whispering Gallery Mode (WGM) Imaging *50*

3.3.2 WGM Imaging for the Detection of Ovarian Cancer Biomarkers *53*

3.3.3 WGM Imaging for Multiplexed Detection of Putative Ovarian Cancer Biomarkers *56*

3.3.4 WGM Imaging for the Detection of MicroRNA *61*

3.4 Future Directions 65

3.4.1 Imaging Whispering Gallery Mode Structure *65*

3.4.2 Challenges of Fluorescence Imaging of Whispering Gallery Mode Resonances *66*

3.5 Conclusions 67

3.6 References 68

Chapter 4: Investigation of Whispering Gallery Mode Resonators as Rapid, Label-Free Sensors in Small Volume Systems 71

4.1 Introduction 71

4.1.1 Utilizing Whispering Gallery Mode Resonators in Small Volume Platforms *72*

4.1.2 Advantages of Whispering Gallery Mode Resonators as Detectors in Small Volume Systems . *73*

4.2 Materials and Methods 75

4.2.1 Materials *75*

4.2.2 Experimental Set-Up and Measurements *75*

4.2.3 Preparing Hydrophobic Surfaces *76*

4.2.4 Evanescently Scattered Light for WGM Imaging *77*

4.2.5 Refractive Index Assays *78*

4.2.6 Microsphere Functionalization *78*

4.2.7 Bioassay Protocol *79*

4.3 Results and Discussion 79

4.3.1 Analysis of Hydrophobic Surfaces *80*

4.3.2 Small Volume Droplet Set-Up *81*

4.3.3 Droplet Evaporation *82*

4.3.4 Real-Time Analysis of WGM Resonators *85*

4.3.5 Investigating Droplet Mixing: Convective versus Active *88*

4.3.6 Refractive Index Calibration *89*

4.3.7 Microsphere Functionalization for Biosensing *90*

4.3.8 Initial Binding Rates *92*

4.4 Future Directions 94

4.4.1 Multiplexed Immunoassays in Small Volume Droplets *94*

4.5 Conclusions 97

4.6 References 98

Chapter 5: Advantages and Opportunities of Whispering Gallery Mode Microsphere Resonators 101

5.1 Introduction 101

5.1.1 Advantages of Whispering Gallery Mode Imaging *101*

5.1.2 Microsphere Whispering Gallery Mode Resonators *103*

5.2 Materials and Methods 104

5.2.1 Materials *104*

5.2.2 Preparation of Microspheres *104*

5.2.3 Whispering Gallery Mode Imaging Set-Up *105*

5.2.4 Refractive Index Assays *106*

5.3 Results and Discussion 106

5.3.1 Characterization of Barium Titanate Microsphere Resonators *106*

5.3.2 Characterization of Fiber Microsphere Resonators *109*

5.4 Conclusions 112

5.5 References 114

Chapter 6: Development of Scanning Resonator Microscopy 115

6.1 Introduction 115

6.1.1 Scanning Probe Microscopy *116*

6.1.2 Atomic Force Microscopy *116*

6.1.3 Hyphenated AFM Techniques *118*

6.1.4 Scanning Resonator Microscopy *119*

6.1.5 Scanning Resonator Microscopy for Material Characterization *120*

6.2 Materials and Methods 121

6.2.1 Materials *121*

6.2.2 Tip Modification *122*

6.2.3 Scanning Resonator Microscopy Instrumentation *123*

6.2.4 Scanning Resonator Microscopy Measurements *125*

6.2.5 Sample Preparation *125*

6.2.5.1 Ultrathin Material Samples 125

6.2.5.2 Positive Photoresist AZ 1518 126

6.2.5.3 Amorphous Fluoropolymer Teflon AF 127

6.2.5.4 Graphene Oxide Thin Films 127

6.2.5.5 Photoreactive Polymer PE-DR 19 128

6.3 Results and Discussion 128

6.3.1 Initial Scanning Resonator Microscopy Imaging 131

6.3.2 Ultrathin Material Samples 133

6.3.3 Positive Photoresist AZ 1518 135

6.3.4 Amorphous Fluoropolymer Teflon AF 138

6.3.5 Analysis of Graphene Oxide Thin Film 140

6.4 Future Directions 143

6.4.1 Azobenzene Polymers 144

6.5 Conclusions 146

6.6 References 148

Chapter 7: Towards Investigating Biological Samples Using Scanning Resonator Microscopy 152

7.1 Introduction 152

7.1.1 Protein Microarrays 153

7.1.2 Model Membranes for the Investigation of Membrane Structure and Organization 154

7.2 Materials and Methods 155

7.2.1 Materials 155

7.2.2 Protein Coated Surfaces 155

7.2.3 Sphingomyelin and Cholesterol Monolayers 156

7.3 Results and Discussion 156

7.3.1 Investigations of Protein Coated Surfaces 156

7.3.2 Investigation of Fluorinated Cholesterol as a Probe for Membrane Organization 158

7.4 Future Directions 163

7.4.1 Cell-Based Assays 163

7.4.2 Fiber Microsphere Resonators for Improved Sensing Capabilities 164

7.4.3 Further Optimization of Scanning Resonator Microscopy 166

7.5 Conclusions 167

7.6 Summary 167

7.7 References 169

Chapter 8 Appendix: Data Analysis, Instrumentation, and Detailed Procedures 171

8.1 Functionalization of Barium Titanate Microspheres 171

8.2 Data Analysis Methods and Techniques 173

8.2.1 Transferring NanoScope Files for Analysis in Excel 173

8.2.2 Analyzing Multiple Resonators Using Image J 174

List of Figures

Figure 1.1: Ovarian Cancer Statistics……...…….2

Figure 1.2: Sandwich ELISA……...12

Figure 2.1: Snell's Law and Total Internal Reflection…….25

Figure 2.2: Total Internal Reflection and the Evanescent Wave…….26

Figure 2.3: Whispering Gallery Mode Resonator……27

Figure 2.4: Transmission Measurements of Resonators……..28

Figure 2.5: Whispering Gallery Mode Resonators for Biosensing……..29

Figure 2.6: Mode Volume……33

Figure 2.7: Geometries of Whispering Gallery Mode Resonators……...34

Figure 2.8: Whispering Gallery Mode Imaging……...38

Figure 3.1: Fluorescence Imaging of Whispering Gallery Mode Resonators……..44

Figure 3.2: Schematic of Whispering Gallery Mode Imaging…….46

Figure 3.3: Analysis of Whispering Gallery Mode Imaging……...47

Figure 3.4: Response to Solution Refractive Index Changes……...51

Figure 3.5: Calibration of Resonant Wavelength and Solution Refractive Index……...52

Figure 3.6: Functionalized Resonators for Protein Detection……..53

Figure 3.7: Detection of CA-125 in Serum……..54

Figure 3.8: Detection of CA-125 in Serum Samples……...55

Figure 3.9: Whispering Gallery Mode Imaging Multiplexed Detection……..57

Figure 3.10: Determination of Cross Reactivity……..59

Figure 3.11: Multiplexed Detection of Putative Ovarian Cancer Biomarkers…….60

Figure 3.12: Functionalized Resonators for MicorRNA Detection…….62

Figure 3.13: Detection of microRNA miR-142-3p…… ……...63

Figure 3.14: Calibration of Resonant Wavelength and microRNA miR-142-3p Concentration…...……..64

Figure 3.15: Fluorescence Image of a Whispering Gallery Mode ……..65

Figure 3.16: Mode Structure Changes with Refractive Index……66

Figure 4.1: Digital Microfluidic Home Built System……..72

Figure 4.2: Surface Droplets Using Teflon Tape……76

Figure 4.3: Water Droplet on a Hydrophobic Surface……77

Figure 4.4: Characterization of Droplet Properties and Contact Angles……81

Figure 4.5: Small Volume Droplet Schematic……82

Figure 4.6: Droplet Evaporation in Air……84

Figure 4.7: Waterfall Plot of Resonator Response to Refractive Index Changes……86

Figure 4.8: Analysis of Droplet Volume……..87

Figure 4.9: Analysis of Active Mixing in Droplets……88

Figure 4.10: Small Volume Refractive Index Calibration……...89

Figure 4.11: Optimization of Surface Functionalization Methods……..91

Figure 4.12: Real-Time Detection of Protein Binding……93

Figure 4.13: Initial Results of IL-6 and IL-10 Protein Binding……...…95

Figure 4.14: Dialysis of IL-10 Stock Solutions……...96

Figure 5.1: Fabrication of Fiber Microsphere……105

Figure 5.2: Range of Q-Factors for Barium Titanate Microspheres……..107

Figure 5.3: Range of Refractive Index Sensitivities for Barium Titanate Microspheres……..……108

Figure 5.4: Q-Factor as a Function of Sensitivity……..109

Figure 5.5: Q-Factor Comparison of Fiber and Barium Titanate Microsphere ……110

Figure 5.6: Q-Factor Comparison of Fiber Microsphere in Air and Water……..…111

Figure 5.7: Resonant Wavelength Shifts and Calibration of Refractive Index Changes……..112

Figure 6.1: Schematic of Atomic Force Microscopy……117

Figure 6.2: Modified Scanning Resonator Microscopy Tip……..123

Figure 6.3: Schematic of Scanning Resonator Microscopy……...124

Figure 6.4: Preparation of Ultra-Thin Samples……..126

Figure 6.5: Scanning Resonator Tip and Whispering Gallery Mode Spectra……128

Figure 6.6: Calibration of Solution Refractive Index Changes……..129

Figure 6.7: Spectral Shifts due to Substrate Refractive Index Changes……130

Figure 6.8: Calibration of Substrate Refractive Index Changes……131

Figure 6.9: Scanning Resonator Microscopy Imaging……...132

Figure 6.10: Bright Field Image of Ultra-Thin Material Samples……134

Figure 6.11: SRM Analysis of AZ 1518 Thin Films……136

Figure 6.12: Calibration and Determination of AZ 1518 Refractive Index……..……137

Figure 6.13: Calculated Refractive Index Differences due to Exposure Energy……...138

Figure 6.14: SRM Analysis of Teflon AF Thin Films……...139

Figure 6.15: Atomic Force Microscopy of Graphene Oxide Thin Film……141

Figure 6.16: Whispering Gallery Mode Spectral Shift due to Graphene Oxide Thin Film……...142

Figure 6.17: SRM Analysis of Graphene Oxide Thin Film……...143

Figure 6.18: Resonant Wavelength Shifts due to UV Exposure to PE-DR19 Thin Films……145

Figure 6.19: Scanning Resonator Microscopy Dynamic Measurements of PE-DR19 Thin Films…..….146

Figure 7.1: Whispering Gallery Mode Spectral Shift due to Protein Functionalized Surface……...157

Figure 7.2: Structure of Heptafluoro Cholesterol and Sphingomyelin……..……159

Figure 7.3: Fluorescence Image of Monolayer in Air……160

Figure 7.4: SRM Analysis of Monolayer with Fluorinated Cholesterol Domains……161

Figure 7.5: Fluorescence Image of Monolayer in Water ……..162

Figure 7.6: Resonant Wavelength Shift and Calibration due to Refractive Index Changes ……165

Figure 8.1: Calibration Plot for Tunable Vortex TLB-6904 Laser.……...174

List of Tables

Table 1.1: Putative Protein Ovarian Cancer Biomarkers …….…….7

Table 1.2: Multiplexed Panels of Ovarian Cancer Protein Biomarkers …….……...9

Table 1.3: Putative MicroRNA Ovarian Cancer Biomarkers …….……11

Table 1.4: Label-Free Methods for Detection of Biomarkers…….……..……14

Table 2.1: Whispering Gallery Mode Resonator Geometries and Performance…….…….35

Chapter 1

Introduction and Overview

1.1 Ovarian Cancer

Ovarian cancer is the most prevalent and, unfortunately, the most fatal gynecologic cancer with over 60% of women receiving a terminal diagnosis.[1] Due to the high fatality rate, ovarian cancer remains the fifth leading cause of cancer related deaths among women.[2] These devastating statistics have changed little over the last several decades despite ongoing advancements in treatment.[3] Being that treatment is most effective prior to disease metastasis, early disease detection is vital for improved patient survival. This is further illustrated in **Fig. 1.1**, where ovarian cancer 5-year survival rates (blue) and percentage of women diagnosed (red) are plotted with respect to disease state.

As indicated in **Fig. 1.1**, less than 20% of women receive an accurate Stage I or II ovarian cancer diagnosis.[4, 5] Fortunately, for the few women who are diagnosed during Stage I or II of the disease, 5-year survival rates are greater than 90%.[6, 7] These statistics confirm ovarian cancer is curable when treatment is administered during initial stages. Unfortunately, early detection of ovarian cancer remains a difficult challenge due to vague, nonspecific initial symptoms and no available clinical screening method.[8] When diagnosed before metastasis, during early and regional stages of the disease, 5-year survival rates are relatively high. However, due to the asymptomatic nature of the disease, over 60% of women receive a Stage IV diagnosis where 5-year survival rates are less than 30%.[9]

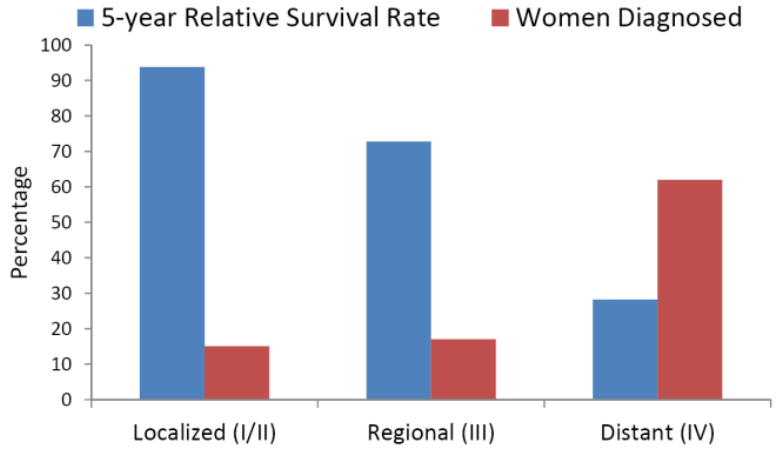

Figure 1.1. The 5-year relative survival rates (blue) of ovarian cancer patients and the percentage of women diagnosed (red) in localized (Stages I or II), regional (Stage III) and distant (Stage IV) stages of the disease.

These statistics illustrate the importance of early detection for improved outcomes for ovarian cancer patients. Early detection remains a challenge due to the asymptomatic nature of the disease. Current clinical diagnostic methods have little effect on reducing the high mortality rate of ovarian cancer. These existing approaches rely on invasive and non-specific methods for diagnosing primarily at-risk populations.

1.2 Ovarian Cancer Diagnostic Methods

Early detection of ovarian cancer has proven to be an extremely difficult challenge. Current standard modalities used for the detection of ovarian cancer of at-risk populations include ultrasounds and detection of elevated cancer antigen 125 (CA-125) levels in blood.[10] If these tests indicate the presence of disease, a tissue biopsy is required for disease confirmation and staging.

1.2.1 Tissue Biopsy

Although not a viable screening method for early detection, tissue biopsies are the most accurate diagnostic protocol for ovarian cancer patients. The removal of tumor tissue provides specific information about the disease state. Unfortunately, this method requires invasive procedures which increase time, costs, discomfort, and health risks for the patient. Furthermore, this approach is ill-suited for early detection of disease. It requires initial identification of the tumor by physical pelvic exams or diagnostic imaging. This pushes the stage of diagnosis to a later point, where successful treatments are much more difficult to achieve.

1.2.2 Diagnostic Imaging

Ultrasounds can be used to image ovaries in order to identify abnormal masses. Imaging approaches are advantageous because they are simple to perform and less invasive procedures for patients. However, standalone imaging tests are not reliable as an ovarian cancer screening approach. Invasive biopsy procedures are required to confirm a diagnostic image. Furthermore, imaging resolution require abdominal masses ~1 cm or greater for identification by ultrasound.[11] Ultimately, this restricts the usefulness of diagnostic imaging for early disease detection due to the considerable tumor size required for identification. An alternative, less-invasive approach relies on the identification of blood biomarkers which are correlated to presence of the disease.

1.2.3 Cancer Antigen 125 (CA-125) Blood Test

Quantifying disease markers is extremely advantageous in order to diagnose ovarian cancer at its earliest onset. Detection of markers in bodily fluids, such as blood, provides a non-invasive and specific screening platform which can be implemented as an early screening method. CA-125 is the most widely studied ovarian cancer biomarker. Serum concentrations of CA-125 have been found to be elevated in 80% of women with ovarian cancer and more than 90% of those with disseminated ovarian cancer.[9] For

at risk women, levels of CA-125 in blood are measured and used as an indicator of disease state. Currently, a widely employed clinical assay utilizes OC125 and M11 antibodies for the detection of CA-125, most often relying on fluorescent or colorimetric tags for protein quantitation. [12, 13] Women with levels greater than 35 U/mL are considered to be at-risk for disease and further, more invasive, testing is required to confirm a diagnosis.[9]

Alone CA-125 lacks specificity and sensitivity as a reliable indicator of early disease.[14] CA-125 was found to be elevated in only 50% of patients with Stage I ovarian cancer.[9] Furthermore, the marker has low sensitivity, ~40%, due to elevated levels in asymptomatic patients for benign conditions.[15] CA-125 is elevated in 1% of healthy women, 3% of women with benign ovarian diseases, and 6% of women with physiological conditions such as menstruation or pregnancy.[16-20] This marker alone, therefore, is considered insufficient for an early screen and is predominantly used to monitor treatment and recurrence of the disease or in combination with other diagnostic methods.[12]

1.2.4 Limitations of Current Diagnostic Methods

To address shortcomings of existing clinical methods for early disease detection, large clinical trials have been performed to evaluate a multimodal diagnostic approach. Recently, as part of the Prostate, Lung, Colorectal, and Ovarian Cancer (PLCO) screening trial, ultrasound and serum CA-125 levels were evaluated simultaneously to determine the effectiveness of combined diagnostic methods as a screening tool for ovarian cancer.[21] The study identified more ovarian cancer cases however, more than 72% of patients were in Stage III or IV of the disease at the time of diagnosis.[21] Unfortunately, the multimodal approach revealed no overall difference in diagnosed disease stage or ovarian cancer death rate.

Used alone or in combination, existing diagnostic tools have an unacceptably high false-positive rate and fail to identify early stage ovarian cancer. Furthermore, in some cases, current diagnostic methods have been reported to do more harm than good due to unnecessary surgeries performed on healthy patients.[21, 22] Currently, no ovarian cancer screening test exists for the general population due to the difficulties associated with early detection.[10] Improving early detection is an ongoing challenge aimed at

finding a better strategy or analytical tool which meets the required sensitivity and specificity to detect malignancies and minimize false-positives. Ideally, a screening test would provide a non-invasive scheme for the detection of ovarian cancer before the disease becomes symptomatic and the tumor becomes of significant size.

1.2.5 Desired Performance Metrics for an Ovarian Cancer Screening Test

To be practical, an early screening tool should be robust, easily implemented, and provide accurate detection capabilities at low costs. The low occurrence of ovarian cancer within the general population (~1.4%) requires a screening test to have a high degree of accuracy.[22] To be successful, a screening test must not only be accurate, but also have the ability to discern between benign and malignant tumors in order to prevent over diagnosis of the disease.[14] To characterize the performance of biomarkers for screening tools sensitivity, specificity and positive predictive values (PPV) are determined. Sensitivity is the probability of a test producing a positive result for an ill patient, or a true positive rate, defined as:[23]

$$\text{Sensitivity} = \frac{\#\ of\ true\ positivies}{\#\ of\ true\ positives + \#\ of\ false\ negatives}$$

The specificity of a diagnostic test is the probability of producing a negative result for a healthy patient, or a true negative rate, defined by:[23]

$$\text{Specificity} = \frac{\#\ of\ true\ negatives}{\#\ of\ true\ negatives + \#\ of\ false\ positives}$$

Finally, the positive predictive value (PPV) is the percentage of patients with a positive test result who actually have the disease, as defined by:[24]

$$\text{PPV} = \frac{\#\ of\ true\ positives}{\#\ of\ true\ positives + \#\ of\ false\ positives}$$

The low occurrence of ovarian cancer within the general population requires an effective early screen to have a sensitivity of at least 75%, specificity greater than 99% and a minimum PPV of 10%.[25] Despite ongoing efforts, no such test exists which meets these performance requirements. Fortunately, many biomarker discovery initiatives have been undertaken in order to identify promising and reliable markers of the disease. Over the last two decades, advancements in serum proteomics and gene-expression analysis have identified hundreds of potential biomarkers.[26] Fortunately, numerous proteins and nucleic acids have been identified to be indicators of early stage ovarian cancer.

1.3 Ovarian Cancer Biomarkers

To address the high mortality rate of ovarian cancer, an effective early screening technology is required. New biomarker targets continue to be identified and have been associated with initial disease states.[10, 27-33] Protein candidates, a few of which are listed in **Table 1.1**, provide promising targets for the development of early detection assays.[7, 34-36] Two proteins, CA-125 and HE4, have been approved by the Food and Drug Administration (FDA) as ovarian cancer biomarkers.[10]

Levels of CA-125 and HE4 have been found to assist with diagnosis, monitoring progression, or predicting recurrence of ovarian cancer. CA-125 is by far the most well-known and widely used ovarian cancer biomarker. As discussed previously, levels of CA-125 in blood are used as a diagnostic marker of disease. The protein is strongly correlated to late stages of ovarian cancer as elevated levels of CA-125 have been found in 90% of patients.[9] However, CA-125 lacks the required specificity and sensitivity needed to achieve early detection with only 50% of patients showing increased levels during Stage I or II.[10]

Another marker which has shown a strong correlation to disease progression and recurrence is HE4.[10, 37-39] Shown in **Table 1.1**, HE4 has a sensitivity and specificity for ovarian cancer comparable to CA-125. Studies indicate serum levels of HE4 could be used as a more accurate marker than CA-125 for predicting disease reoccurrence.[10] Furthermore, Hellström, *et. al.* determined HE4 to be more selective for ovarian

cancer when compared to CA-125. In the study, benign masses had elevated levels of CA-125 while HE4 levels were not increased, indicating improved selectivity for ovarian cancer.[40]

Additional non-FDA approved protein candidates are listed in **Table 1.1**. Studies have revealed increased sensitivity and specificity for some of these biomarker candidates, however, no single protein achieves the desired performance metrics required for an effective ovarian cancer screening tool.

Table 1.1 Putative ovarian cancer protein biomarkers for use in noninvasive tools for disease detection

Biomarker	Sensitivity	Specificity	Notes
Cancer Antigen 125 (CA-125)	40% to 78%	77% to 84%	FDA approved as marker for ovarian cancer, prognostic value for detecting reoccurrence[8, 41, 42]
HE4	80% to 95%	73% to 96%	FDA approved for monitoring disease recurrence or progression. Superior to CA-125 in differentiating benign versus malignant masses[37-40]
Cancer Antigen 72-4 (CA-72-4)	63.2%	91.1%	Recommended detection in combination with CA-125[43]
Osteopontin (OPN)	81% to 85%	55% to 80%	Involved in tumor metastasis and tumor progression, may be useful for recurrent disease[28, 37, 44]
IL-6	76%	NA	Correlated with poor prognosis[21]
Prolactin (PRL)	95%	95%	Elevated in ovarian cancer serum [36, 45, 46]
OVX 1	40%	83%	Beneficial in a panel with CA-125[41]
Cathepsin L	80%	85%	Beneficial in a panel, also elevated for cardiovascular diseases[47]
VEGF	77%	87%	Beneficial in combination with CA-125[37]

Although these protein markers show potential, to date no single marker has been able to achieve the required specificity (>99%) for an effective ovarian cancer screen.[25, 48] Within the diagnostic community

it is highly agreed upon that desired performance characteristics are unlikely to be achieved by a single marker. An effective screening technology will require the detection of multiple ovarian cancer biomarkers. By including additional markers with CA-125, a stronger diagnosis can be achieved.[35, 45, 49] Investigations of multiplexed protein biomarker panels have been completed to address shortcomings of individual protein markers.[50]

1.3.1 Ovarian Cancer Protein Biomarker Panels

A popular strategy aimed at improving sensitivity and specificity of screening tests is the incorporation of additional biomarkers capable of complimenting and improving CA-125 detection capabilities.[50, 51] **Table 1.2** highlights seven multiplexed protein panels which were investigated for improved detection of ovarian cancer. The first multiplexed panel listed, known as OVA1, was recently approved by the FDA as a clinical test to aid in tumor subtyping prior to surgery.[10] The multivariate index assay OVA1 consists of a blood test detecting five biomarkers and an algorithm to generate a malignancy score. For women with an identified pelvic mass, OVA1 can be used prior to surgery to assist in determining the histological subtype. Studies indicate the OVA1 test is more sensitive in detecting ovarian cancers than clinical assessment or CA-125 alone.[52] For Stage I disease, the OVA1 test had a measured sensitivity of 90%.[52] However, the specificity of the blood test is poor, with results indicating a lower degree of specificity than CA-125 alone. Therefore, OVA1 is not a valid screening tool.

Impressively, the simultaneous detection of CA-125, HE4, carcinoembryonic antigen (CEA), and vascular cell adhesion molecule-1 (VCAM-1) was able to discriminate early stage ovarian cancer with 86% sensitivity and 98% specificity.[49] Furthermore, when a panel of six markers were investigated (PRL, OPN, CA-125, leptin, IGF-II, and MIF), the sensitivity increased to 95.3% and specificity of 99.4%.[53] These studies indicate improved performance of multiple blood biomarkers as an indicator of ovarian cancer. However, in the study by Visintin, *et. al.* samples were collected post-diagnosis by current clinical technologies. Therefore, this six marker panel indicates the ability to diagnosis the disease during

late or distant stages, but requires further investigations to validate its effectiveness for early disease detection. Importantly, some of the multiplexed panels indicate improvements in detection capabilities with higher sensitivity and specificity compared to measuring a single biomarker.

Table 1.2. Multiplexed biomarker panels investigated for improved ovarian cancer diagnostics.

Biomarker Panel	Sensitivity	Specificity	Analytical Method
OVA1: Transthyretin, apolipoprotein, A-1, beta 2-microglobulin, transferrin, CA-125	93%	43%	Multivariate index assay[10, 52]
CA-125, HE4, CEA, VACAM-1	86%	98%	Bead-based immunoassay[49]
CA-125, CRP, SAA, IL-6, IL-8	94.1%	91.3%	Bead-based immunoassay[54]
CA-125, IGF-II, PRL, OPN, Leptin	NA	NA	ELISA[35]
CA-125, Leptin, PRL, OPN, IGF-II, MIF	95.3%	99.4%	Mass Spec./ELISA[53]
Leptin, OPN, PRL, IGF-II	95%	94%	ELISA[45]
CA-125, CA-72-4, CA-15-3, M-CSF	70%	98%	ELISA[55]

Although a significant improvement, multiplexed protein panels have yet to demonstrate accurate and efficient detection of early stages of ovarian cancer. To achieve an early screening tool for ovarian cancer, it would be advantageous to detect the presence of markers from a variety of origins. Recently, levels of nucleic acids have been shown to be correlated to the presence of disease.[56, 57] These non-protein targets may provide complimentary and additional information for accurate early detection of ovarian cancer.

1.3.2 MicroRNA as Promising Non-Protein Ovarian Cancer Biomarkers

In addition to protein-based biomarkers, there is a growing interest in quantifying non-protein targets of ovarian cancer to increase the accuracy of an early diagnosis. MicroRNAs (miRNAs) are small, single-stranded RNA molecules which have been shown to have profiles related to the presence of cancer.[56, 57] These noncoding RNAs are 19 to 25 nucleotides in length and have been identified in serum samples, thus, can be used as a non-invasive indicator of disease state.[56] Specifically, for ovarian cancer, numerous miRNA targets have been identified at elevated levels during initial stages of the disease.[29] MicroRNA targets are favorable ovarian cancer biomarkers due to their high stability, presence in plasma and serum and role in tumorigenesis.[29, 48, 56]

Measuring miRNA targets in serum samples provides a means to improve ovarian cancer screening. **Table 1.3** illustrates a selection of miRNA candidates which are both overexpressed and underexpressed in patient sera samples.[5, 58, 59] Specifically, miR-148b has been identified in over 90% of asymptomatic women providing a promising marker for early stages of ovarian cancer.[60] MiroRNA are also promising targets for achieving accurate histological subtyping during a diagnosis. Certain miRNA markers, including miR-141 and miR-21, have shown to be strongly correlated with specific ovarian cancer tumor subtypes.[29] Detecting panels of miRNA is a promising approach for improving ovarian cancer diagnosis, monitoring treatment, or predicting outcomes.[31]

Table 1.3. MicroRNA candidates for detection and monitoring ovarian cancer

Molecular Biomarker	Expression Levels	Notes
miR-21	Overexpressed	Possible for panel screening tool[5]
miR-29a	Overexpressed	Possible for panel screening tool[5]
miR-127	Underexpressed	Possible for panel screening tool[5]
miR-155	Underexpressed	Possible for panel screening tool[5]
miR-200a	Overexpressed	Significantly overexpressed[29, 58]
miR-142-3p	Overexpressed	Significantly overexpressed[59]
miR-141	Overexpressed	Advantageous for histological subtyping[29]
miR-21	Overexpressed	Advantageous for histological subtyping[29]
miR-148b	Overexpressed	In 92.21% of asymptomatic women, important for early stage[60]

As demonstrated with the protein panel studies, an ovarian cancer diagnostic test can be improved with the detection of multiple markers in a single assay. Detecting protein and non-protein targets in a single assay would be advantageous for achieving the high sensitivity and specificity requirements for an early screening test. With this goal in mind, it is important to consider current clinical assay capabilities.

1.4 Enzyme-Linked Immunosorbent Assay (ELISA)

A common diagnostic tool for biomarker detection is an enzyme-linked immunosorbent assay (ELISA). Considered to be the "gold standard" for diagnostics, ELISA provides high specificity and robust detection of proteins in bodily fluids. Several ELISA assay formats exist which utilize antibody-antigen interactions for the detection of target proteins. A particular assay schematic with a high degree of specificity relies on antibody-antigen interactions to "sandwich" a target protein and quantify concentrations in sample solutions. **Figure 1.2** illustrates a typical sandwich-based ELISA method. Target protein within a sample solution binds to surface immobilized antibodies. For colorimetric detection, a secondary antibody labeled with an enzymatic tag, such as horseradish peroxidase (HRP), is incubated with the antibody-antigen complex. By adding 3,3',5,5'-tetramethylbenzidine (TMB) in the

presence of hydrogen peroxide, HRP oxidation leads to the formation of a diimine product.[61] After incubation, an acidic solution is added to stop the reaction. For protein quantitation, absorbance at 450 nm is measured for ELISA sample and calibration wells.

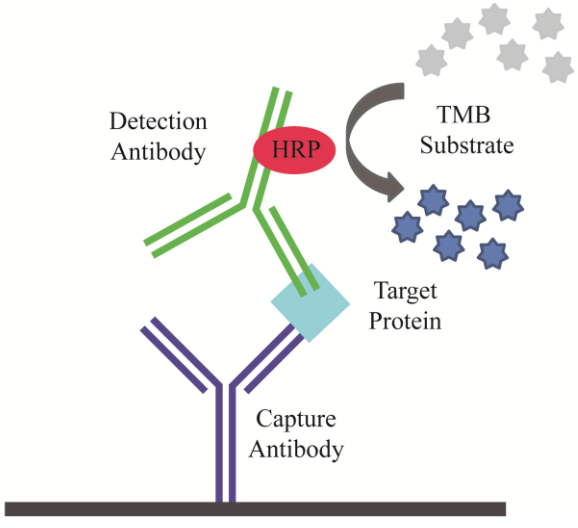

Figure 1.2. Schematic of a sandwich ELISA immunoassay where a target protein is captured by a surface immobilized antibody. To detect the target protein, a detection antibody is incubated with the sample, followed by a HRP labeled antibody. Addition of TMB results in a colorimetric reaction, enabling quantification of target protein in solution.

There are several factors which contribute to the wide use of ELISA assays for biomarker detection. By utilizing a primary and secondary antibody, a sandwich-ELISA assay has a high degree of specificity with reduced cross-reactivity issues. Amplification of the colorimetric signal results in low detection limits (nM). The assay is also easily performed in multi well plates, allowing for method automation. However, drawbacks do exist for ELISA assays.

A particular limitation of the sandwich-ELISA method results from the requirement of both a primary and secondary antibody which increases the overall time and costs associated with an assay. Additional limitations result from utilizing antibodies as molecular capture agents which limits the assay to measuring proteins and, furthermore, single protein targets per well due to the general colorimetric signal used for quantitation. Additionally, the required enzymatic tag for generating the colorimetric signal

relies on a labeled secondary antibody which may suffer from altered molecular structure and performance. These limitations have prompted interest in developing alternative clinical assays.

Label-free techniques overcome limitations of ELISA assays by enabling a homogeneous platform for the detection of proteins and nucleic acid targets in a single approach. Furthermore, label-free platforms reduce chemistry, costs, and time required for the detection of biomolecules. New, label-free analytical approaches are needed to improve clinical capabilities for multiplexed detection of protein as well as non-protein targets. Ultimately, an assay capable of detecting protein and miRNA ovarian cancer markers would improve the specificity of an early detection screen.

1.5 Label-Free Biosensing Platforms

Label-free techniques provide flexibility for diagnostic platforms as they allow real-time detection capabilities of virtually any complex while requiring minimum assay development. In label-free platforms, no additional labels or modifications are required for analyte detection.[62] This enables the development of low cost, inexpensive and rapid assays. These advantages are well suited to address clinical needs. Particular label-free techniques which have shown considerable promise for clinical applications are outlined in **Table 1.4** and described in the following sections.

Table 1.4. Analytical methods for the label-free detection of biomarkers.

Analytical Method	Detection Limits	Notes
Nanopores and Nanowires[63-65]	fM	+ High multiplexed potential - Extensive fabrication requirements
Quartz-Crystal Microbalance[66]	μM	+ Sensitive - Limited multiplex capabilities
Cantilever[67]	nM	+ High multiplex capabilities + Small in size, portable - Not user friendly, or easily implemented
Surface Plasmon Resonance (SPR)[68]	pM to μM	+ Well-established technique + Commercially available - Detection limits
Interferometry[68]	fM to pM	+ Rapid, sensitive - Limited multiplex capabilities - Low throughput - Reference required
Ellipsometry[69]	nM	+ Low costs - Limited multiplex capabilities - Low spatial resolution
Optical Microcavities[68, 70-72]	Single molecule to pM to μM	+ Sensitive - Limited multiplex capabilities

1.5.1 Electrochemical-Based Label-Free Biosensors

Miniaturized electrochemical sensors, such as nanopores and nanowires, have been demonstrated to have sensitive detection capabilities for proteins and DNA.[62-65, 73] These miniaturized systems, 5 to 100 nm in size, are capable of detecting target molecules based on measured changes in conduction, impedance or capacitance. The sensitive detection schemes are further complimented by rapid detection capabilities and ease of use.[73]

In particular, these attributes have generated interest in utilizing nanowire arrays for the development of clinically relevant assays. Zheng, *et. al.* demonstrated multiplexed capabilities by simultaneously detecting three cancer biomarkers in serum samples using a nanowire array-based sensor. The device was

able to detect proteins at femtomolar concentrations.[65] While these miniaturized electrochemical sensors have much potential, the required fabrication methods limit their wide use. Creating precise nanostructure arrays requires tedious fabrication using specialized and expensive equipment. These limitations prevent routine implementation of these systems in the clinic. An alternative label-free approach based on system mechanical changes has been demonstrated as a robust and reliable analytical tool.

1.5.2 Mechanical-Based Label-Free Biosensors

A piezoelelctric crystal responds to absorbed mass by a change in its resonant frequency. [74, 75] This technique is the basis of a quartz-crystal microbalance (QCM) which is used for sensitive, label-free detection of surface events, such as antigen-antibody binding.[66, 76] Frequency measurements provide a high degree of sensitivity, however the platform is not easily integrated with solutions and data interpretation can be complex due to the sensitivity of the acoustic detection. An alternative mechanical-based sensor utilizes functionalized cantilever surfaces.

Micro- and nanocantilever biosensors measure a mechanical response due to surface binding events. As analytes bind to a modified cantilever surface, deflections or changes in the strain/stress provide a mechanical measurement of concentration.[67] The platform allows for a high degree of multiplexing as each cantilever can be functionalized with a particular recognition element. Similar to QCM systems, cantilevers suffer from signal dampening when analyzing solution samples. Solutions can be analyzed more accurately by alternative label-free platforms, such as systems which rely on optical-based signals.

1.5.3 Optical-Based Label-Free Biosensors

Optical-based label-free sensing platforms rely on measuring refractive index which is a parameter describing how light propagates through a medium. Refractive-index based sensors are desirable for the development of simple, low-cost sensing schemes. While the sensing mechanism for refractive index

sensors is similar, the construction and execution varies. A common refractive index approach which has been developed as a commercial instrument is surface plasmon resonance (SPR).

In SPR, metal surface plasmons are used to probe analyte interactions.[77] Valence electrons in the metal surface absorb incident electromagnetic radiation if it matches their collective oscillation, or plasmon. Resonances are measured by monitoring reflected light intensity as a function of angle or wavelength. By immobilizing capture molecules on a surface, plasmons can be used to detect and quantify corresponding binding events. This well established, label-free technique allows for real-time analysis of binding events and kinetics.[75] One of the more difficult components of SPR is incorporating multiplexed detection capabilities.

With the appropriate sample surfaces, multiplexed protein detection can be achieved using SPR. In order to detect multiple targets samples must consist of spatially addressed high-density arrays. These patterned metal surfaces can be analyzed by SPR imaging approaches.[78] The requirement of high quality microarrays on metal supports has limited detection capabilities as well as the usefulness of SPR for routine clinical implementation.

An alternative refractive index sensor which has less stringent sample requirements is based on interferometry. There are several designs of interferometry based sensors as the basic principle relies on measuring small changes in optical phase velocity of light to quantify a target species. Interferometric techniques are sensitive with detection limits in the femtomolar range.[68] However, these techniques have limited multiplexing capabilities and overall low throughput, reducing their potential as effective platforms for ovarian cancer screens.

A well-established label-free platform for investigating surfaces and thin films relies on ellipsometry. Ellipsometry is a powerful technique for measuring refractive index, and thickness of materials. The reflection-based technique measures polarization shifts which can be correlated to material optical properties.[79] These measurements can be extended to biological molecules on a functionalized surface. This low cost, non-destructive method is capable of achieving good detection limits, however, it suffers from the inability to achieve multiplexed detection which is vital for early detection screens.

Furthermore, data interpretation can be cumbersome as it requires extensive modeling by experienced researchers. Optical microcavities are emerging as promising techniques which overcome many of the limitations of the discussed optical-based label-free sensors.

Optical microcavities are an emerging platform for the development of label-free platforms for the detection of biomolecules. These cavities are small spherical structures which support whispering gallery mode (WGM) resonances. Resonances occur due to the recirculation of light within these circular structures through continuous total internal reflection events. The particular wavelength supported within the structure depends upon the surrounding refractive index, thus, these cavities can be utilized as sensitive label-free detectors. WGM techniques have demonstrated excellent performance metrics for the detection of biomolecules.[71, 72] In Chapter 2, a more thorough discussion of optical microcavities is presented with a focus on fundamental aspects and desirable performance metrics of WGM resonators for label-free detection of biomolecules.

1.6 Motivation of Dissertation

The asymptomatic nature of ovarian cancer results in delayed diagnoses and poor patient prognosis. Currently, no screening method is available to the general population while at-risk women are subjected to clinical diagnostic tools with unacceptable false-positive rates due to poor sensitivity and specificity. Ideally, a screening tool capable of quantifying protein and non-protein targets in a single assay would help address clinical early detection requirements. ELISA assays fail to meet these clinical needs by only detecting proteins and having limited multiplex capabilities. To overcome multi-antigen challenges, label-free optical resonators can be utilized for the detection of numerous protein and nucleic acids within a single assay. Optical resonators provide a particularly flexible platform for the development of multiplexed biosensors capable of real-time detection of protein binding and nucleic acid hybridization.

1.7 References

1. Yap, T. A., et al., Beyond Chemotherapy: Targeted Therapies in Ovarian Cancer. *Nat. Rev. Cancer* **2009,** *9* (3), 167-181.
2. Moyer, V. A., Screening for Ovarian Cancer: U.S. Preventive Services Task Force Reaffirmation Recommendation Statement. *Ann Intern Med* **2012,** *157* (12), 900-904.
3. Institute, N. C. *Snapshot of Ovarian Cancer*; National Institutes of Health: Bethesda, MD., 2011.
4. Key Statistics About Ovarian Cancer. (accessed 10/08/2010).
5. Resnick, K. E., et al., The Detection of Differentially Expressed microRNAs From the Serum of Ovarian Cancer Patients Using a Novel Real-Time PCR Platform. *Gynecol. Oncol.* **2009,** *112*, 55-59.
6. Chambers, A. F.; Vanderhyden, B. C., Ovarian Cancer Biomarkers in Urine. *Clin. Cancer Res.* **2006,** *12* (2), 323-327.
7. Jacobs, I. J.; Menon, U., Progress and Challenges in Screening for Early Detection of Ovarian Cancer. *Mol. Cell. Proteomics* **2004,** *3* (4), 355-366.
8. Wittmann, J.; Jäck, H.-M., Serum microRNAs as Powerful Cancer Biomarkers. *Biochimica et Biophysica Acta In Press*.
9. Nossov, V., et al., The Early Detection of Ovarian Cancer: From Traditional Methods to Proteomics. Can we Really do Better than Serum CA-125? *Am. J. Obstet. Gynecol.* **2008,** *199* (3), 215-223.
10. O'Toole, S. A., et al. In *Noninvasive Biomarkers in Ovarian Cancer*, CRC Press: 2014; pp 615-642.
11. Ng, A.; Swanevelder, J., Resolutin in Ultrasound Imaging. *Continuing Education in Anaesthesia, Critical Care & Pain* **2011,** *11* (5), 186-192.
12. Karlan, B. Y., The Quest for Ovarian Cancer's Holy Grail: Can CA-125 Still be the Chalice of Early Detection? *J. Clin. Oncol.* **2007,** *25* (11), 1303-1304.
13. Kenemans, P., et al., The Second Generation CA-125 Assays. *Ann Med* **1995,** *27* (1), 107-113.
14. Etzioni, R., et al., Early Detection: The Case for Early Detection. *Nat. Rev. Cancer* **2003,** *3* (4), 243-252.
15. Wittmann, J.; Jaeck, H.-M., Serum microRNAs as Powerful Cancer Biomarkers. *Biochim. Biophys. Acta, Rev. Cancer* **2010,** *1806* (2), 200-207.
16. Welander, C. E., What do CA-125 and Other Antigens tell us About Ovarian Cancer Biology? *Acta Obstet Gynecol Scand Suppl* **1992,** *155*, 85-93.

17. Saksela, E., Prognostic Markers in Epithelial Ovarian Cancer. *Int J Gynecol Pathol* **1993,** *12* (2), 156-61.
18. Kenemans, P., et al., CA-125 in Gynecological Pathology--a Review. *Eur J Obstet Gynecol Reprod Biol* **1993,** *49* (1-2), 115-24.
19. Farghaly, S. A., Tumor Markers in Gynecologic Cancer. *Gynecol Obstet Invest* **1992,** *34* (2), 65-72.
20. Bast, R. C., Jr., et al., CA-125: the Past and the Future. *Int. J. Biol. Markers* **1998,** *13* (4), 179-187.
21. Buys, S. S., et al., Effect of Screening on Ovarian Cancer Mortality. The Prostate, Lung, Colorectal and Ovarian (PLCO) Cancer Screening Randomized Controlled Trial. *JAMA, J. Am. Med. Assoc.* **2011,** *305* (22), 2295-2303.
22. Slomski, A., Screening Women for Ovarian Cancer Still Does More Harm than Good. *JAMA, J. Am. Med. Assoc.* **2012,** *307* (23), 2474-2475.
23. Altman, D. G.; Bland, J. M., Diagnostic Tests. 1: Sensitivity and Specificity. *BMJ* **1994,** *308* (6943), 1552.
24. Altman, D. G.; Bland, J. M., Diagnostic Tests 2: Predictive Values. *BMJ* **1994,** *309* (6947), 102.
25. Clarke-Pearson, D. L., Clinical Practice. Screening for Ovarian Cancer. *N Engl J Med* **2009,** *361* (2), 170-177.
26. Rapkiewicz, A. V., et al., Biomarkers of Ovarian Tumours. *Eur. J. Cancer* **2004,** *40* (17), 2604-2612.
27. Suh, K. S., et al., Ovarian Cancer Biomarkers for Molecular Biosensors and Translational Medicine. *Expert Rev. Mol. Diagn.* **2010,** *10* (8), 1069-1083.
28. Nakae, M., et al., Preoperative Plasma Osteopontin Level as a Biomarker Complementary to Carbohydrate Antigen 125 in Predicting Ovarian Cancer. *J. Obstet. Gynaecol. Res.* **2006,** *32*, 309-314.
29. Iorio, M. V., et al., MicroRNA Signatures in Human Ovarian Cancer. *Cancer Res.* **2007,** *67* (18), 8699-8707.
30. Dobrzycka, B., et al., Circulating Levels of TNF-Alpha and its Soluble Receptors in the Plasma of Patients with Epithelial Ovarian Cancer. *Eur. Cytokine Network* **2009,** *20* (3), 131-134.
31. Dahiya, N., et al., MicroRNA Expression and Identification of Putative miRNA Targets in Ovarian Cancer. *Plos One* **2008,** *3* (6).
32. Balch, C., et al., Epigenetic Changes in Ovarian Cancer. *Endocrinology* **2009,** *150* (9), 4003-4011.
33. Anastasi, E., et al., HE4: a New Potential Early Biomarker for the Recurrence of Ovarian Cancer. *Tumor Biol.* **2010,** *31* (2), 113-119.

34. Terry, K. L., et al., Blood and Urine Markers for Ovarian Cancer: A Comprehensive Review. *Dis. Markers* **2004,** *20* (2), 53-70.
35. Hwang, J., et al., Correlation Between Preoperative Serum Levels of Five Biomarkers and Relationships Between these Biomarkers and Cancer Stage in Epithelial Ovarian Cancer. *J. Gynecol. Oncol.* **2009,** *20* (3), 169-175.
36. Levina, V. V., et al., Biological Significance of Prolactin in Gynecologic Cancers. *Cancer Res.* **2009,** *69* (12), 5226-5233.
37. Nguyen, L., et al., Biomarkers for Early Detection of Ovarian Cancer. *Womens Health* **2013,** *9* (2), 171-185.
38. Moore, R. G., et al., The Use of Multiple Novel Tumor Biomarkers for the Detection of Ovarian Carcinoma in Patients with a Pelvic Mass. *Gynecol. Oncol.* **2008,** *108* (2), 402-408.
39. Scholler, N., et al., Bead-Based ELISA for Validation of Ovarian Cancer Early Detection Markers. *Clin. Cancer Res.* **2006,** *12* (7, Pt. 1), 2117-2124.
40. Hellstrom, I., et al., The HE4 (WFDC2) Protein is a Biomarker for Ovarian Carcinoma. *Cancer Res.* **2003,** *63* (13), 3695-3700.
41. Woolas, R. P., et al., Combinations of Multiple Serum Markers Are Superior to Individual Assays for Discriminating Malignant from Benign Pelvic Masses. *Gynecol. Oncol.* **1995,** *59* (1), 111-116.
42. Tamakoshi, K., et al., Clinical Value of CA125, CA19-9, CEA, CA72-4, and TPA in Borderline Ovarian Tumor. *Gynecol Oncol* **1996,** *62* (1), 67-72.
43. Negishi, Y., et al., Serum and Tissue Measurements of CA72-4 in Ovarian Cancer Patients. *Gynecol Oncol* **1993,** *48* (2), 148-54.
44. Kim, J. H., et al., Osteopontin as a Potential Diagnostic Marker for Ovarian Cancer. *Women's Oncol. Rev.* **2002,** *2*, 313-314.
45. Mor, G., et al., Serum Protein Markers for Early Detection of Ovarian Cancer. *Proc. Natl. Acad. Sci. U. S. A.* **2005,** *102* (21), 7677-7682.
46. Yurkovetsky, Z., et al., Development of Multimarker Panel for Early Detection of Endometrial Cancer. High Diagnostic Power of Prolactin. *Gynecol. Oncol.* **2007,** *107*, 58-65.
47. Nishida, Y., et al., Increased Cathepsin L Levels in Serum in Some Patients with Ovarian Cancer: Comparison with CA125 and CA72-4. *Gynecol Oncol* **1995,** *56* (3), 357-61.
48. Zhang, B., et al., An Overview of Biomarkers for the Ovarian Cancer Diagnosis. *Eur. J. Obstet. Gynecol. Reprod. Biol.* **2011,** *158*, 119-123.
49. Yurkovetsky, Z., et al., Development of a Multimarker Assay for Early Detection of Ovarian Cancer. *J Clin Oncol* **2010,** *28*, 2159-2166.

50. Nolen, B. M.; Lokshin, A. E., Biomarker Testing for Ovarian Cancer: Clinical Utility of Multiplex Assays. *Mol. Diagn. Ther.* **2013,** *17* (3), 139-146.
51. Badgwell, D.; Bast, R. C., Early Detection of Ovarian Cancer. *Dis. Markers* **2007,** *23* (5-6), 397-410.
52. Ueland, F. R., et al., Effectiveness of a Multivariate Index Assay in the Preoperative Assessment of Ovarian Tumors. *Obstet Gynecol* **2011,** *117* (6), 1289-97.
53. Visintin, I., et al., Diagnostic Markers for Early Detection of Ovarian Cancer. *Clin. Cancer Res.* **2008,** *14* (4), 1065-1072.
54. Edgell, T., et al., Phase II Biomarker Trial of a Multimarker Diagnostic for Ovarian Cancer. *J. Cancer Res. Clin. Oncol.* **2010,** *136* (7), 1079-1088.
55. Skates, S. J., et al., Preoperative Sensitivity and Specificity for Early-Stage Ovarian Cancer When Combining Cancer Antigen CA-125II, CA 15-3, CA 72-4, and Macrophage Colony-Stimulating Factor Using Mixtures of Multivariate Normal Distributions. *J Clin Oncol* **2004,** *22* (20), 4059-66.
56. Ferracin, M., et al., Micromarkers: miRNAs in Cancer Diagnosis and Prognosis. *Expert Rev. Mol. Diagn.* **2010,** *10*, 297-308.
57. Calin, G. A.; Croce, C. M., MicroRNA Signatures in Human Cancers. *Nat. Rev. Cancer* **2006,** *6* (11), 857-866.
58. Taylor, D. D.; Gercel-Taylor, C., MicroRNA Signatures of Tumor-Derived Exosomes as Diagnostic Biomarkers of Ovarian Cancer. *Gynecol. Oncol.* **2008,** *110* (1), 13-21.
59. Wu, X., et al., Elevated Levels of Dendritic Cell-Correlated miRNAs in Ascites and Sera of Patients with Ovarian Cancer. *Xi Bao Yu Fen Zi Mian Yi Xue Za Zhi* **2015,** *31* (3), 383-386.
60. Chang, H., et al., Increased Expression of miR-148b in Ovarian Carcinoma and its Clinical Significance. *Mol. Med. Rep.* **2012,** *5* (5), 1277-1280.
61. Josephy, P. D., et al., The Horseradish Peroxidase-Catalyzed Oxidation of 3,5,3',5'-Tetramethylbenzidine. *J. Biol. Chem.* **1982,** *257* (7), 3669-3675.
62. Hunt, H. K.; Armani, A. M., Label-Free Biological and Chemical Sensors. *Nanoscale* **2010,** *2* (9), 1544-1559.
63. Patolsky, F., et al., Nanowire-Based Biosensors. *Anal. Chem.* **2006,** *78*, 4260-4269.
64. Kasianowicz, J. J., et al., Nanoscopic Porous Sensors. *Annu. Rev. Anal. Chem.* **2008,** *1*, 737-766.
65. Zheng, G., et al., Multiplexed Electrical Detection of Cancer Markers with Nanowire Sensor Arrays. *Nat. Biotechnol.* **2005,** *23* (10), 1294-1301.
66. Vashist, S.; Vashist, P., Recent Advances in Quartz Crystal microbalance-Based Sensors. *Journal of Sensors* **2011,** *2011*, 1-13.

67. Hwang, K. S., et al., Micro- and Nanocantilever Devices and Systems for Biomolecule Detection. *Annu Rev Anal Chem* **2009,** *2,* 77-98.
68. Fan, X., et al., Sensitive Optical Biosensors for Unlabeled Targets: A Review. *Anal. Chim. Acta* **2008,** *620* (1-2), 8-26.
69. Sun, Y.-S.; Zhu, X., Ellipsometry-Based Biosensor for Label-Free Detection of Biomolecular Interactions in Microarray Format. *Sens. Mater.* **2013,** *25* (9), 673-688.
70. Chiasera, A., et al., Spherical Whispering-Gallery-Mode Microresonators. *Laser Photonics Rev.* **2010,** *4* (3), 457-482.
71. Soria, S., et al., Optical Microspherical Resonators for Biomedical Sensing. *Sensors* **2011,** *11*, 785-805.
72. Vollmer, F.; Arnold, S., Whispering-Gallery-Mode Biosensing: Label-Free Detection Down to Single Molecules. *Nature Methods* **2008,** *5* (7), 591-596.
73. Wang, J., Electrochemical Biosensors: Towards Point-of-Care Cancer Diagnostics. *Biosens. Bioelectron.* **2006,** *21* (10), 1887-1892.
74. Seker, S.; Elcin, Y. M., Bioanalytical Applications of Piezoelectric Sensors. In *Nanopatterning and Nanoscale Devices for Biological Applications*, Selimovic, S., Ed. CRC Press: 2014; pp 261-288.
75. Cooper, M. A., Label-Free Screening of Bio-Molecular Interactions. *Anal. Bioanal. Chem.* **2003,** *377* (5), 834-842.
76. Janshoff, A., et al., Piezoelectric Mass-Sensing Devices as Biosensors-an Alternative to Optical Biosensors? *Angew. Chem., Int. Ed.* **2000,** *39* (22), 4004-4032.
77. Homola, J., Present and Future of Surface Plasmon Resonance Biosensors. *Anal. Bioanal. Chem.* **2003,** *377* (3), 528-539.
78. Ouellet, E., et al., Multiplexed Surface Plasmon Resonance Imaging for Protein Biomarker Analysis. *Methods Mol. Biol.* **2013,** *949* (Microfluidic Diagnostics), 473-490.
79. Garipcan, B., et al., New Generation Biosensors Based on Ellipsometry. In *New Perspectives in Biosensors Technology and Applications*, Serra, P. A., Ed. InTech: 2011; pp 197-214.

Chapter 2

Whispering Gallery Mode Resonators for Label-Free Biosensing

2.1 Introduction

Assays which exploit refractive index changes as the sensing signal offer promising general routes for the development of improved biomarker screens. These techniques enable the homogeneous detection of proteins, nucleic acids, or other markers of disease without the use of labels, making them attractive for both point-of-care and clinical applications. In particular, whispering gallery mode (WGM) optical resonators have shown considerable promise as platforms for assay development.

A whispering gallery mode was first described in the 1800's by Lord Rayleigh based on an interesting observation he made while in St. Paul's Cathedral. At a particular level of the cathedral, he noticed sound waves spoken into the gallery wall could carry and reach a second individual at the opposite side of the room. The circular structure of the gallery had the ability to confine sound waves through surface reflections, thus, allowing a whisper to travel tens of meters. A similar phenomenon can be observed in small, circular dielectric materials tens of micrometers in size. Light waves coupled into these objects can be confined through continuous total internal reflection events due to refractive index differences between the spherical structure and its surroundings. Although the whispering gallery mode phenomenon has been known for many years, recent advancements in microfabrication techniques and tunable light sources have increased the usefulness and applicability of these resonators for sensing. Before thoroughly discussing WGM sensors, it is important to understand the concepts of total internal reflection and the evanescent wave.

2.1.1 Total Internal Reflection and the Evanescent Wave

Whispering gallery mode resonators are able to achieve resonances by supporting the recirculation of light within their spherical cavity. To understand this phenomenon, consider the behavior of light passing from one material to another described by Snell's law, which states:

$$Sin\theta_1 n_1 = Sin\theta_2 n_2 \qquad \textbf{Equation 2.1}$$

where n_1 and n_2 are the material refractive indices, θ_1 is the light beam's incident angle and θ_2 is the refracted angle of the beam measured from the interface normal. When a light wave reaches a boundary between two different materials, portions of the light will be refracted and reflected due to different dielectric properties of the materials. At shallow incident angles, light passing from a material of higher refractive index to a material of lower refractive index will be refracted away from the interface normal, shown in **Fig. 2.1A**. As the angle of incidence increases, the angle of refraction increases. At the point where $\theta_2 = 90°$, defines the critical angle (θ_c):

$$\theta_c = sin^{-1}\frac{n_2}{n_1} \qquad \textbf{Equation 2.2}$$

At an angle of incidence equal to or greater than the critical angle (θ_c), light is no longer refracted into the low refractive index material. Instead, at this condition, all of the light is reflected back into the original material achieving total internal reflection (TIR), illustrated in **Fig. 2.1B**. In order for TIR to occur, light must pass from a high index material to a low index material ($n_1 > n_2$).

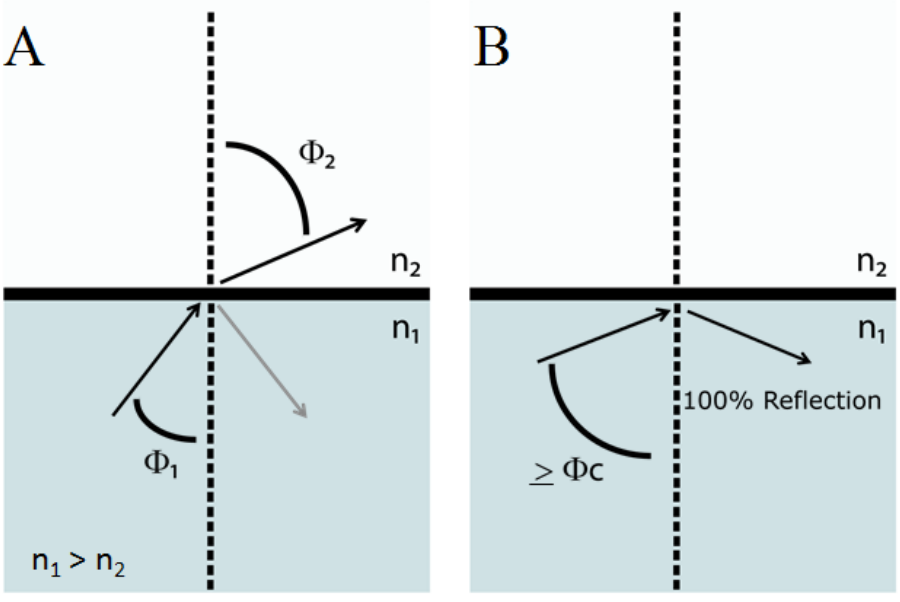

Figure 2.1. The behavior of light at a boundary between two mediums is described by Snell's law (equation 2.1). At shallow incident angles (θ_1), light traveling from a high index (n_1) to a low index (n_2) material will be refracted (θ_2) as well as a small portion of light reflected (shown in grey). (B) Incident angles equal to or greater than the critical angle (θ_c) result in 100% of the beam reflected back into the high index material, also known as total internal reflection (TIR).

Total internal reflection is the operating principle behind optical fibers which are thin, glass filaments used to transmit light long distances. An important component of TIR is the non-propagating, exponentially decaying electromagnetic field which extends into the low index medium. This field is known as an evanescent wave and is illustrated in **Fig. 2.2**. For visible light, the exponentially decaying field extends ~200 nm beyond the material boundary.[1] Importantly, this non-propagating field can sense molecules at the boundary surface, thus, has been exploited for fluorescence microscopy as well as for the development of label-free sensing schemes.

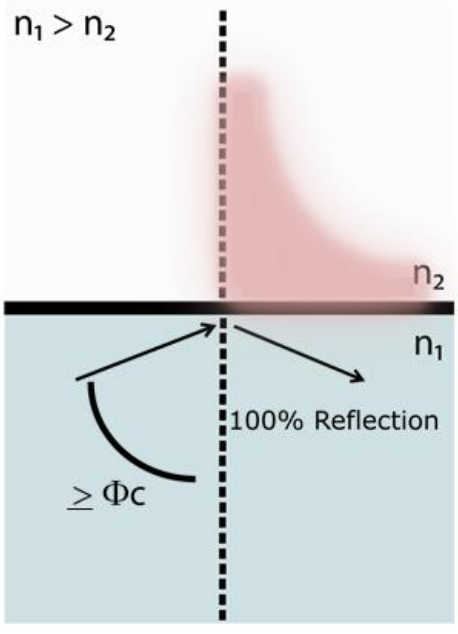

Figure 2.2. An evanescent wave occurs at a point of total internal reflection (TIR). This non-propagating field exponentially decays at the material boundary, extending hundreds of nanometers into the low index material.

For sensing applications, the concentrated electromagnetic field can be used to sense local events near the boundary, such as surface binding events. The limited propagating depth is advantageous for minimizing background signal in these techniques. Total internal reflection and the evanescent wave are important fundamental aspects for understanding WGM resonators and their ability to sense their surrounding environment.

2.2 Whispering Gallery Mode Resonators

Light coupled into small, high index structures such as glass microspheres can undergo nearly TIR at each interaction with the dielectric interface, leading to the confinement of light within the spherical structure. When the roundtrip distance within the sphere is an integer multiple of the coupled wavelength, the light coherently drives itself leading to WGM resonances, shown schematically in **Fig. 2.3** by the optical ray (black line) trapped near the surface of the spherical cavity.

Figure 2.3. Schematic illustrating continuous TIR events within a spherical microcavity. Recirculation of a particular wavelength within the cavity achieves a whispering gallery mode resonance.

The ability of microstructures to confine light is based on refractive index differences between the spherical resonator and its surroundings. Confinement of light achieves a WGM resonance when the following condition is met:

$$\lambda_r = \frac{2\pi r n_{\text{eff}}}{m} \qquad \textbf{Equation 2.3}$$

where λ_r is the resonant wavelength, r is the radius of the cavity, n_{eff} is the effective refractive index surrounding the sphere, and m is an integer. Importantly, continuous total internal reflection events due to light confinement result in a strong evanescent field extending from the resonator surface and into the surrounding environment. The electromagnetic field at the surface of a WGM resonator can interact and respond to external environment changes. **Equation 2.3** illustrates this through the linear relationship between the resonant wavelength (λ_r) and effective refractive index (n_{eff}). It is this relationship which has generated much interest in utilizing WGM resonators as label-free refractometric and biologic sensors.[1-3]

One way to excite WGMs involves positioning a thin optical fiber (approximately 3 μm in diameter) near the WGM resonator. Precise positioning allows for light from the fiber to evanescently couple into the resonator when the resonant condition is met. **Figure 2.4** shows a simplified schematic for a microsphere WGM transmission measurement. A tunable laser is coupled into one end of the tapered

optical fiber while the corresponding transmission spectrum is collected by a photodetector at the opposite end. As the tunable light source scans through a wavelength range, transmitted intensity is measured by the photodiode. When the laser is tuned to the appropriate wavelength, a sharp dip in intensity is recorded, as shown in **Fig. 2.4**. The center of the peak corresponds to the WGM resonance. By altering the refractive index surrounding the sphere, through solution refractive index changes or a surface binding event, a corresponding shift in the measured resonant wavelength occurs (shown in red). The magnitude of the shift provides a quantitative measure of system refractive index changes, **Equation 2.3**.

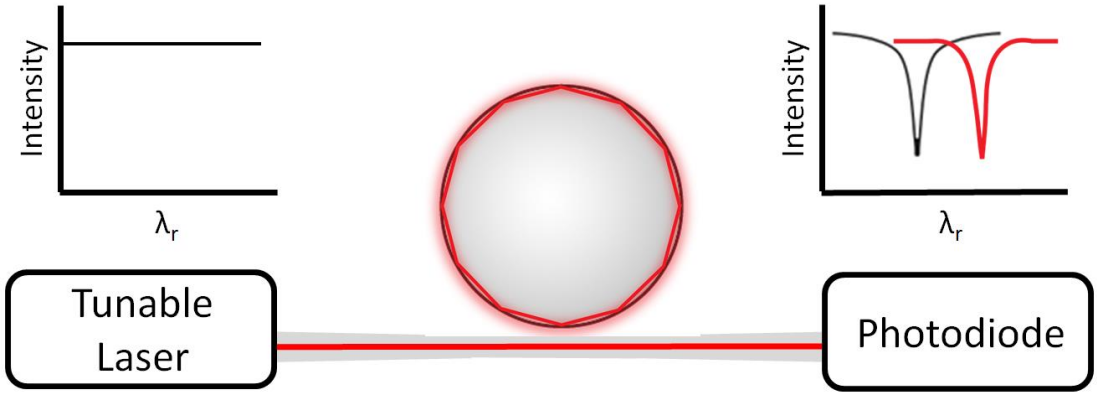

Figure 2.4. Schematic for the detection of WGM resonances through transmission measurements. A thinned optical fiber is placed adjacent to a dielectric microsphere to couple light to the resonator. Light from a tunable laser is introduced at one end of the fiber optic, while transmitted light is collected by a photodetector at the opposite end. By altering the refractive index, a corresponding resonant wavelength shift can be measured (red transmission spectrum).

For sensing, the recirculation of light within the compact, small size of WGM spherical cavities leads to multiple-pass interactions between the propagating electromagnetic field and the resonator surface. These multi-pass photonic structures provide sensitive detection schemes due to long effective path lengths achieved through the recirculation of light. Enhanced path lengths increase the sample-light interaction compared to planar waveguide photonics, thus, WGM resonators are advantageous for the development of extremely sensitive label-free sensing platforms.[1-6]

2.2.1 Whispering Gallery Mode Resonators for Biosensing

Figure 2.5 illustrates one way in which WGM resonators are used as biosensors. Biorecognition elements, such as antibodies, are covalently attached to the resonator surface. When exposed to a sample solution containing antigens of interest, target proteins will bind to the surface attached antibodies. Most biomolecules have a greater refractive index (n = ~1.5) than buffer solutions (n = 1.33).[2] Therefore, the presence of targeted biomolecules on the resonator surface alters the effective refractive index ($n_{eff,}$) leading to quantitative shifts of the resonant wavelength. In **Fig. 2.5**, the red arrow indicates a corresponding red-shift of the WGM resonance in response to surface functionalization and binding events.

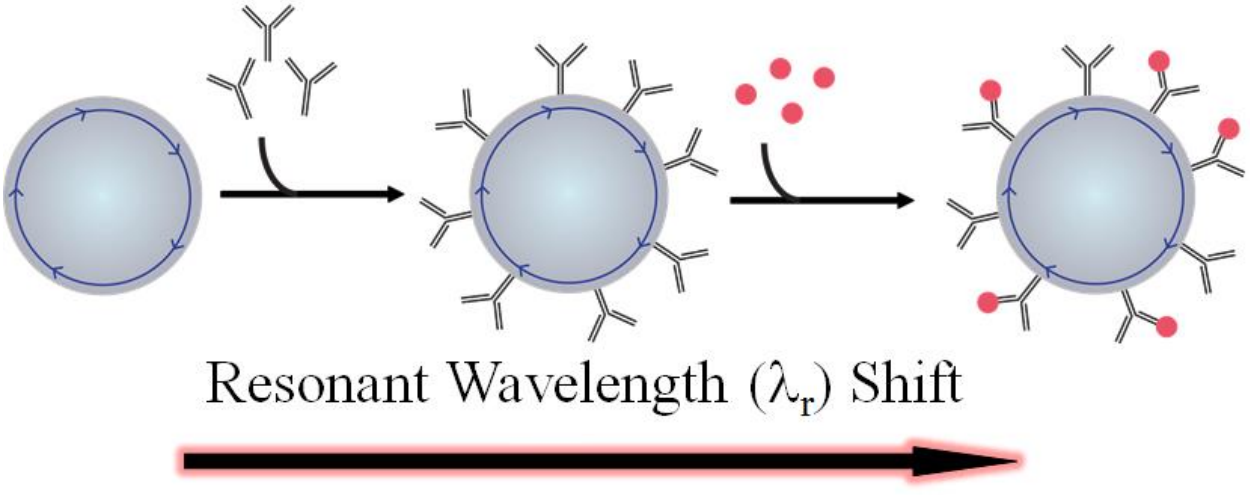

Figure 2.5. Schematic of a WGM biosensor. Biological recognition elements, such as monoclonal antibodies, are covalently attached to the surface of glass microspheres. Binding events between the target protein and immobilized antibody red-shift the WGM resonance (red arrow). The magnitude of the resonant wavelength shift can be used to quantify the amount of bound target protein.

Equation 2.4 illustrates the importance of the relative resonant wavelength shift for WGM sensing rather than the absolute wavelength value. The magnitude of the resonant wavelength shift is given by **Eq. 2.4**:[1, 4]

$$\frac{\Delta\lambda}{\lambda} = \alpha_{ex} \frac{\sigma}{\varepsilon_0(n_s^2 - n_m^2)R_0}$$ **Equation 2.4**

where σ is the surface coverage of target molecules, n_s is the cavity refractive index, n_m is the refractive index of the surrounding medium, α_{ex} is the excess polarizability, and r is the resonator radius. Since a change in excess polarizability due to a biomolecule binding event is proportional to the molecular weight, resonant wavelength shifts can be used to quantitatively determine the amount of target molecules in solution.

When considering the performance of WGM resonators for sensing applications, it is important to consider several factors. Optical resonators are gaining interest for sensing applications due to their small size and long effective path lengths which result in sensitive label-free detection platforms.

2.3 Performance Metrics of Whispering Gallery Mode Resonators

Whispering gallery mode resonators have several sensing advantages over alternative label-free methods. Performance factors discussed in the following sections include quality factors (Q-factors), effective path length, mode volume, and finesse.

2.3.1 Quality Factor

A microresonator Q-factor is basic parameter used to characterize resonator performance. Q-factor is directly related to the photon lifetime within the microspherical cavity. The Q-factor is determined by the resonant wavelength (λ_r) divided by the full width half max of the resonant peak ($\delta\lambda_r$), shown in **Eq. 2.5**:

$$Q = \frac{\lambda_r}{\delta\lambda_r}$$ **Equation 2.5**

High Q resonators are able to efficiently trap and recirculate light within the spherical cavity. For sensing applications, high Q's allow for resolution of tiny spectral shifts due to a small number of analyte binding interactions.[7] For microsphere resonators, Q-factor's as high as 8 x 10^9 (at 633 nm) have been reported.[8] To achieve high Q's it is important to minimize light loss. For microsphere resonators, the inherent Q-factor is affected by several loss contributions related to the cavity size, material, and surface conditions. The inherent Q factor of a microcavity has four independent contributions, shown in **Eq. 2.6**:[9]

$$Q^{-1} = Q_{rad}^{-1} + Q_{mat}^{-1} + Q_{s.s}^{-1} + Q_{cont}^{-1} \qquad \textbf{Equation 2.6}$$

These contributions are associated with radiative losses (Q_{rad}), material absorption (Q_{mat}), surface scattering losses ($Q_{s.s}$) and losses due to surface contamination (Q_{cont}). Radiative, or curvature, losses (Q_{rad}) are related to the size of the cavity. These bending losses occur due to the curvature of the cavity shape. As the spherical cavity decreases in size, radiative losses increase exponentially due to the large curvature angles.[9, 10] For an excitation wavelength of 633 nm, bending losses are negligible for microcavities ~10 μm in diameter or larger.[9] In addition to the cavity size, light loss also occurs due to cavity composition. The circulating electromagnetic field can experience loss due to material absorption (Q_{mat}). Cavity surface conditions also affect light loss events. Surface roughness or inhomogeneities contribute to scattering losses ($Q_{s,s}$). Fabrication process contributes to losses through surface contaminants (Q_{cont}). These factors contribute to the inherent Q-factor of WGM resonators. Since the Q-factor is directly related to the number of revolutions, high Q's are desirable for enhanced light-sample interaction lengths, or effective path lengths.

2.3.2 Effective Path Length

The effective path length (L_{eff}) is directly related to the Q-factor as it describes the length over which light-analyte interactions occur. **Equation 2.7** illustrates the relationship:[8]

$$L_{eff} = \frac{Q\lambda_r}{2\pi n}$$ **Equation 2.7**

where λ_r is the resonant wavelength, Q is the Q-factor, and n is the refractive index of the resonator. In contrast with planar waveguides, the effective light-sample interaction length of WGM optical resonators is determined by the number of revolutions supported by the spherical structure, not it's physical size.[2] Therefore, effective path length of WGM resonators can be on the order of centimeters, even though the physical footprint of the detector is micrometers in size.[7] Another desirable performance metric is the mode volume of optical resonators.

2.3.3 Mode Volume

Mode volume (V) describes the field localization, or circulating density of photons, within a WGM resonator.[11] A smaller mode volume is advantageous because it increases the electromagnetic field strength at the WGM resonator surface.[3] Schematically, mode volume can be illustrated as shown in **Fig. 2.6**. A large mode volume, **Fig. 2.6** (left), results in a wide distribution of the electric field in the radial direction. A smaller mode volume, **Fig. 2.6** (right), concentrates the electric field at the sensing surface. For sensing applications, it is desirable to have small mode volumes to enable concentration of the electromagnetic field at the sensor surface. Furthermore, mode volume (V) is directly related to the excitation wavelength (λ). Using shorter excitation wavelengths may be advantageous for achieving smaller mode volumes. Commonly, silicon WGM resonators are excited using ~1500-1600 nm light. For biosensing purposes, we are interested in utilizing a shorter wavelength, 633 nm, for the optimization of sensor performance. It is well agreed upon that high Q-factors and small mode volumes are desirable for sensing applications.[12, 13]

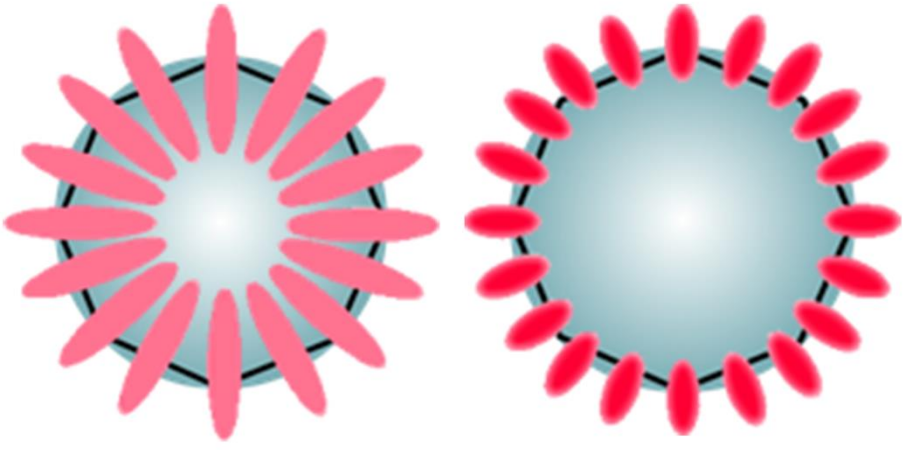

Figure 2.6. Illustration of high (left) and low (right) mode volume for a WGM microsphere resonator. Low mode volumes are advantageous for surface sensing due to the concentration of the mode at the sensor surface, where binding events occur.

Whispering gallery mode resonators are unique sensing platforms due to their ability to achieve high Q-factors and low mode volumes. This combination is desirable for optimization of the biosensor performance, also known as the finesse of the sensing system.

2.3.4 Finesse

Biosensing performance of WGM resonators can be characterized by a particular figure of merit known as finesse (*F*). Finesse is proportional to the Q-factor (*Q*) and inversely proportional to mode volume (*V*), thus, for improved biosensing performance, it is desirable to have high Q microspheres with low mode volumes.[12]

$$F \propto \frac{Q}{V} \qquad \textbf{Equation 2.8}$$

Microresonators are uniquely suited to achieve a high finesse with capabilities of achieving high Q-factors and low mode volumes. Ultra-high-Q microtoroids have been demonstrated to achieve a record finesse value for optical microcavities of ~5 x 10^6.[12]

The desirable characteristics of WGM resonators have generated much interest in developing novel sensing platforms. Over the last two decades, advancements have been made for the optimization of WGM resonator shapes, materials and sensing performance.

2.4 Implementation and Application of High-Q Whispering Gallery Mode Resonators

Whispering gallery mode resonances can be supported in a variety of cavity materials including polymer, glass, and diamond.[3] The flexibility in resonator composition can be used to optimize the performance characteristics and improve sensing applications. **Figure 2.7** highlights cylindrical-, toroidal-, ring- and spherical-shaped geometries, all of which support WGM resonances.[9] These four geometries have been demonstrated as promising platforms for WGM sensing applications. Using these platforms, researchers have demonstrated the detection of a variety of analytes including proteins, DNA, RNA, and viruses. For biosensing applications, each of the geometries has associated advantages and limitations. Performance characteristics are briefly outlined in Table 2.1 and further discussed in the following sections.

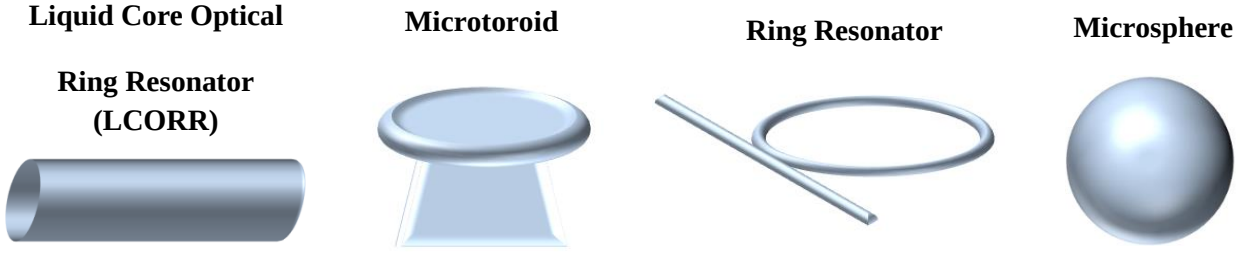

Figure 2.7. Whispering gallery mode resonances can be supported by a variety of spherical geometries including cylinders, toroids, rings, and spheres. These geometries are tens of micrometers in diameter and are commonly used for WGM sensing applications.

Table 2.1. WGM geometries and corresponding biosensing performance metrics.

Optical Resonator Geometry	Detection Limits	Quality Factors	Notes
Liquid Core Optical Ring Resonator (LCORR)[14-16]	10^{-4}- 10^{-7} (RIU) pM – nM	10^3 to 10^5	+ Fluid handling - Not robust - Difficult to multiplex
Microtoroid[17, 18]	nM	$>10^8$	+ Tedious fabrication - Individual functionalization
Ring Resonator[19, 20]	10^{-4} - 10^{-7} (RIU) nM	10^3-10^5	+ Mass fabrication + Compatible with on-chip fluidics + Multiplex capabilities - Individual functionalization - Limited Q-factors
Microsphere[6, 8, 21, 22]	10^{-7} (RIU) nM single virus	10^5 - 10^9	+ Inexpensive + Straightforward fabrication + High Q-Factors - Difficult to multiplex - Fragile system, not robust - Individual functionalization

2.4.1 Liquid Core Optical Ring Resonators (LCORR)

Liquid core optical ring resonators (LCORRs) are able to easily incorporate fluidics as they are fabricated from glass capillaries. A WGM resonance is excited along the perimeter of a thinned capillary wall using a tapered optical fiber.[15] For sensing, the interior of the capillary is functionalized with capture molecules allowing sample fluids to be driven through and contained within the cylinder during an assay. This geometry requires delicate components to be precisely aligned with one another in order to achieve a WGM resonance. To excite the perimeter of the capillary the wall must be extremely thin, approximately 4 μm or less. Capillary walls are thinned by HF etching which is extremely dangerous and time consuming. These requirements limit the throughput and multiplex capabilities of LCORRs. Although fluidic handling is important to clinical applications, LCOOR seems unlikely to ever be a robust system capable of routine implementation. Furthermore the delicate system requires precise alignment, and has

only been reported to achieve moderate performance metrics. A WGM geometry which has shown impressive sensitivities is the microtoroid resonator.

2.4.2 Microtoroid Resonators

Microfabrication methods can be used to prepare 3-D ring resonators, known as microtoroids. Ultrahigh-Q toroidal microcavities have been demonstrated, but require extensive and elaborate fabrication procedures. A combination of photolithography, wet and dry etching, and laser reflowing is required to achieve pristine WGM microtoroid resonators. These extensive procedures require expensive equipment and long procedure times while ultimately resulting in low throughput capabilities. Furthermore, this 3-D structure requires precise alignment of the etched optical fiber for excitation of WGMs. Alignment of this 3-D WGM geometry can be extremely tedious and is not a robust system for routine use. Alternatively, 2-D ring resonators allow for fabrication of a waveguide coupler alongside the WGM device.

2.4.3 Planar Ring Resonators

Planar ring resonators are advantageous because they can be fabricated using well developed standard photolithography techniques. Microfabrication techniques have made mass fabrication of 2-D ring resonators routine and repeatable. Mass fabrication enables multiplexed detection capabilities to be easily integrated with this 2-D geometry. Multiplexed detection has been demonstrated by several groups. Washburn, *et. al.* demonstrated the simultaneous detection of five proteins using silicon photonic microring resonators.[23] Fabrication methods allow for a range of polymer and transparent materials to be used for the optimization of WGM performance and to improve surface chemistry. Using chip-based platforms, fluid handling can be easily integrated with ring-resonator system which is important for clinical applications of these sensors and has enabled the development of commercial instrumentation.

Overall, planar ring resonators have been demonstrated as robust and reliable WGM geometries for biosensing applications. Drawbacks of the technique include reduced quality factors (10^3-10^4) and individual on-chip functionalization. These limitations are easily overcome by microsphere resonators.

2.4.4 Microspheres

Microsphere resonators are widely employed as WGM resonators due to their low costs, ease of fabrication, and high performance characteristics. Using straight forward melting techniques, microspheres can be fabricated in a range of sizes 10-200 μm in diameter, and materials. Microspheres have been demonstrated to achieve high Q-factors (10^8-10^9) due their smooth surfaces.[3, 9] Furthermore, this WGM geometry has demonstrated excellent detection capabilities by measuring single molecules on the resonator surface.[1, 24, 25]

As shown in **Fig. 2.4**, typical measurements of these formed microspheres require precise alignment of the resonator with a thin optical fiber. This approach makes multiplexing very difficult to accomplish given the limitations of transmission measurements. Since the signal collection occurs at the end of the fiber, each light guide can only reliably be used to excite and measure a single microsphere. Even if multiple resonators were aligned on a single taper, only one resulting signal would be measured by the detector. These constraints limit throughput and multiplex capabilities when using this approach for WGM resonators. We hope to address these limitations by developing an improved WGM detection scheme. Ultimately, we would like to combine the desirable performance metrics of microsphere resonators with the ease of use and multiplexed capabilities of planar ring resonators.

2.5 Opportunities for Microsphere Whispering Gallery Mode Resonators

Of the available geometries, microsphere resonators offer an appealing platform for assay development since they are inexpensive, commercially available or easily fabricated, formed in a variety of sizes and materials, and are easily functionalized. Moreover, microspheres have exquisitely smooth

surfaces, low material absorption, and minimal reflection losses which lead to quality (Q) factors that can be orders of magnitude larger than other resonator designs. Large Q values translate into long effective path lengths and narrow resonances, both of which are highly desirable in sensing applications. Microsphere resonators, however, present challenges for integration into multiplexed sensing schemes when traditional, transmission based approaches are used for measuring WGM resonances. In an effort to combine their favorable optical attributes with multiplexed sensing capabilities, we recently reported a fluorescence imaging scheme for simultaneously measuring individual WGM resonances from a field of microspheres.

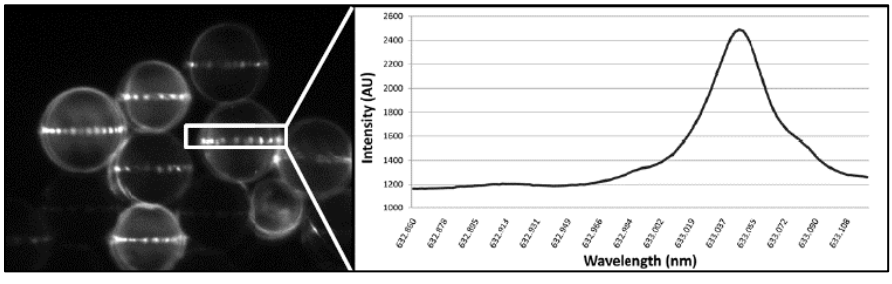

Figure 2.8. Whispering gallery mode imaging approach utilizing a fluorescent dye molecule covalently attached to the surface of microsphere resonators for the determination of WGM resonance location and intensity.

The approach takes advantage of the evanescent field generated at the sphere surface when a WGM resonance is excited. By functionalizing the surface of the sphere with a fluorescent dye, distinct fluorescence rings are observed when a particular sphere comes into resonance. Using fluorescence imaging, large numbers of spheres can be simultaneously characterized as the excitation wavelength is scanned, providing a new approach for multiplexed detection. WGM imaging, further discussed in Chapter 3, provides a flexible and powerful biosensing scheme capable to imaging and quantifying WGM shifts from numerous microspheres within the field of view.

2.6 Overview of Dissertation

Whispering gallery mode optical resonators provide sensitive label-free detection capabilities due to the recirculation of light at the spherical interface. The resulting evanescent wave can sense surface binding events with enhanced light-sample interaction due to long effective path lengths. Traditional analysis methods require thin, tapered fibers to excite WGM resonances. These delicate systems limit multiplex capabilities. To overcome these limitations, we have developed a fluorescence imaging approach for detecting WGM resonances. This imaging approach allows tens to hundreds of optical microcavities to be excited and utilized in a single assay. Chapter 3 discusses our improved WGM biosensing platform which we have utilized to simultaneously detect three putative ovarian cancer biomarkers: osteopontin, prolactin and CA-125. Furthermore, the label-free platform allows for the detection of non-protein targets. Numerous nucleic acid markers have been identified as promising markers for early detection, tumor staging, and for monitoring disease recurrence.[26-28] Using WGM imaging, we detected miRNA miR-142-3p, a nucleic acid marker of ovarian cancer.

Multiplexed capabilities of optical microcavities are further complimented by their compact sizes. Their miniature size, tens of micrometers in diameter, enables hundreds of microsphere resonators to be incorporated in small volumes. Incorporating numerous resonators in small volume systems is important for reducing assay sample requirements. Rapid, real-time detection of picomolar protein concentrations in small volume droplets was completed to demonstrate the potential of WGM imaging.

Chapter 5 characterizes properties of microsphere resonators to optimize approaches for improved label-free sensing using WGM resonators. Microsphere resonators fabricated from optical fibers achieve impressive performance metrics. In some cases, these resonators showed a 10x improvement in refractive index sensitivity compared to commercially available barium titanate microspheres. Individual microsphere fabrication is not ideally suited for multiplexed assays which require a large number of microspheres. However, the improved performance is advantageous for the development of novel biosensing platforms.

In addition to developing improved biosensing platforms to meet clinical needs, we are also interested in utilizing microsphere WGM resonators for the development of novel sensing instrumentation. The label-free sensing capabilities of WGM microspheres can be applied to the development of novel analytical tools. For example, single, unmodified resonators can be incorporated with scanning probe microscopy in order to investigate surface refractive index changes. Chapter 6 discusses the development and optimization of this new technique termed scanning resonator microscopy (SRM). The developed analytical technique integrates WGM sensing with atomic force microscopy. Scanning resonator microscopy is capable of simultaneously imaging topography and optical properties by scanning a WGM microsphere resonator across a sample surface. This technique provides high-content information about a sample as it senses surface refractive index changes through WGM resonance shifts. Initial investigations demonstrate the potential of the technique to characterize material samples such as thin film polymers. In Chapter 7, we discuss applying SRM to biological samples. The label-free detection capabilities provide a powerful scanning probe technique for the characterization of protein modified surfaces, such as protein microarrays, or label-free cellular assays.

2.7 References

1. Vollmer, F.; Arnold, S., Whispering-Gallery-Mode Biosensing: Label-Free Detection Down to Single Molecules. *Nature Methods* **2008,** *5* (7), 591-596.
2. Fan, X., et al., Sensitive Optical Biosensors for Unlabeled Targets: A Review. *Anal. Chim. Acta* **2008,** *620* (1-2), 8-26.
3. Ward, J.; Benson, O., WGM Microresonators: Sensing, Lasing and Fundamental Optics with Microspheres. *Laser Photon. Rev.* **2011,** *5*, 553-570.
4. Soria, S., et al., Optical Microspherical Resonators for Biomedical Sensing. *Sensors* **2011,** *11*, 785-805.
5. Yalcin, A., et al., Optical Sensing of Biomolecules Using Microring Resonators. *Selected Topics in Quantum Electronics, IEEE Journal of* **2006,** *12* (1), 148-155.
6. Arnold, S., et al., Shift of Whispering-Gallery Modes in Microspheres by Protein Adsorption. *Opt. Lett.* **2003,** *28* (4), 272-274.
7. Luchansky, M. S.; Bailey, R. C., High-Q Optical Sensors for Chemical and Biological Analysis. *Anal. Chem.* **2011**.
8. Gorodetsky, M. L., et al., Ultimate Q of Optical Microsphere Resonators. *Opt. Lett.* **1996,** *21* (7), 453-455.
9. Chiasera, A., et al., Spherical Whispering-Gallery-Mode Microresonators. *Laser Photonics Rev.* **2010,** *4* (3), 457-482.
10. Quan, H.; Guo, Z., Analyses of Whispering-Gallery Modes in Small Resonators. *Journal of Micro/Nanolithography, MEMS and MOEMS* **2009,** *8* (3), 033060-7.
11. Matsko, A. B.; Ilchenko, V. S., Optical Resonators with Whispering-Gallery Modes-Part I: Basics. *IEEE J. Sel. Top. Quantum Electron.* **2006,** *12*, 3-14.
12. Kippenberg, T. J. A. Nonlinear Optics in Ultra-high-Q Whispering-Gallery Optical Microcavities. California Institute of Technology, 2004.
13. Yoshie, T., et al., Optical Microcavity: Sensing Down to Single Molecules and Atoms. *Sensors* **2011,** *11* (2), 1972-91.
14. Suter, J. D.; Fan, X. In *Overview of the Optofluidic Ring Resonator: A Versatile Platform for Label-Free Biological and Chemical Sensing*, EMBC 2009. Ann. Intl. Conf. IEEE, 3-6 Sept. 2009; 2009; pp 1042-1044.
15. Zhu, H., et al., Analysis of Biomolecule Detection with Optofluidic Ring Resonator Sensors. *Opt. Express* **2007,** *15* (15), 9139-9146.

16. Zhu, H., et al., Opto-Fluidic Micro-Ring Resonator for Sensitive Label-Free Viral Detection. *Analyst* **2008,** *133* (3), 356-360.
17. Ozgur, E., et al., Label-Free Biosensing with High Selectivity in Complex Media using Microtoroidal Optical Resonators. *Sci Rep* **2015,** *5*, 13173.
18. Armani, D. K., et al., Ultra-High-Q Toroid Microcavity on a Chip. *Nature (London, U. K.)* **2003,** *421* (6926), 925-928.
19. Choi, S. J., et al., Microring Resonators Vertically Coupled to Buried Heterostructure Bus Waveguides. *Trends Opt. Photonics* **2003,** *91* (Integrated Photonics Research), 151-154.
20. Washburn, A. L., et al., Label-Free, Multiplexed Biomolecular Analysis Using Arrays of Silicon Photonic Microring Resonators. *Procedia Eng.* **2011,** *25*, 63-66.
21. Vollmer, F., et al., Single Virus Detection from the Reactive Shift of a Whispering-Gallery Mode. *Proc Natl Acad Sci U S A* **2008,** *105* (52), 20701-20704.
22. Hanumegowda, N. M., et al., Refractometric Sensors Based on Microsphere Resonators. *Appl. Phys. Lett.* **2005,** *87* (20), 201107.
23. Washburn, A. L., et al., Quantitative, Label-Free Detection of Five Protein Biomarkers Using Multiplexed Arrays of Silicon Photonic Microring Resonators. *Anal. Chem.* **2009,** *82* (1), 69-72.
24. Armani, A. M., et al., Label-Free, Single-Molecule Detection with Optical Microcavities. *Science* **2007,** *317* (5839), 783-787.
25. Vollmer, F., et al., Protein Detection by Optical Shift of a Resonant Microcavity. *Appl. Phys. Lett.* **2002,** *80* (21), 4057-4059.
26. Iorio, M. V., et al., MicroRNA Signatures in Human Ovarian Cancer. *Cancer Res.* **2007,** *67*, 8699-8707.
27. Ferracin, M., et al., Micromarkers: miRNAs in Cancer Diagnosis and Prognosis. *Expert Rev. Mol. Diagn.* **2010,** *10*, 297-308.
28. Calin, G. A.; Croce, C. M., MicroRNA Signatures in Human Cancers. *Nat. Rev. Cancer* **2006,** *6* (11), 857-866.

Chapter 3

Whispering Gallery Mode Imaging for the Multiplexed Detection of Putative Ovarian Cancer Biomarkers

Portions of the chapter were previously published in Biosensors and Bioelectronics: Wildgen, S.; Huckabay, H.; Dunn, R. Label-free Detection of Ovarian Cancer Biomarkers Using Whispering Gallery Mode Imaging. Biosens Bioelecton. 2013, 45, 223-229.

3.1 Introduction

Small optical microresonators that support whispering gallery mode (WGM) resonances offer powerful biosensing capabilities. These resonators respond to changes in refractive index and offer many advantages for label-free sensing. Here, we report a fluorescence imaging scheme for measuring WGM resonators using excitation light coupled into a Dove prism. Fluorescence imaging of WGM resonances offers the potential for large scale multiplexed detection which is demonstrated by simultaneously exciting and imaging hundreds of microsphere resonators. For multiplexed applications, analyte identity can be encoded in the resonator size and/or location. By encoding analyte identity into microresonator size, we simultaneously quantify three putative ovarian cancer biomarkers in a single PBS assay. Additionally, the label-free approach enables the homogeneous detection of proteins, nucleic acids, or other markers of disease without the use of labels. We explore the application of WGM imaging for the detection of microRNA (miRNA), small non-coding RNA molecules, which have been identified as promising markers of disease. The development of WGM imaging is discussed as well as application of the technique to detection of putative ovarian cancer protein and miroRNA biomarkers.

3.1.1 Development of Whispering Gallery Mode Imaging

To combine high Q-factors of microsphere resonators with multiplexed detection capabilities, we have developed a WGM imaging approach. By covalently attaching fluorescent dye molecules to the surface of glass microspheres, sensitive fluorescent imaging can be used to analyze a field of WGM resonators. Light evanescently coupled into microsphere resonators excites surface attached dye. When the excitation wavelength matches a WGM resonance, a bright intensification of fluorescence signal is visible, **Fig. 3.1**.

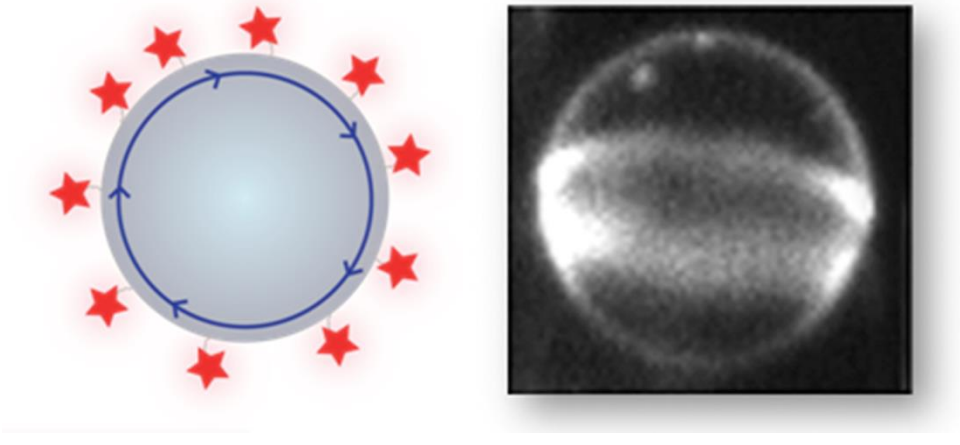

Figure 3.1. To image WGM microsphere resonances, fluorophores are covalently attached to the glass surface. Light evanescently coupled into the microsphere resonator excites the surface attached dye providing a bright intensification of the fluorescent signal when a WGM resonance is achieved.

Previously, we demonstrated fluorescence imaging of WGM resonances using the evanescent field from a total internal reflection (TIR) microscope to launch light into a field of dye labeled microsphere resonators.[1] The high numerical aperture objective needed to create the TIR field, however, limited the number of microspheres that could be simultaneously excited, increased the cost of the apparatus, and lowered the excitation coupling efficiency into the microresonators. Here we show that a much simpler arrangement, shown schematically in **Fig. 3.2**, overcomes these drawbacks. As shown by others, prism couplers can efficiently launch light into microresonators.[2-4] A Dove prism is used to launch WGMs in a

collection of microspheres which simplifies the experimental design, lowers the cost, and enables improved phase matching conditions.

As shown in **Fig. 3.2**, excitation light is directed into a Dove prism which creates the evanescent field used to excite a large field of microsphere resonators. Excitation from a computer controlled tunable diode laser is sent into a Dove prism which directs light towards the microsphere resonators at an approach beyond the critical angle. Total internal reflection creates an evanescent field at the prism interface that couples light into the microsphere resonators. Circumnavigating light within each sphere creates an evanescent wave at the surface which excites the fluorescent dye attached to the microsphere, shown in **Fig. 3.1**. As the wavelength of the laser is tuned, WGM resonances lead to an enhanced band of fluorescence around the sphere equator. The fluorescence is collected from above, filtered, and imaged on a charge-coupled device (CCD) camera. Using this approach, the individual WGM excitation spectrum for each sphere in the field of view can be measured as the diode laser wavelength is scanned.

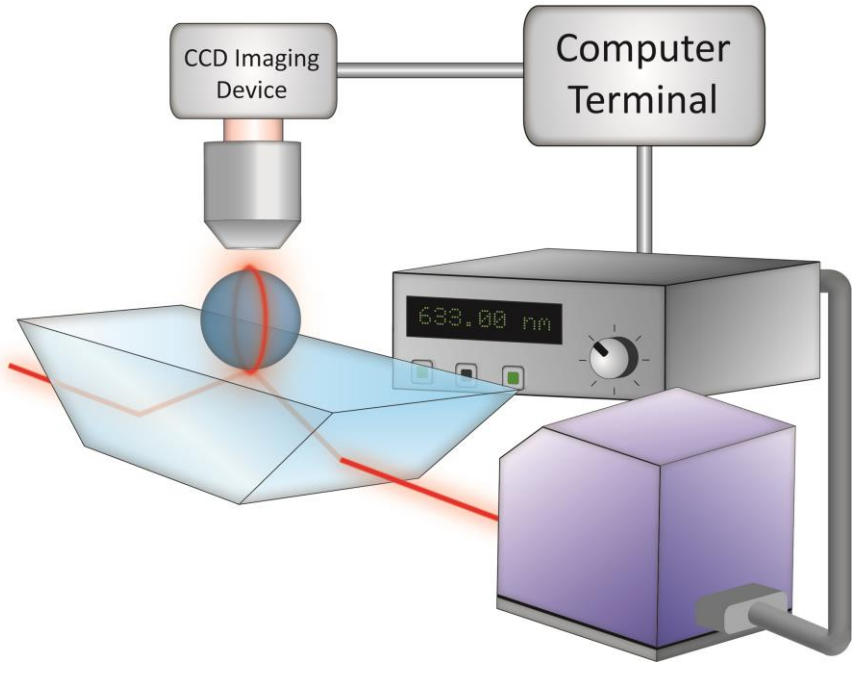

Figure 3.2. Schematic of the instrumental arrangement used for the fluorescence imaging of WGM resonances from a field of microsphere resonators. Light from a tunable diode laser is sent into a Dove prism which directs light towards the interface where it undergoes total internal reflection (TIR). The associated evanescent field is used to couple light into microsphere resonators dispersed at the interface. When a specific sphere comes into resonance with the excitation source, the large increase in light circumnavigating the sphere excites the surface attached fluorescent dye. This leads to a distinctive stripe of fluorescence from the sphere which is imaged from above and detected on a CCD camera.

To illustrate the WGM spectral sensitivity of this technique, **Fig. 3.3** shows a series of fluorescence images collected from the same field of microsphere resonators as the excitation wavelength of the diode laser is scanned ~0.2 nm. As the excitation wavelength is tuned, several spheres undergo large increases in fluorescence intensity indicative of a WGM resonance. For example, the microsphere denoted by the arrow is dark in the first image (**Fig. 3.3A**), comes into resonance in the middle image (**Fig. 3.3B**), and then goes dark again in the third image (**Fig. 3.3C**). Spheres which exhibit weak fluorescence throughout the images have resonances outside the excitation window shown. During WGM imaging, a series of images are collected. The excitation spectra of individual microspheres can be extracted from the

collected images allowing the fluorescence intensity to be plotted as a function of the excitation wavelength range. **Figure 3.3** includes a representative WGM spectra corresponding to the microsphere denoted by the arrow. Within the spectra, the red lines indicate data points corresponding to the three representative fluorescent images. By plotting the fluorescence signal from a particular microsphere collected in a series of images, the WGM resonance can be identified by a sharp increase in intensity, as shown below.

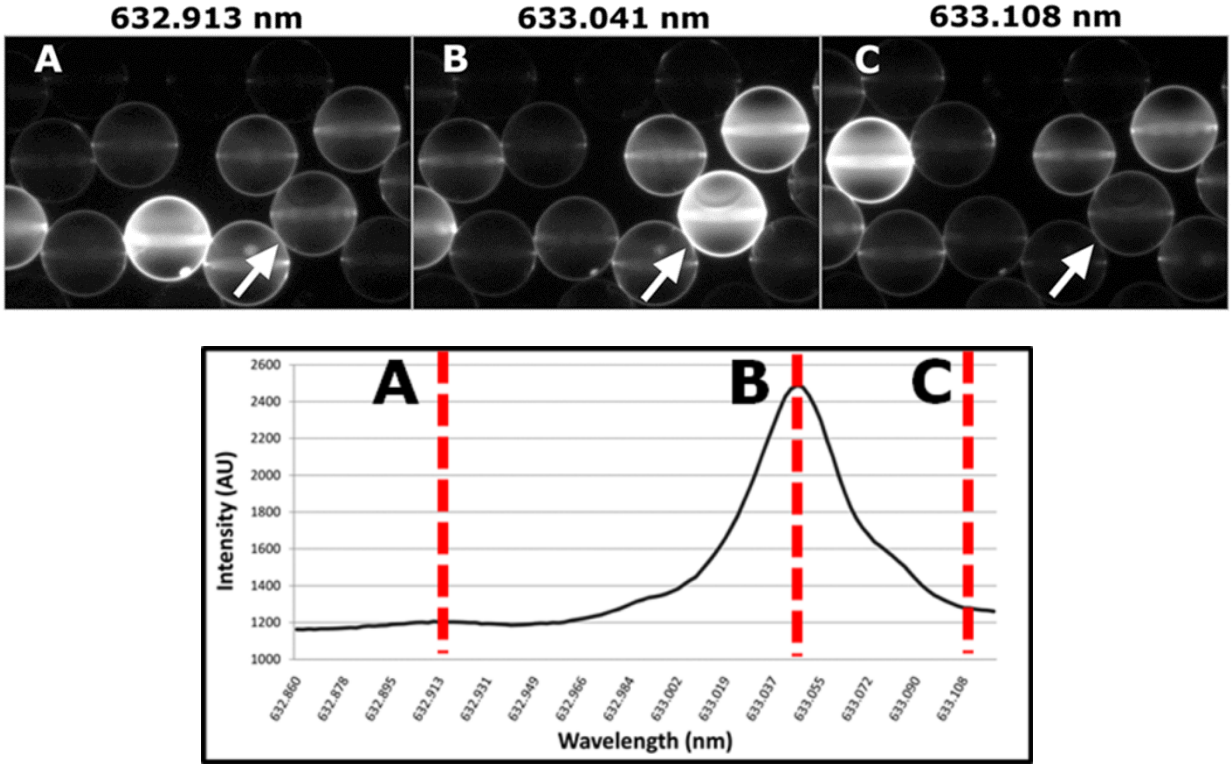

Figure 3.3. Fluorescence image snapshots of the same field of microsphere resonators collected following excitation at the wavelengths denoted. Individual spheres become bright and dark across the panels as they come in and out of resonance with the excitation wavelength. For example, the sphere denoted by the arrows reveals a large enhancement in its fluorescence in the middle image (B), denoting a WGM resonance at or near 633.041 nm. By collecting a series of images, individual WGM spectrum for each sphere in the image can be extracted. The resonant wavelength is identified by plotting intensity of the WGM resonance as a function of excitation wavelength.

For sensing applications, combining high-Q microsphere resonators with fluorescence detection offers a label-free approach for the detection of proteins, nucleic acids, and other species of interest. Low cost, high Q-factors, and wide commercial availability of microspheres in various materials facilitates the adoption of this approach. To validate this method, results and progress on the development of WGM imaging biosensors for the early detection of ovarian cancer are presented in this chapter. To demonstrate multiplexed capabilities, three putative ovarian cancer markers are detected using whispering gallery mode imaging. Furthermore, initial results are presented for the detection of miRNA miR-142-3p.

3.2 Materials and Methods

3.2.1 Materials

Barium titanate glass microspheres were obtained from Mo-Sci Corporation (Rolla, MO). Anti-CA-125 mouse monoclonal antibodies, anti-osteopontin monoclonal antibodies, and osteopontin protein were purchased from Abcam (Cambridge, MA). CA-125 ovarian tumor marker antigen was obtained from MP Biomedicals (Solon, OH). Anti-prolactin monoclonal antibodies and prolactin protein were purchased from R&D Systems (Minneapolis, MN). MicroRNA miR-142-3p and biotinyled complimentary strand were purchased from Integrated DNA Technologies (Coarlville, IA). Streptavidin, Alexa Fluor 633 conjugate was purchased from Life Technologies, Thermo Fisher Scientific (Grand Island, NY). All were used without further purification. The amine reactive succinimidyl ester of the Alexa 633 fluorescent dye was obtained from Invitrogen Corporation (Carlsbad, CA), and perfusion chambers were obtained from Grace Bio-Labs (Bend, OR). StartingBlock blocking solution was obtained from Thermo Pierce Products (Rockford, IL). All other reagents, unless otherwise noted, were purchased from Fisher Scientific (Hampton, NH) and used without further purification.

3.2.2 Preparation of Microsphere WGM Sensors

Barium titanate microspheres with 38 ±3 μm, 53 ±4 μm, and 63 ±4 μm diameters were prepared separately. Each sphere size was soaked in a 10% Contrad™ 70 Liquid Detergent solution in 18 MΩcm nanopure water for 1 hr. and triply rinsed with nanopure water. The spheres were then incubated in a 30% hydrogen peroxide solution for 1 hr. to increase the number of hydroxyl groups on the surface.[5] After triply rinsing with nanopure water, ethanol, and toluene, the spheres were tumbled overnight in 6% (3-aminopropyl)triethoxy silane (APTES) in toluene, and triply rinsed in toluene and ethanol to form an amine terminated surface. For protein detection, antibodies were attached to the spheres.

For antibody attachment, microspheres were subsequently tumbled for 2 hr. in 6% glutaraldehyde solution in PBS, triply rinsed with PBS, then incubated overnight (~4 ^{0}C) with the desired monoclonal antibodies for the immobilization of capture agent onto the sensor surface. Microspheres were triply rinsed with PBS and labeled with ~10 ng/mL Alexa 633 fluorescent dye in 0.1 M sodium bicarbonate buffer. In order to block non-specific adsorption sites, the spheres were tumbled for 2 hr. in a StartingBlock solution containing 5% BSA, 5% sucrose (w/v %) and refrigerated prior to use.

For miRNA detection, microspheres were tumbled for 2 hr. in 6% glutaraldehyde solution in PBS, triply rinsed with PBS, then incubated overnight (~4 ^{0}C) with streptavidin conjugated Alexa Fluoro A633 for the immobilization of the fluorescently labeled protein onto the resonator surface. Microspheres were triply rinsed with PBS and tumbled for 2 hr. in StartingBlock solution. After blocking reactive sites on the resonator surface, microspheres were incubated with biotinylated single stranded RNA which was a complimentary sequence to the target miR-142-3p. Once the capture strand was immobilized on the sensor surface, microspheres were refrigerated prior to use.

3.2.3 WGM Imaging Measurements

Functionalized microsphere resonators were deposited into polydimethylsiloxane (PDMS) wells adsorbed to glass coverslips, enclosed in a CoverWell perfusion chamber, and subsequently immersed in

solution (1:1 solution of PBS:serum or PBS). Coverslips were placed above a BK7 Dove prism (Edmund Optics, Barrington, NJ) coated in high index immersion oil which was mounted onto a three-axis robotic micromanipulator (MP-285, Sutter Instruments, Novato, CA). Light from an external cavity diode laser (TLB-6904, Newport Corporation, Irvine, CA) was free space coupled into the Dove prism creating an evanescent field at the center of the prism for launching light into the microresonators. Fluorescence was collected from above the sample with an upright microscope (Olympus BXFM, Center Valley, PA) equipped with a 10x UMPlanFL (0.3 NA) objective lens (Olympus), filtered (Chroma Technology, Bellows Falls, VT), and imaged on a CCD camera (Cascade 650, Roper Scientific, Tucson, AR). Diode laser scanning was controlled using LabVIEW (National Instruments, Austin, TX) and image collection and processing was performed with SlideBook software (Version 4.2.0.3, Intelligent Imaging Innovations, Denver, CO). The resonant wavelengths of single spheres were measured in triplicate and error bars indicate standard deviation, bars smaller than the marker size were found to range from ±0.059 pm to ±3.6 pm.

3.3 Results and Discussion

3.3.1 Label-Free Sensing Using Whispering Gallery Mode (WGM) Imaging

Before applying WGM imaging to the detection of biomarkers, it was important to demonstrate WGM imaging approach for measuring refractive index changes. To explore sensing capabilities, fluorescence measurements were made to determine the location of the microsphere's resonant wavelength as the surrounding refractive index was systematically changed. Dye functionalized microspheres were immersed in aqueous solution and fluorescent images were collected as the tunable light source was scanned. Injections of absolute ethanol were added to increase the surrounding refractive index. **Figure 3.4** illustrates resonant wavelength shifts in response to increasing solution refractive index. With tiny alterations of the solution refractive index (Δn = 0.0008 RIU), small shifts or the resonant wavelength (~10 pm) were measured using WGM imaging.

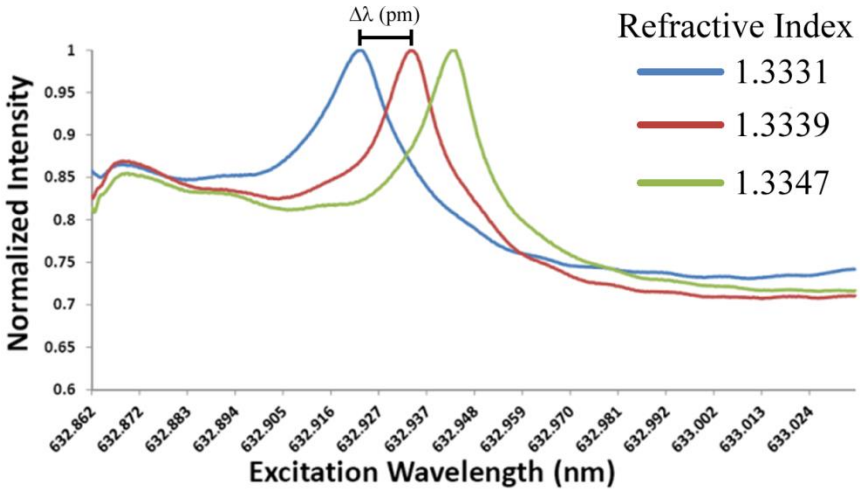

Figure 3.4. Excitation spectra of fluorescence intensity with excitation wavelength extracted from a series of fluorescence images. Enhanced fluorescence intensity from an individual WGM resonator identifies the resonant wavelength value. By systematically changing the bathing solution surrounding the microspheres, shifts of the resonant wavelength are measured.

The spectral shifts illustrate small refractive index changes correspond to measureable shifts in the WGM resonant wavelength (pm). To quantify these shifts, a typical calibration plot measured for a fluorescently labeled glass microsphere is shown in **Fig. 3.5**. As expected from the resonant condition equation (**Eq. 2.3**), the plot of resonant wavelength (λ_r) versus refractive index (n) is linear (R^2=0.998), with a measured sensitivity of 10 nm/ RIU. This sensitivity is typical for WGM resonators and, importantly, higher than what is achieved using SPR. The high sensitivity of WGM microsphere resonators to refractive index changes further illustrates why microsphere resonators are appealing label-free sensors.

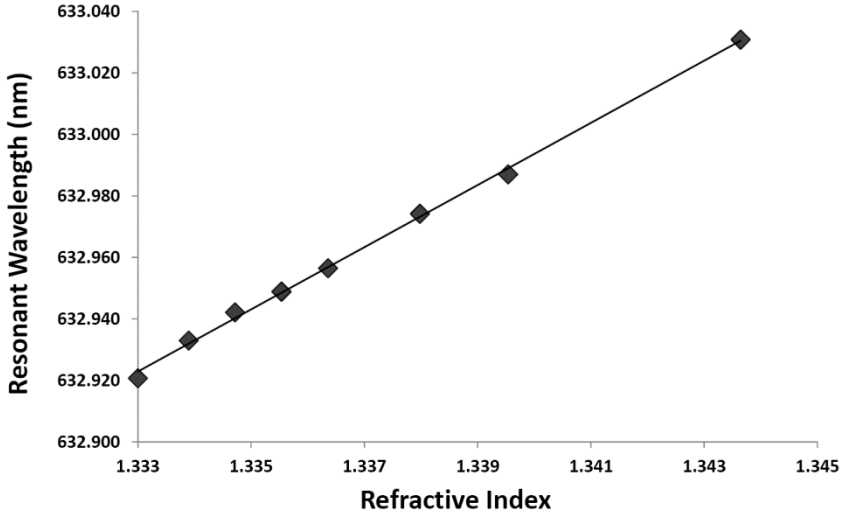

Figure 3.5. Calibration plot of resonant wavelength shifts as a function of solution refractive index. Refractive index was altered by injections of absolute ethanol to the bathing solution surrounding microsphere resonators. Using WGM imaging, a sensitivity of 10 nm/ RIU was measured (R^2 =0.998).

Having validated the use of WGM imaging for monitoring resonant wavelength shifts through fluorescence imaging, we extended measurements to biosensing applications. As discussed in Chapter 2, for the development of WGM biosensing platforms, microsphere surfaces are covalently modified with molecular capture agents, **Fig. 3.6**. A surface binding event between the target and capture molecules results in an effective refractive index change, thus, providing a measurable shift in the WGM resonant wavelength.

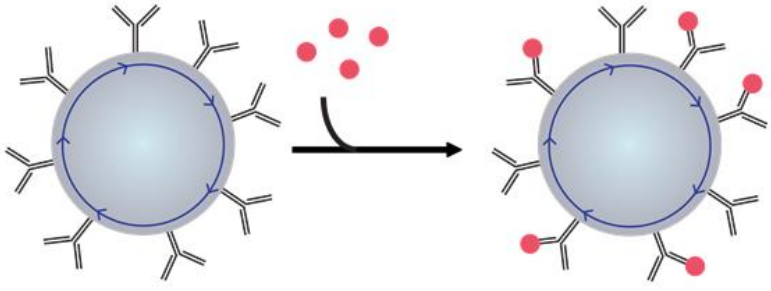

Figure 3.6. Illustration of surface functionalization of microsphere resonators for biosensing applications. Capture molecules, such as monoclonal antibodies, are covalently attached the glass surface. When immersed in a sample solution, targeted analytes will bind to the modified microspheres. Surface binding events alter the effective refractive index of the microsphere environments. These alterations are detected through resonant wavelength shifts to longer values.

Compared to traditional WGM biosensing platforms, the WGM imaging approach simplifies microsphere functionalization as surface modifications are completed prior to loading resonators into the assay. Furthermore, by using the same fluorescent marker for all microsphere resonators, equipment costs are decreased while assay flexibility is increased. We were interested in applying WGM imaging to the detection of putative ovarian cancer biomarkers. Previously we demonstrated WGM imaging could be used to quantify levels of TNF-α and ovarian cancer marker CA-125 in buffer.[1] Here we extend those measurements and show that CA-125 levels can be quantified in clinically relevant serum samples using the WGM imaging approach.

3.3.2 WGM Imaging for the Detection of Ovarian Cancer Biomarkers

Label-free detection schemes, like the one developed here, are generally susceptible to interferences arising from non-specific binding.[6] These can be problematic for label-free approaches and often pose significant challenges for developing new bioassays. It is important, therefore, to show that these effects can be minimized such that analytes can be detected and quantified in complicated matrices at

biologically relevant levels. To show that these effects can be minimized, **Fig. 3.7** displays a calibration plot for the detection of CA-125 in serum using microspheres pre-treated with a modified blocking agent. The fluorescently labeled and blocked microspheres were functionalized with anti-CA-125 monoclonal antibodies and immersed in a 1:1 solution of PBS:serum. Sequential injections of CA-125 antigen in a 1:1 solution of PBS:serum were added and the resonant wavelength shifts due to antigen binding were recorded to generate the calibration curve shown in **Fig. 3.7**. The linear response has a measured sensitivity of 1.8 pm / U/mL, a detection limit of ~1.8 U/mL, and a limit of linearity of ~10 U/mL. By way of comparison, commercial ELISA kits for CA-125 typically report detection limits of ~5 U/mL (Panomics). These results suggest that modified blocking agents are sufficient to minimize non-specific binding and enable the collection of linear calibration curves in complicated biological fluids using the fluorescence imaging of WGM resonances.

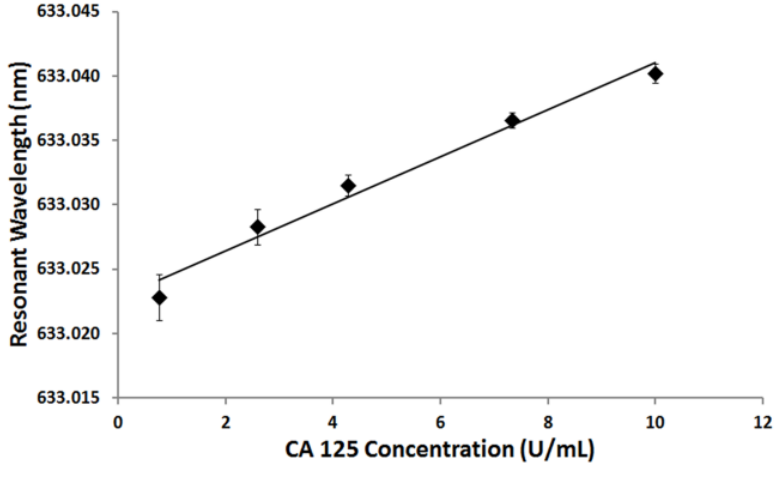

Figure 3.7. Calibration plot for the detection of the ovarian cancer marker CA-125 in serum using 63 μm spheres. Dye labeled microspheres coated with CA-125 monoclonal antibodies were immersed in a 1:1 solution of serum:PBS and subjected to sequential injections of CA-125. From the linear calibration plot (R^2 = 0.98), the measured sensitivity is 1.8 pm / (U/mL) with a detection limit of ~1.8 U/mL CA-125 and limit of linearity of ~10 U/mL. Error bars represent intra assay variability (N = 3).

Detection of CA-125 in serum was an important step in validating the label-free sensing platform in physiological fluids. To further extend these measurements, CA-125 was quantified in patient serum samples. Using standard addition assays, WGM imaging was able to quantify the levels of CA-125 in both a healthy and disease patient serum sample, **Fig. 3.8** (unpublished data). The disease patient was found to have an elevated level of CA-125 of 316 U/mL (R^2 = 0.98). While the healthy patient had a measured level of 42 U/mL (R^2 = 0.94).

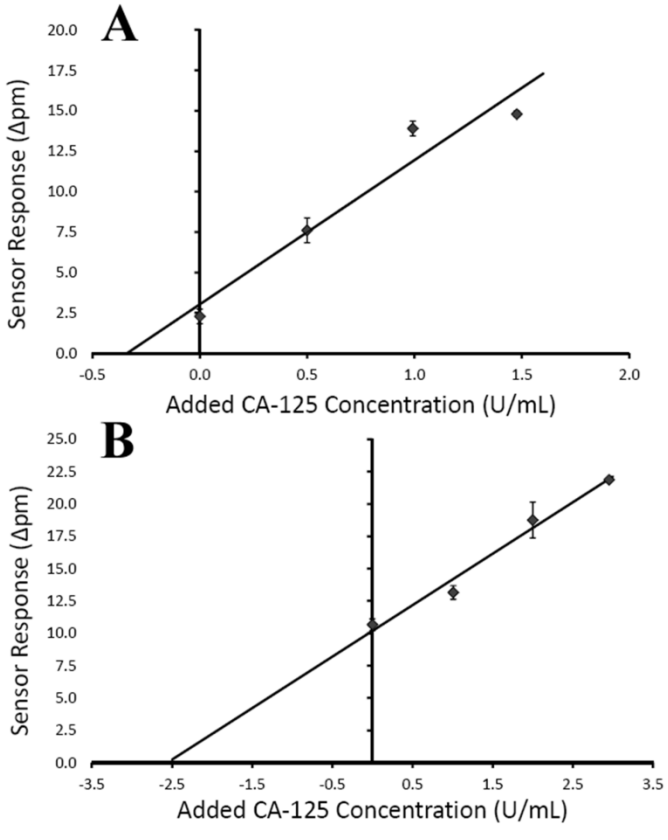

Figure 3.8. Detection of CA-125 in serum patient samples. (A) A healthy patient had a measured CA-125 level of 42 U/mL (R^2 = 0.94) which is higher than the diagnostic cut off of 35 U/mL. This supports the need for multiplexed diagnostic technologies in order to strengthen an early diagnosis. (B) A disease patient had an elevated CA-125 level of 316 U/mL (R^2=0.98). Error bars represent intra assay variability (N = 3). Results were collected by former lab member Heath Huckabay.

Although classified as a healthy patient sample, the measure CA-125 level of 42 U/mL is above the clinical cut off of 35 U/mL.[7] This illustrates the difficulties of achieving an accurate diagnosis of ovarian cancer using CA-125 alone. For a more accurate diagnosis, multiple markers need to be quantified in a single assay.[8-11] We hope to utilize WGM imaging for the multiplexed detection of putative ovarian cancer biomarkers.

3.3.3 WGM Imaging for Multiplexed Detection of Putative Ovarian Cancer Biomarkers

Since the imaging approach enables large numbers of resonators to be simultaneously measured, significant multiplexing capabilities can be envisioned. As an example, **Fig. 3.9** shows a fluorescence image of a 547 μm x 445 μm field of view containing over 120 microspheres. For multiplexed measurements, analyte identity can be encoded into the sphere size, location or both. An example of the former is illustrated in **Fig. 3.9**, which contains a mix of spheres with diameters of 38 μm, 53 μm, and 63 μm. Spheres of each size class were collectively functionalized with a monoclonal antibody specific for a putative biomarker associated with ovarian cancer. For the image shown in **Fig. 3.9**, the selected antibodies targeted the putative ovarian cancer markers OPN (38 μm), CA-125 (53 μm), and prolactin (63 μm). Serum prolactin levels have shown to be significantly elevated in women with ovarian cancer, especially in women with a strong family history of the disease.[12] Additionally, osteopontin is overexpressed in tumors and serum of newly diagnosed ovarian cancer patients providing a complimentary marker to CA-125 for diagnostics.[13-15]

Furthermore, prolactin, OPN, and CA-125 have all been shown to be significantly elevated in serum samples from epithelial ovarian cancer patients.[16-19] One study also showed that all three biomarkers are elevated during early stages of the disease for at-risk populations, classifying them as potential diagnostic markers for early detection of ovarian cancer.[12] Subsequent reports indicated the latter study to be controversial due to overestimated results indicating a positive predictive value of 99.3%. This calculated value failed to account for the low prevalence of the disease (1.4%) in the general population.[20, 21] After

recalculation, the positive predictive value was only 6.5%, thus, the panel fails to meet the requirements of an accurate screening test for the general population.[21]

Microspheres were functionalized with the appropriate monoclonal antibody and Alexa 633 dye as described in the experimental section. Sphere sizes were combined, blocked using the previously outlined procedure, and placed on a glass substrate for analysis. Correlating WGM shifts with sphere size, therefore, enables specific biomarker quantification in mixed assays such as that shown in **Fig. 3.9**.

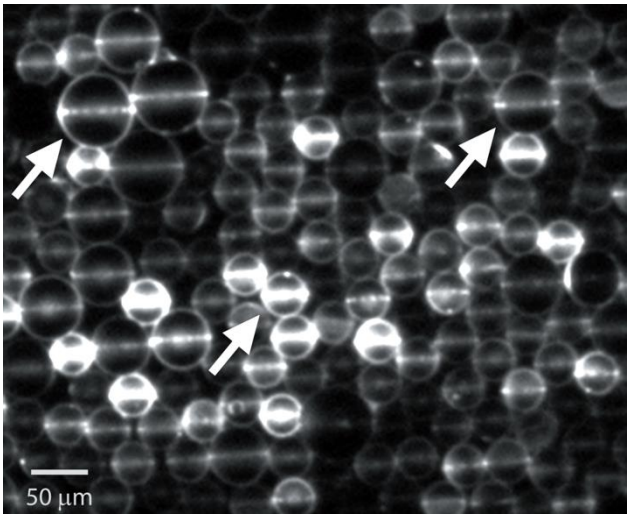

Figure 3.9. Snapshot of a field of fluorescently labeled microspheres extracted from a series of images collected as the excitation wavelength is scanned. The 547 μm x 445 μm field of view contains over 120 dye labeled microspheres consisting of a mix of 38 μm, 53 μm and 63 μm diameter sizes. Analyte identity is encoded into the sphere size, which is clearly resolved in the imaging approach (arrows). Some resonators exhibit enhanced bands of fluorescence indicating their resonant condition more closely matching the excitation wavelength associated with this particular snapshot. The individual WGM spectrum for each sphere in the image, therefore, can be extracted from a series of images collected as the excitation wavelength is scanned, illustrating the high multiplexing potential of this approach.

Before multiplexed measurements can be validated, cross reactivity between the antibody-antigen pairs must be explored. To probe these possible effects, calibration plots for all three sphere sizes following injections of a single antigen solution in PBS were measured. The calibration plots in **Fig. 3.10** show the results from these measurements following injections of OPN (**Fig. 3.10A**), CA-125 (**Fig. 3.10B**), and prolactin (**Fig. 3.10C**). In each case, only the sphere size functionalized with the antibody specific for the added antigen showed a linear response, indicating that cross reactivity is not significant among these antibody-antigen pairs. The calibration plot in **Fig. 3.10A** for OPN (38 μm sphere) has a measured sensitivity of 14 pm / ng/mL and a detection limit of ~270 pg/mL. For CA-125 (53 μm sphere) shown in **Fig. 3.10B**, the measured sensitivity is 13 pm / U/mL with a detection limit of ~0.11 U/mL while that for prolactin (63 μm sphere) in **Fig. 3.10C** reveals a sensitivity of 15 pm / ng/mL and a detection limit of ~290 pg/mL.

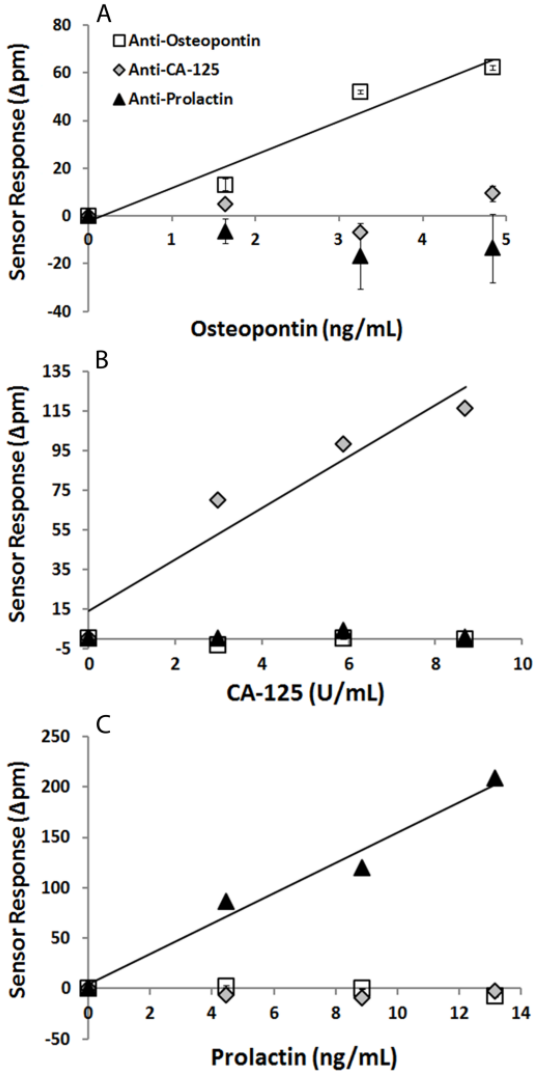

Figure 3.10. Three sphere sizes were functionalized with monoclonal antibodies: anti-OPN (38 μm spheres), anti-CA-125 (53 μm spheres), and anti-prolactin (63 μm spheres). The spheres were combined, immersed in PBS and systematically exposed to each antigen to probe for cross-reactivity. Only sphere sizes functionalized with the antibody compliment to the injected antigen showed a linear response: (A) OPN (R^2 = 0.94) had a sensitivity of 14 pm / ng/mL and detection limit of ~270 pg/mL, (B) CA-125 (R^2 = 0.91) had a sensitivity of 13 pm / U/mL and detection limit of ~0.11 U/mL, and (C) prolactin (R^2 = 0.97) showed a sensitivity of 15 pm / ng/mL and detection limit of ~290 pg/mL. Spheres functionalized with non-complimentary antibodies showed negligible responses indicating cross-reactivity was not significant. Error bars represent intra assay variability (N = 3). In most cases, bars are less than the marker size (see experimental section).

Having established no substantial cross reactivity, all three proteins were quantified in a single PBS assay. Sequential injections of a PBS solution containing all three antigens resulted in the measured linear responses shown in **Fig. 3.11**. In this particular assay, the response for OPN has a sensitivity of 7.7 pm / ng/mL and a detection limit of ~140 pg/mL; CA-125 has a sensitivity of 18 pm / U/mL and a detection limit of ~0.23 U/mL; and prolactin shows a sensitivity of 7.2 pm / ng/mL and a detection limit of ~94 pg/mL.

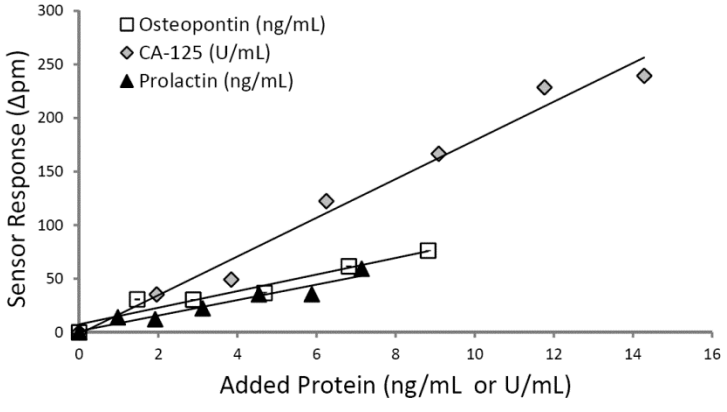

Figure 3.11. Detection of multiple ovarian cancer biomarkers in a single assay in PBS. OPN (38 μm sphere) showed a liner response (R^2 = 0.93) with a measured sensitivity of 7.7 pm / ng/mL and detection limit of ~140 pg/mL. CA-125 (53 μm sphere) showed a measured linear response (R^2 = 0.98) with a sensitivity of 18 pm / U/mL and detection limit of ~0.23 U/mL. Prolactin (63 μm sphere) had a linear response (R^2 = 0.93) with a sensitivity of 7.2 pm / ng/mL and a detection limit of ~94 pg/mL. Error bars represent intra assay variability (N = 3). In most cases, bars are less than the marker size (see experimental section).

A new set of spheres are utilized for each assay, thus inter assay variability may arise from slight differences in microresonator Q-factors. Quality factors can be impacted by several factors including geometry, material absorption, radiative losses, and scattering losses due to imperfections on the sphere surface.[22] Importantly, all measured detection limits are well below the reported antigen serum levels found in both healthy and disease patients.[14, 15, 17, 19]

These results show that all three antigens can be quantified in a single assay, which is important for the development of specific and sensitive screens for ovarian cancer. Moreover, encoding analyte identity into sphere size, as shown in **Fig. 3.11**, or through sphere location (not shown) provides straightforward routes for expanding the number of analytes detected. Furthermore, since the spheres are functionalized before loading into the assay, the choice of targets is flexible as the chemistry is easily implemented.

We aim to further improve the WGM imaging platform by expanding the utility of the assay for the detection of various target molecules. Since the label-free platform provides flexibility in detection of a variety of targets, we were interested in extending WGM imaging to the quantification of nucleic acid markers of ovarian cancer. As discussed in Chapter 1, miRNAs are promising biomarkers for disease detection due to their stability and diagnostic correlations.[23-25] Ultimately, by incorporating various types of markers, the specificity and sensitivity of the early detection method can be greatly improved.

3.3.4 WGM Imaging for the Detection of MicroRNA

MicroRNA are small, noncoding RNAs typically 19 to 25 nucleotides long which have been determined to be important regulators of gene expression.[24] Levels of miRNA have been implicated to play an important role in a number of diseases, including cancer.[23, 26-28] Importantly, numerous miRNA signatures have been identified in serum samples of ovarian cancer patients, providing a non-invasive and powerful tool for diagnostics.[25, 29, 30]

Although there is much interest in detecting nucleic acid markers for disease diagnostics, difficulties associated with quantifying circulating miRNA in bodily fluids prevents wide spread clinical use. Analytical challenges exist due to the short length and low abundance of miRNA markers in physiologic fluids.[31-33] Most often, amplification-based methods such as polymerase chain reaction (PCR) are used due to the high degree of specificity of these well-established techniques. However, the high costs and limited throughput associated with PCR limits its applicability in early disease diagnostics.[31, 32]

To improve throughput, hybridization-based microarrays are emerging as powerful multiplexed detection schemes for diagnostics. These platforms can detect numerous miRNA markers per assay, yet,

they lack accurate quantification.[31] An ideal detection method would provide both quantitative and multiplexed detection capabilities. By utilizing our WGM imaging approach, multiplexed, sensitive and label-free detection of miRNA markers can be achieved. These label-free sensors provide a hybridization-based method for miRNA detection in clinically relevant samples. **Figure 3.12** illustrates the approach for label-free WGM platform for the detection of nucleic acids. Complimentary single stranded RNA molecules are attached to the microsphere surface as capture probes. Prior to hybridization, the WGM resonant wavelength is determined through fluorescence imaging (**Fig. 3.12A**). When the sample is introduced to the microsphere resonator, hybridization between the capture and target strands alter the resonant condition (**Fig. 3.12B**). Using the tunable light source, the new resonant wavelength is determined, providing a quantitative measurement of target miRNA strands in solution (**Fig 3.12C**).

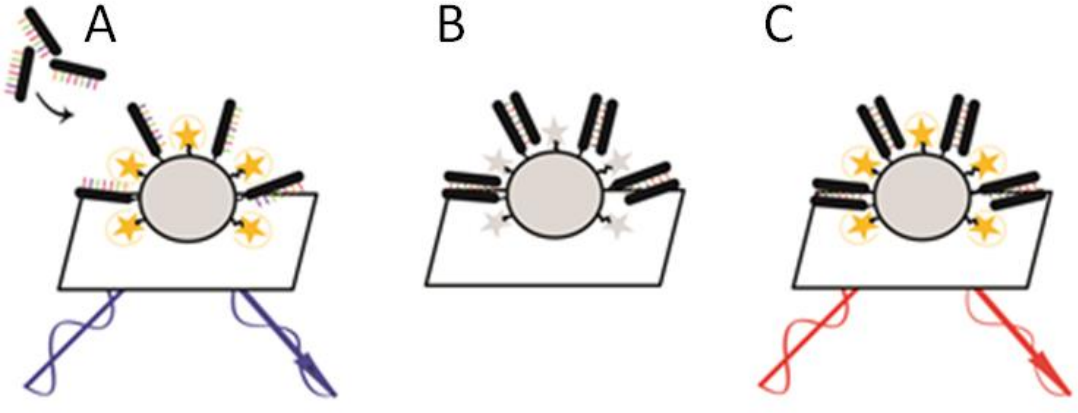

Figure 3.12. Schematic of WGM imaging for the detection of miRNA. (A) Single stranded complimentary RNA sequences are attached to the microsphere surface, and the corresponding WGM resonance is measured through fluorescence imaging. (B) Hybridization of the target and capture strands increases the effective refractive index altering the resonant wavelength. (C) The tunable light source is used to determine the resonant wavelength post hybridization, providing a quantitative measurement of target miRNA in solution.

Initial studies were conducted to determine the feasibility of WGM imaging for detection of miRNA. In order to detect the extremely short nucleic acid strands, 23 nucleotides in length, a modified thermo cycling procedure was implemented to increase hybridization between the target and probe molecules. Heat cycles were used to promote denaturing and annealing of the RNA strands. Initial heating (>T_m) disrupted hydrogen bonds in order to ensure single stranded molecules. Once denatured, assay temperature was cooled (50-60 °C) to promote hybridization between the capture probe and target miRNA.

Initial results using the thermo cycling procedure, detected nM concentrations of miR-142-3p by WGM imaging, shown in **Fig. 3.13**. In a PBS assay, additions of miRNA miR-142-3p, 0 to 23 nM, were made and small resonant wavelength shifts were measured in response to hybridization events. The resonant wavelength shifts responded linearly to increasing miRNA concentration.

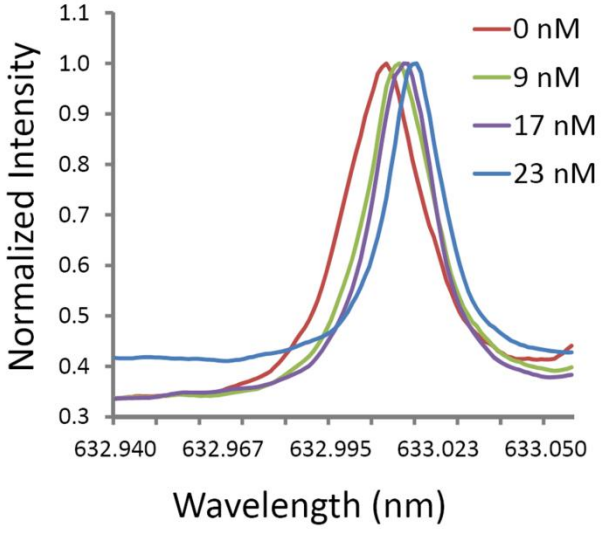

Figure 3.13. Plot of WGM resonator wavelength shifts due to miRNA concentration. Microsphere resonators were functionalized with complimentary single strands through streptavidin-biotin chemistry. WGM imaging was used to measure the resonant wavelength as injections of miRNA standard solutions were made. Hybridization between the target and capture probe resulted in a shift of the WGM resonant wavelength.

The corresponding calibration curve, **Figure 3.14** shows the resulting spectral shifts due to hybridization as a function of miRNA concentration. The linear (R^2 = 0.96) calibration plot had a measured sensitivity of ~0.31 pm/nM miR-142-3p, demonstrating initial proof-of-concept results for miRNA detection using WGM imaging.

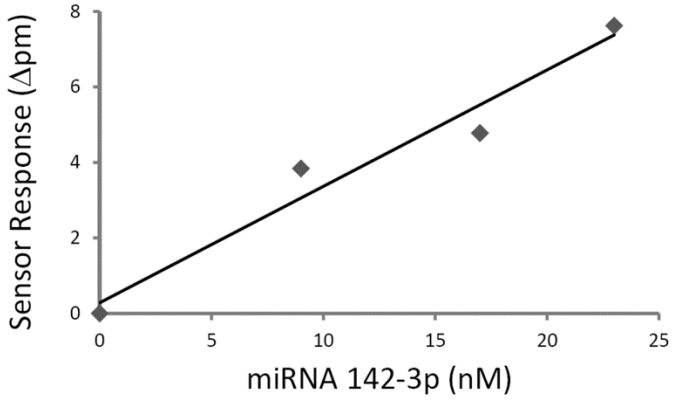

Figure 3.14. Calibration of resonant wavelength shifts as a function of miRNA concentration. With increasing miRNA concentrations, a corresponding red-shift was measured with a linear correlation of R^2 = 0.96 and sensitivity of ~0.31 pm/nM.

Future investigations will focus on detecting miRNA in complicated sample matrices, such as human serum, in order to validate the assay is appropriate for clinical diagnostic applications. WGM imaging provides an improved analytical tool for the multiplexed, quantitative analysis of miRNA. Ultimately, we aim to achieve simultaneous detection of miRNA and proteins in human serum. This achievement will greatly benefit the clinical community by providing a much improved screening method for ovarian cancer.

3.4 Future Directions

3.4.1 Imaging Whispering Gallery Mode Structure

In addition to the previously discussed advantages, fluorescence imaging of WGM resonances provides a route for investigating fundamental parameters of whispering gallery modes. With increased signal-to-noise from the enhanced phase matching, mode structure present in the resonators is visible using the fluorescence imaging approach. **Fig. 3.15** shows a typical fluorescence image from a resonator in which the band of fluorescence arising from the WGM has a distinct structure.

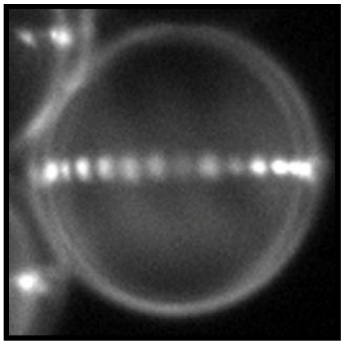

Figure 3.15. Fluorescence image of a single resonator (53 μm) excited at a WGM resonance. The structure observed in the fluorescence ring around the sphere reflects the mode structure of the WGM resonance.

By solving the Helmholtz equation in spherical coordinates, the optical modes of a spherical dielectric can be calculated and are characterized by the radial (n), polar (l) and azimuthal (m) mode numbers.[34] The field distributions can be calculated for various combinations of mode numbers by matching solutions at the dielectric boundary. The radial mode number n indexes field maxima along the sphere radius while l and m are related to the number of angular maxima in the field. Since the fluorescence intensity shown in **Fig. 3.15** maps the field strength at the sphere surface, imaging measurements can characterize the angular components.

The value $l - m + 1$ gives the number of field maxima in the polar direction, perpendicular to the fluorescence ring shown in Fig. 3.4.[35] From **Fig. 3.15** and similar measurements, one maximum is

observed within our spatial resolution suggesting that $l = m$. The value $2l$ reflects the number of maxima around the equator of the resonator which, for the resonator shown in **Fig. 3.15**, is 28. Therefore, assuming that the fundamental radial mode is excited ($n = 1$), the mode numbers for the resonance shown in **Fig. 3.15** correspond to $n = 1$, $m = l = 14$. These measurements, therefore, provide a direct link with the underlying mode structure of the light trapped within a resonator and may also lead to new ways of analyte sensing based on mode structure.

Often complicated mode structures are observed by fluorescent imaging of WGM. Initial investigations reveal mode structure changes as a result of alterations of solution refractive index, shown in **Fig. 3.16**. These characteristic alterations provide promising approaches for label-free sensing which our group is currently investigating.

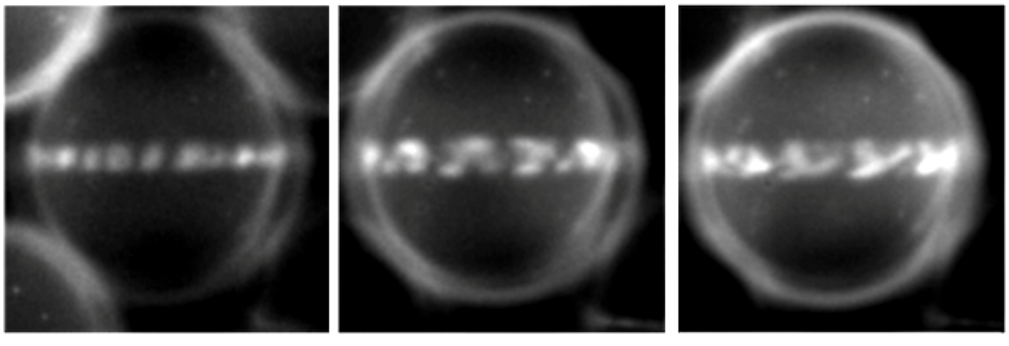

Figure 3.16. Fluorescence imaging reveals WGM mode structure. A particular microsphere is shown in different refractive index solutions. Noticeably, the mode structure changes in response to solution refractive index. Mode structure imaging provides a potential new sensing scheme which we are currently investigating.

3.4.2 Challenges of Fluorescence Imaging of Whispering Gallery Mode Resonances

Using fluorescence detection to determine WGM location and intensity provides several sensing advantages. However, the addition of dye to the surface of microsphere resonators may affect the performance metrics. Attached dye as a fluorescent marker on the microsphere surface results in a reduction of the Q-factor due to absorption losses. Typical Q-factors achieved are 10^4-10^5 which are

comparable to those measured in microfabricated resonators.[36, 37] However, microsphere resonators have been reported to have Q-factors orders of magnitude larger, 10^8-10^9.[22, 38] To improve the performance metrics of WGM imaging, we have investigated modified detection schemes. Chapter 4 discusses measuring WGM resonance using evanescently scattered light from the resonator.[39]

3.5 Conclusions

A label-free sensing method based on fluorescence imaging of microsphere whispering gallery modes is presented. An evanescent field is created at the sample interface using total internal reflection in a Dove prism which enables large fields of microsphere resonators to be simultaneously excited. Whispering gallery mode resonances are measured by scanning the excitation wavelength and imaging the enhanced ring of fluorescence from individual microspheres as light efficiently couples into the dye functionalized resonators. This label-free approach is capable of detecting proteins, nucleic acids and other species in a homogeneous format.

Combining fluorescence detection with high-Q microsphere resonators offers many advantages for biosensing. WGM imaging measures an intrinsic property, namely the excitation spectrum, which reduces difficulties associated with photobleaching and variable dye labeling which can be problematic for intensity based fluorescence assays. Moreover, fluorescence imaging provides a tool for visualizing mode structure linking simulations of the trapped modes to experimental measurements which may be useful for developing new sensing schemes.

We demonstrate the large multiplexing potential of this fluorescence approach by imaging over 120 microsphere resonators in an area less than 1 mm^2. Additionally, by encoding analyte identity with sphere size we demonstrate the ability to simultaneously detect the putative ovarian cancer markers osteopontin, CA-125, and prolactin in a single assay. Since sphere functionalization takes place before loading onto the assay, the biosensing platform greatly simplifies assay development, especially for multiplexed formats. These results illustrate the utility of WGM imaging to quantify biomarkers in complex biological media.

3.6 References

1. Huckabay, H. A.; Dunn, R. C., Whispering Gallery Mode Imaging for the Multiplexed Detection of Biomarkers. *Sens. Actuators, B* **2011,** *160* (1), 1262-1267.
2. Gorodetsky, M. L.; Ilchenko, V. S., High-Q Optical Whispering-Gallery Microresonators: Precession Approach for Spherical Mode Analysis and Emission Patterns with Prism Couplers. *Opt. Commun.* **1994,** *113*, 133-143.
3. Gorodetsky, M. L.; Ilchenko, V. S., Optical Microsphere Resonators: Optimal Coupling to High-Q Whispering-Gallery Modes. *J. Opt. Soc. Am. B* **1999,** *16* (1), 147-154.
4. Rowland, D. R.; Love, J. D., Evanexcent Wave Coupling of Whispering Gallery Modes of a Dielectric Cylinder. *Proc. Inst. Elect. Eng., Optoelectronics,* **1993,** *140* (3), 177-188.
5. Li, C. C., et al., Efficient Hydroxylation of BaTiO(3) Nanoparticles by Using Hydrogen Peroxide. *Colloids Surf., A* **2010,** *361* (1-3), 143-149.
6. Zhu, H. Y., et al., Rapid and Label-Free Detection of Breast Cancer Biomarker CA15-3 in Clinical Human Serum Samples with Optofluidic Ring Resonator Sensors. *Anal. Chem.* **2009,** *81* (24), 9858-9865.
7. Nossov, V., et al., The Early Detection of Ovarian Cancer: from Traditional Methods to Proteomics. Can we Really do better than Serum CA-125? *Am. J. Obstet. Gynecol.* **2008,** *199* (3), 215-223.
8. Yurkovetsky, Z., et al., Development of a Multimarker Assay for Early Detection of Ovarian Cancer. *J Clin Oncol* **2010,** *28*, 2159-2166.
9. Woolas, R. P., et al., Combinations of Multiple Serum Markers Are Superior to Individual Assays for Discriminating Malignant from Benign Pelvic Masses. *Gynecol. Oncol.* **1995,** *59* (1), 111-116.
10. Suh, K. S., et al., Ovarian Cancer Biomarkers for Molecular Biosensors and Translational Medicine. *Expert Rev. Mol. Diagn.* **2010,** *10* (8), 1069-1083.
11. Badgwell, D.; Bast, R. C., Early Detection of Ovarian Cancer. *Dis. Markers* **2007,** *23* (5-6), 397-410.
12. Mor, G., et al., Serum Protein Markers for Early Detection of Ovarian Cancer. *Proc. Natl. Acad. Sci. U. S. A.* **2005,** *102* (21), 7677-7682.
13. Brakora, K. A., et al., Utility of Osteopontin as a Biomarker in Recurrent Epithelial Ovarian Cancer. *Gynecol. Oncol.* **2004,** *93*, 361-365.
14. Kim, J. H., et al., Osteopontin as a Potential Diagnostic Marker for Ovarian Cancer. *Women's Oncol. Rev.* **2002,** *2*, 313-314.

15. Nakae, M., et al., Preoperative Plasma Osteopontin Level as a Biomarker Complementary to Carbohydrate Antigen 125 in Predicting Ovarian Cancer. *J. Obstet. Gynaecol. Res.* **2006,** *32*, 309-314.
16. Bast, R. C., Jr., et al., CA-125: the Past and the Future. *Int. J. Biol. Markers* **1998,** *13* (4), 179-187.
17. Hwang, J., et al., Correlation Between Preoperative Serum Levels of Five Biomarkers and Relationships Between these Biomarkers and Cancer Stage in Epithelial Ovarian Cancer. *J. Gynecol. Oncol.* **2009,** *20* (3), 169-175.
18. Jacobs, I. J.; Menon, U., Progress and Challenges in Screening for Early Detection of Ovarian Cancer. *Mol. Cell. Proteomics* **2004,** *3* (4), 355-366.
19. Levina, V. V., et al., Biological Significance of Prolactin in Gynecologic Cancers. *Cancer Res.* **2009,** *69* (12), 5226-5233.
20. Buchen, L., Cancer: Missing the Mark. *Nature* **2011,** *471* (7339), 428-432.
21. Clarke-Pearson, D. L., Clinical Practice. Screening for Ovarian Cancer. *N Engl J Med* **2009,** *361* (2), 170-177.
22. Gorodetsky, M. L., et al., Ultimate Q of Optical Microsphere Resonators. *Opt. Lett.* **1996,** *21* (7), 453-455.
23. Calin, G. A.; Croce, C. M., MicroRNA Signatures in Human Cancers. *Nat. Rev. Cancer* **2006,** *6* (11), 857-866.
24. Ferracin, M., et al., Micromarkers: miRNAs in Cancer Diagnosis and Prognosis. *Expert Rev. Mol. Diagn.* **2010,** *10*, 297-308.
25. Iorio, M. V., et al., MicroRNA Signatures in Human Ovarian Cancer. *Cancer Res.* **2007,** *67* (18), 8699-8707.
26. Gilad, S., et al., Serum MicroRNAs Are Promising Novel Biomarkers. *Plos One* **2008,** *3* (9), -.
27. Lu, J., et al., MicroRNA Expression Profiles Classify Human Cancers. *Nature* **2005,** *435* (7043), 834-838.
28. Wittmann, J.; Jäck, H.-M., Serum microRNAs as Powerful Cancer Biomarkers. *Biochimica et Biophysica Acta In Press*.
29. Resnick, K. E., et al., The Detection of Differentially Expressed microRNAs From the Serum of Ovarian Cancer Patients Using a Novel Real-Time PCR Platform. *Gynecol. Oncol.* **2009,** *112*, 55-59.
30. Taylor, D. D.; Gercel-Taylor, C., MicroRNA Signatures of Tumor-Derived Exosomes as Diagnostic Biomarkers of Ovarian Cancer. *Gynecol. Oncol.* **2008,** *110* (1), 13-21.
31. Chevillet, J. R., et al., Issues and Prospects of microRNA-Based Biomarkers in Blood and Other Body Fluids. *Molecules* **2014,** *19* (5), 6080-6105, 26 pp.

32. Tiberio, P., et al., Challenges in Using Circulating miRNAs as Cancer Biomarkers. *Biomed Res Int* **2015,** *2015*, 731479.
33. McDonald, J. S., et al., Analysis of Circulating microRNA: Preanalytical and Analytical Challenges. *Clin. Chem.* **2011,** *57*, 833-840.
34. Oraevsky, A. N., Whispering-Gallery Waves. *Quantum Electronics* **2002,** *32* (5), 377-400.
35. Little, B. E., et al., Analytic Theory of Coupling from Tapered Fibers and Half-Blocks into Microsphere Resonators. *Lightwave Technology, Journal of* **1999,** *17* (4), 704-715.
36. Chiasera, A., et al., Spherical Whispering-Gallery-Mode Microresonators. *Laser Photonics Rev.* **2010,** *4* (3), 457-482.
37. Fan, X., et al., Overview of Novel Integrated Optical Ring Resonator Bio/Chemical Sensors. **2007,** *6452*.
38. Vernooy, D. W., et al., High-Q Measurements of Fused-Silica Microspheres in the Near Infrared. *Opt Lett* **1998,** *23*, 247-249.
39. Arnold, S., Microspheres, Photonic Atoms and the Physics of Nothing. *American Scientist* **2001,** *89* (5), 414-421.

Chapter 4

Investigation of Whispering Gallery Mode Resonators as Rapid, Label-Free Sensors in Small Volume Systems

Portions of this chapter were published in Biosensors:
Wildgen, S.; Dunn, R. Whispering Gallery Mode Resonators for Rapid Label-Free Biosensing in Small Volume Droplets. Biosensors. 2015, 5 (1), 118-130.

4.1 Introduction

The specific detection of biological markers in complex matrices is important in early disease detection, evaluating response to treatment, and monitoring disease reoccurrence. To reduce the complexity, costs, and time associated with these tests, much work has been devoted to developing biosensing methods that can specifically quantify analytes of interest in small volumes of biological fluids. Whispering gallery mode (WGM) resonators are desirable biosensing platforms not only for their label-free detection capabilities, but also due to their small, compact structure. By incorporating hundreds of WGM resonators within 10 μL droplets, microspheres provide a means of rapid, low cost and high-content analysis within sample limited assays. Furthermore, the high sensitivity of these tiny structures achieves impressive detection capabilities which can be applied to a variety of analytical platforms. In this chapter, we demonstrate the flexibility and utility of WGM detectors in small volume droplets by measuring real-time protein binding events.

4.1.1 Utilizing Whispering Gallery Mode Resonators in Small Volume Platforms

Small volume systems are appealing for their reduced sample requirements, minimal reagents, rapid analysis and compatibility with high throughput technologies. One of the main challenges of working with small volumes is accurate and reliable fluid handling. Microfluidic systems have progressed significantly over the last several decades to address these needs. Most microfluidic systems rely on continuous flow, however, these systems are not easily compatible with physiological fluids, which are vital for clinical diagnostics.[1] Recently, electrowetting digital microfluidic systems have gained attention due to their ability to control small fluid volumes, including physiological fluids, through the automation of droplet mixing, splitting, dispensing and transporting.[2, 3] In these systems, discrete droplets are manipulated by applying electrical fields to an array of patterned electrodes.[4]

Unlike traditional continuous flow microfluidic systems, digital microfluidics allows for complete control of individual, small volume droplets. Another member of our group, Daniel Kim, has fabricated a low cost digital microfluidic platform based on previously reported procedures which use a glass microscope slide, plastic wrap, and Rain X to create a one-plate system, **Fig. 4.1**.[5] The resulting one-plate system design supports small volume droplets in air on a hydrophobic surface.

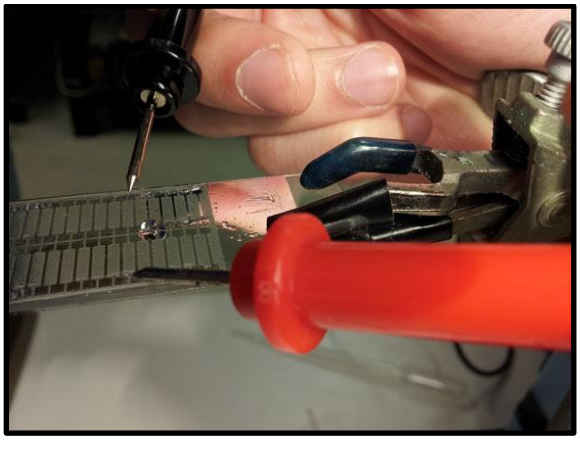

Figure 4.1. One-plate digital microfluidic platform for the manipulation and automation of droplets-in-air.[5] Patterned electrodes on the glass surface allow for precise control of droplet location. The device was fabricated by Daniel Kim. (Unpublished work)

These small volume systems are advantageous for the manipulation of droplets and precise fluid handling. To date, majority of detection schemes require off-chip analysis through coupling of the digital microfluidic platform to commercial instrumentation, such as mass spectrometry. These requirements significantly hinder the portability and usefulness of these miniaturized analytical systems while ultimately increasing costs and requirements. By incorporating an on-chip detection scheme for digital microfluidic platforms, a low-cost, portable, and high-throughput analytical tool is possible.

Majority of on-chip analysis methods currently available for digital microfluidic platforms require label-based detection methods relying on chemiluminescent[3], colorimetric[1], or fluorescent[6, 7] signals. Label-free approaches capable of multiplexed detection are particularly attractive for these platforms since they simplify the chemistry, enable real-time analysis, and allow multiple targets to be evaluated.[8-11] We are interested in utilizing WGM resonators in small volume droplets in order to assess the usefulness of these detectors for digital microfluidic platforms. As shown above in **Fig. 4.1**, a one-sided digital microfluidic chip consist of a droplet in air supported by a hydrophobic surface. In this chapter, we investigate the usefulness of WGM resonators as label-free detectors within these systems. The small size of the resonators allows for hundreds to be easily incorporated within a droplet, and, furthermore, there are several sensing performance metrics which are improved by using a detector which is micrometers in size.

4.1.2 Advantages of Whispering Gallery Mode Resonators as Detectors in Small Volume Systems

Historically, the primary metric driving sensor development has been detection limits. This has led to the advancement of many cleaver biosensing schemes, which enable detection down to the single molecule level. Often this is accomplished using nanoengineered sensors where the small size of the sensing element leads to favorable signal-to-noise.[12-14] Recently, however, an increasing appreciation for

the time required to carry out an analysis, especially at low concentrations, has focused a renewed interest in mass transport aspects of biosensing.[15-17]

For species at low concentration, diffusion to the sensing element often represents a limiting factor in the time required to carry out analysis. Analyte diffusion can lead to surprisingly long mass transport times in unstirred solutions.[15-17] For sensing, these issues can be further exaggerated by the size and geometry of the detection element itself. While nanometric sensors offer many unique advantages for sensing, their small size limits diffusion to the active area. At low picomolar analyte concentrations, for example, diffusion to nanoscale elements on a planar surface can take days, leading to impractically long analysis times.[15-17] Moving to larger WGM microsphere resonators for sensing can decrease analysis time through favorable mass transport metrics. Their spherical geometry and tens of microns diameters lend themselves to optimized mass transfer for rapid analysis.[15-17]

The compact size of microsphere resonators also enables accurate analysis in small volumes, supporting multiplexed sensing in sample-limited applications. For the latter, small droplet analysis platforms, such as digital microfluidic systems, offer an intriguing approach for reducing the costs, complexity and consumables associated with analysis.[18-20] Droplets on a surface undergo complex evaporation processes leading to temperature gradients which produce a natural mixing effect within the liquid.[21-25] This can potentially decrease sensor response time through improved mass transport.

In this chapter, we investigate the response time of WGM resonators in small droplet assays. As a model system, 38 μm diameter barium titanate resonators are functionalized with bovine serum albumin-biotin to detect binding of streptavidin. WGM resonators are loaded into 10 μL droplets of phosphate buffered saline supported on a hydrophobic Teflon AF film. Shifts of unmodified WGM resonators were observed over time to quantify evaporation of the droplets and define the useful limits over which assays can be performed without significant perturbation due to decreasing volume. Sensor response is compared in both stirred and unstirred droplets with the results showing that active stirring is required to sufficiently shorten response time in order to compete with evaporation. Initial binding rate studies in actively stirred droplets show that nanomolar protein concentrations can be quantified within minutes

using the small volume assay. Results presented here indicate the potential of utilizing WGM resonators in small volume droplet systems, including digital microfluidic platforms.

4.2 Materials and Methods

4.2.1 Materials

Barium titanate microspheres were obtained from Mo-Sci Corporation (Rolla, MO). Polydimethylsiloxane (PDMS) or Slygard 184 Silicone Elastomer Kit was obtained from Dow Corning (Midland, MI). Optical coating AngstromLink AL-2233 (1% solids) was obtained from Fiber Optic Center (New Bedford, MA). Rain X was obtained from the local hardware store. Teflon® AF amorphous fluoropolymer (1% solids) was obtained from DuPont (Wilmington, DE). Sigmacote and poly-l-lysine (0.1% w/v in water) were obtained from Sigma-Aldrich (St Louis, MO). Streptavidin and 10x phosphate buffered saline (PBS) (27 mM KCl; 15 mM KH_2PO_4; 1400 mM NaCl; 81 mM Na_2HPO_4) were obtained from MP Biomedicals. Prior to use, 1x PBS solutions were prepared with 0.05% sodium azide (pH 7.35). Bovine serum albumin-biotin (BSA-biotin) and SuperBlock® (PBS) Blocking Buffer were acquired from Thermo Scientific (Waltham, MA). OptEIA IL-10 and IL-6 Human ELISA kits II were purchased from BD Biosciences (San Jose, CA). Unless otherwise noted, all other materials and reagents were obtained from Fisher Scientific (Hampton, NH) and used without further purification.

4.2.2 Experimental Set-Up and Measurements

A hydrophobic glass slide supporting a PBS droplet is placed on a Dove prism coated with high index immersion oil. Excitation light from a tunable diode laser (New Focus Vortex II TLB-6900) centered at wavelength 633 nm is coupled into the prism. The Dove prism refracts the light towards the sample at an angle leading to total internal reflection at the interface. The associated evanescent field is used to excite whispering gallery modes in the barium titanate microspheres.

To measure WGM spectra, the evanescently scattered light from the resonator is collected from below using an inverted optical microscope (Zeiss Axiovert 100 TV) equipped with a 4x objective (Olympus PlanN, 0.10 NA). The scattered light is detected on an avalanche photodiode (APD) (SPCM-200, EG&G). Digital Instruments Nanoscope IIIa software was used to control the acquisition system by synchronizing the wavelength scanning of the laser and data collection to continuously record spectra with time. All experiments were carried out at 21 °C ± 1 °C and relative humidities between 10% and 18%.

4.2.3 Preparing Hydrophobic Surfaces

Glass microscope slides were modified in order to support aqueous droplets in air. Various surfaces were investigated in order to produce stable and reproducible hydrophobic films. For initial investigationes, Teflon tape with small circular cut outs (~1 mm) was placed on a clean microscope slide. Pressure and heat were applied to the tape to help it firmly adhere to the glass. Aqueous solution was pipetted into the cut outs and the hydrophobic boundaries of the Teflon tape supported droplet formation (**Fig. 4.2B**).

Figure 4.2. Images of Teflon tape on a glass microscope slide to support aqueous droplet formation in air. (A) The Teflon tape was firmly adhered to the microscope slide using heat and pressure. (B) A side view shows the formation of aqueous droplets (~10 μL) on the surface due to the hydrophobic boundary created by the Teflon tape.

Alternatively, hydrophobic surfaces were created by coating glass microscope slides. Various hydrophobic coatings were investigated including Teflon AF amorphous fluoropolymer (400s2-100-1), AL1-2233 (n=1.333), Rain X, and PDMS. To create hydrophobic surfaces using Teflon AF, AL1-2233 and Rain X, separate glass slides were spin coated with ~1.5 μL of solution to create a thin hydrophobic layer. Slides were spin cast at approximately 10,000 rpm for ~15 seconds. Coated slides were placed in a 60 °C oven for 15 minutes to remove residual solvent and stored at room temperature prior to use.

PDMS surfaces were prepared by mixing elastomer resin with curing agent (10:1 w/w), removing air bubbles in a vacuum, then heating to 60 °C for polymerization. No further modifications to the PDMS surface were made. 10 μL sessile droplets were deposited onto the hydrophobic surfaces and contact angles were measured to determine the degree of hydrophobicity.

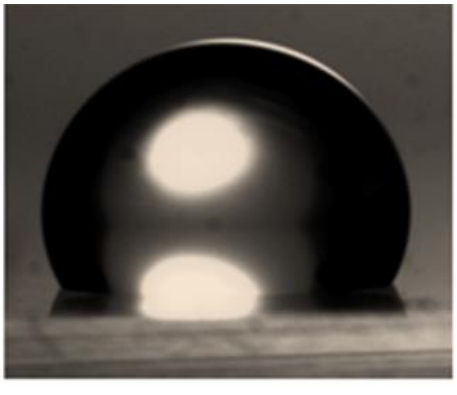

Figure 4.3. A 10 μL aqueous droplet supported on a Teflon AF hydrophobic surface. To prepare the slide, Teflon AF was spin coated onto the surface then dried to remove residual solvent. Contact angle measurements were completed to determine the degree of hydrophobicity.

4.2.4 Evanescently Scattered Light for WGM Imaging

Scatter detection can be used as a low cost, easily implemented WGM detection scheme. A well-defined spot of scattered radiation exists due to the large size of the resonator compared with the rapid

decay of the evanescent field.[26-28] This provides a label-free readout signal of WGM resonance that is easily collected and imaged. Furthermore, by eliminating the fluorescent dye marker, we reduce associated equipment requirements, costs, and time constraints for WGM imaging. By detecting the microsphere scatter intensity, we aim to further simplify WGM imaging and increase flexibility of the platform for biosensing. Results presented in this chapter were collected using evanescently scattered light from WGM resonators.

4.2.5 Refractive Index Assays

For refractive index measurements, the appropriate amount of 18 MΩcm water (10 or 100 μL) was pipetted onto unfunctionalized barium titanate microspheres resting on Teflon AF hydrophobic glass slides. Appropriate volumes (1 μL or 10 μL) of 1.7 M NaCl stock solution were quickly pipetted into the droplet to increase the refractive index by 0.002 refractive index units (RIU). For experiments involving mixing droplets, a stirring system was made by using a single mode optical fiber (125 μm diameter) attached to a 12 V motor for rotation. The glass fiber was positioned in the droplet prior to the NaCl spikes and rotated at ~5,000 rpm.

4.2.6 Microsphere Functionalization

Barium titanate microspheres of 38 μm diameters were used for WGM assays. Various microsphere functionalization procedures resulting in non-covalent or covalent attachment of BSA-biotin were investigated in order to optimize biosensor performance.

For incubation using small volumes, spotting procedures were used to investigate the immobilization procedures of BSA-biotin on the surface of microspheres. To incubate, spheres were placed in a PDMS cut out on a glass microscope slide, then submerged in 10-20 μL of solution and sealed in a humidity chamber to reduce evaporation. The sealed chambers were stored at 4 °C. Microspheres were separately incubated in poly-l-lysine (0.1% w/v in water), APTES, or glutaraldehyde (50%) overnight, rinsed with

PBS, and then incubated with BSA-biotin (2 mg/mL) for 2 hours. Functionalized microspheres were stored in PBS at 4 °C.

For covalent attachment of BSA-biotin, microspheres were plasma cleaned and sonicated in H_2O_2 for 15 min. They were then rinsed sequentially in water, ethanol, and toluene before reacted in 10% (3-aminopropyl)triethoxysilane (APTES)/toluene for 2 hours. The microspheres were tumbled in ~2 mL of solution during the following reaction steps. Following silanization, spheres were rinsed in toluene, ethanol, and PBS then further reacted in 10% gluteraldehyde/PBS for 1 hour. Aldehyde functionalized microspheres were reacted with the capture protein, BSA-biotin (2 mg/mL), interleukin-6 (IL-6) or interleukin-10 (IL-10), for 2 hours leading to covalent attachment. To minimize non-specific binding, functionalized microspheres were incubated in SuperBlock blocking buffer solution for 15 minutes. All functionalized microspheres were stored in PBS at 4 °C.

4.2.7 Bioassay Protocol

For all protein assays, functionalized microspheres were placed on a hydrophobic glass slide and 10 μL of PBS was carefully pipetted onto them. 1 μL injections of stock solutions (streptavidin 0-7.6 μM, IL-6 2175 pg/mL, or IL-10 2200 pg/mL) were delivered into the droplet using pipette tips coated with Sigmacote to reduce wetting of the pipette surface.

4.3 Results and Discussion

To take advantage of the compact detector size for real-time binding, WGM resonators were utilized as label-free detectors in small volume systems. For these studies, we prepared small volume droplets on hydrophobic surfaces because they were easy to fabricate, capable of high throughput, and are applicable for small volume systems such as digital microfluidics. Results discuss the development and optimization of the small volume systems and corresponding WGM measurements.

4.3.1 Analysis of Hydrophobic Surfaces

Hydrophobic surfaces are important components of small volume analytical systems such as digital microfluidic platforms. Here we investigate polymer materials and coatings to develop a hydrophobic surface for aqueous droplets. Several methods were investigated for the fabrication of stable and reproducible hydrophobic surfaces. Initially, Teflon tape with small circular cut outs (~1 mm) was adhered to a glass microscope slide. Microsphere resonators were placed in the cut outs and surrounded by aqueous solution which formed a droplet due to the hydrophobic boundary of the Teflon tape (**Fig. 4.2**). This geometry allowed for light to be easily coupled into the microresonators at the glass surface. While promising, poor Teflon tape adhesion to the surface resulted in inconsistent and unstable droplet systems due to solution spreading between the tape and glass surface. This system was determined not to be the most robust or reproducible for small volume investigations.

To develop a more stable system, the hydrophobicity of PDMS surfaces and other polymer coatings were analyzed. PDMS was prepared with elastomer and curing agent (10:1 w/w) spread on a petri dish surface. After polymerization, a section of the PDMS was removed and the hydrophobicity was determined without any further modifications to the silicon surface. The hydrophobic coatings Teflon AF amorphous fluoropolymer (400s2-100-1), AL1-2233 (n=1.333), and Rain X were prepared on glass slides by spin casting. Contact angle (θ) measurements of sessile droplets on each surface were measured in order to determine the degree of hydrophobicity, shown in **Fig. 4.4**. Teflon AF was determined to produce the most hydrophobic surface with an approximate contact angle of 115°.[24] Therefore, Teflon AF coated slides were used for small volume droplet experiments.

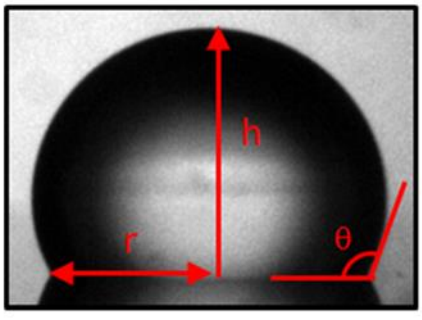

Solution	Contact Angle
Teflon AF	115 ± 3 °
AL 2233	112 ± 3 °
PDMS	103 ± 3 °
Rain X	96 ± 3 °

Figure 4.4. A 10 μL droplet on a Teflon AF hydrophobic surface with the contact angle (θ), height (h) and contact radius (r) parameters indicated in red. Different hydrophobic surfaces were prepared on glass slides and the resulting contact angles were measured to determine the extent of hydrophobicity (N = 3). Teflon AF created the most hydrophobic surfaces with a contact angle of ~115° and was used exclusively for droplet experiments.

4.3.2 Small Volume Droplet Set-Up

The small, compact size of microsphere WGM resonators make them well suited for small volume assays. **Figure 4.5A**, for example, shows approximately 500 resonators (38 μm diameter) loaded into a 10 μL droplet of PBS on a Teflon AF hydrophobic surface. In theory, each resonator in the droplet acts as an individual assay, which enables large signal averaging and/or multiplexing capabilities even in these modest volumes. WGM resonances are excited using the evanescent field created at the substrate interface through total internal reflection of the excitation light at the surface of a Dove prism, as shown in **Fig. 4.5B**. To measure the WGM spectrum, evanescently scattered light from a WGM resonator is collected from below with a 4x objective (Olympus PlanN, 0.10 NA) as the excitation wavelength of the laser is tuned. The scattered light can be imaged onto a CCD camera (Photometrics, CoolSnap K4) for multiple resonator analysis or focused onto a single element detector (APD, SPCM-200, EG&G) for rapid analysis of a single resonator. A micropipette positioned above the droplet is used to quickly inject standards into the droplet. Sensor response in unstirred and stirred droplets is compared. For actively

mixed droplets, a 125 μm diameter optical fiber connected to a 12 V motor in the droplet as shown in **Fig. 4.5C** and rotated at ~5,000 rpm.

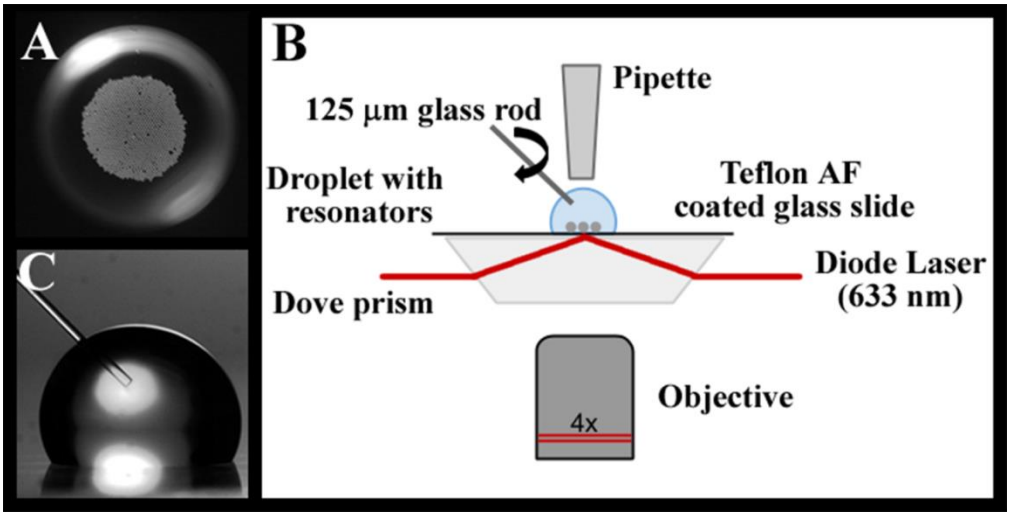

Figure 4.5. (A) Approximately 500 barium titanate (38 μm diameter) microspheres within a 10 μL PBS droplet on a hydrophobic Teflon AF coated glass surface. (B) Schematic of WGM droplet assay. Light from a tunable diode laser is directed into a Dove prism for evanescent wave coupling into 38 μm barium titanate microspheres. Evanescently scattered light from the resonators is imaged from below (4x objective, 0.10 NA) and detected on an avalanche photodiode (APD). (C) For active mixing experiments, a 125 μm diameter optical fiber is rotated at ~5,000 rpm in the 10 μL PBS droplet.

With a system in place, it was important to first characterize droplet evaporation. Aqueous droplets in air were prepared and analyzed using the above set-up to determine the feasibility of utilizing WGM resonators as detectors in small sample volumes.

4.3.3 Droplet Evaporation

Analysis within supported droplets exposed to air is complicated by evaporation. While droplet evaporation can be exploited as a means of concentrating analytes and optimizing detection limits, it more

often hinders analysis by limiting the time available.[29] Evaporation of supported sessile droplets is a complicated process that depends on environmental factors such as relative humidity and temperature, as well as, the nature of the interactions between the droplet and the substrate surface.[30-35]

As others have shown, a high contact angle leads to a linear decrease in droplet volume with time, which can be characterized by measuring the changes in the droplet height.[22, 23, 31] **Figure 4.6A** shows evaporation of a 10 μL PBS droplet on a hydrophobic surface at various time points. Under the conditions tested, a 10 μL droplet on the hydrophobic surface will typically evaporate in 50-60 minutes. In **Fig. 4.6B**, the droplet height is plotted with time to show the expected linear dependence.

Also plotted in **Fig. 4.6B** is the shift in WGM resonance from WGM resonators in an evaporating 10 μL PBS droplet. As the droplet volume decreases due to evaporation, the concentration of ions in the PBS droplet increases. This results in a change of the refractive index of the solution and shifts the WGM resonance. These WGM shifts seem to become evident after approximately 600 seconds. In a control study with 10 μL PBS droplets covered in silicon oil to prevent evaporation, negligible shifts in the WGM resonance were observed on this time scale (**Fig. 4.6B**).

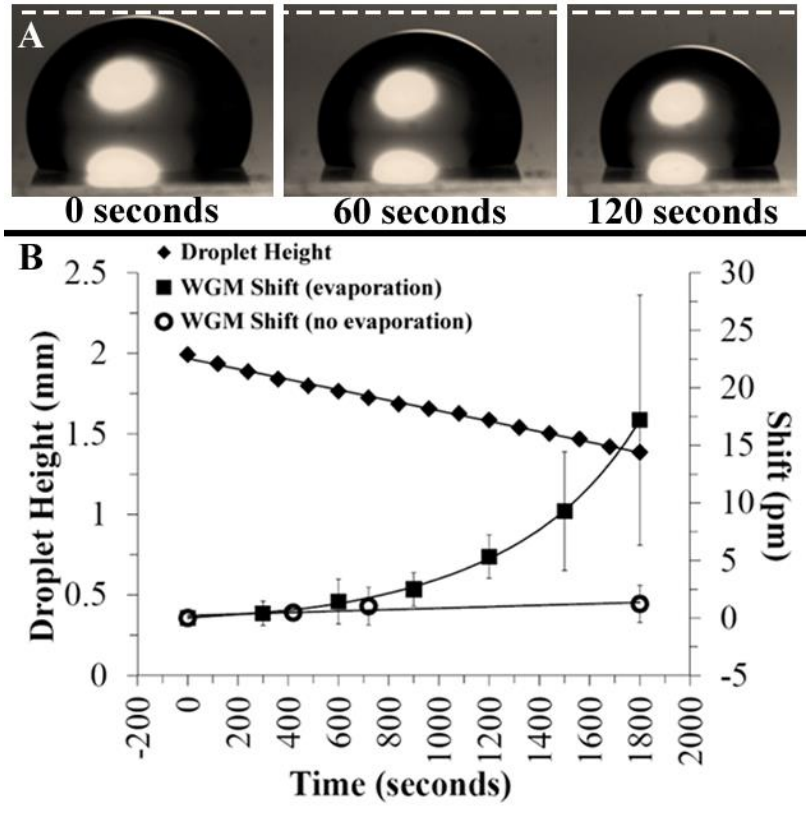

Figure 4.6. (A) Evaporation of a 10 μL PBS droplet over time. The white dotted line indicates the original height of the droplet which is seen to decrease with time. (B) Evaporation of 10 μL PBS droplets on a Teflon AF coated surface (115^{o} contact angle) leads to the expected linear decrease (R^2= 0.997) in droplet height with time (diamonds, N=3). The evaporating 10 μL PBS droplet red-shifts the WGM resonance (squares, N=10) of embedded resonators as the decreasing volume concentrates the buffer ions. As shown, evaporation negligibly affects the WGM resonance ($\leq$ 2 pm shift in first 10 minutes) early in the evaporative process. Control experiments using 10 μL PBS droplets covered in silicon oil (open circles, N=2) shows the stability of the WGM resonance in the absence of evaporation. Error bars represent inter assay variability.

For droplets in air, the refractive index shifts can complicate specific biosensing at the WGM resonator. However, as shown in **Fig. 4.6B**, the shifts are minimal ($\leq$ 2 pm) within the first 10 minutes, thus, providing a window over which WGM bioassays can be carried out with negligible effects from background refractive index changes. The goal here, then, is to explore conditions under which analytes can be quantified in small droplet assays before evaporation significantly affects the WGM resonance or

droplet volume. Measures can be taken to significantly reduce evaporation, such as using oil layers or controlling relative humidity. However, we chose to investigate droplets in air because they provide a straightforward and simple system for initial characterization of real-time analysis using WGM resonators. Once understanding the capabilities of resonators in these simplified small volume systems, more elaborate schemes can be investigated.

4.3.4 Real-Time Analysis of WGM Resonators

To minimize the effects of evaporation, initial binding rate measurements are used to quantify protein concentration. These measurements are rapid since they do not require the establishment of equilibrium and offer additional advantages for microsphere WGM assays, where resonator Q-factor and other metrics difficult to control can lead to variations in resonator sensitivity. First, however, WGM resonator real-time response in small volume droplets must be characterized and optimized. To characterize sensor response, spectra are continuously recorded with time as shown in **Fig. 4.7**. The waterfall plot in **Fig. 4.7A** shows the response from a 38 μm resonator in a 100 μL droplet of water following a rapid injection of salt solution to elevate the refractive index. **Figure 4.7B** highlights selected line cuts from the waterfall plot showing the evolution in the WGM spectra with time. The WGM resonance has a measured Q-factor of 3.0×10^4.

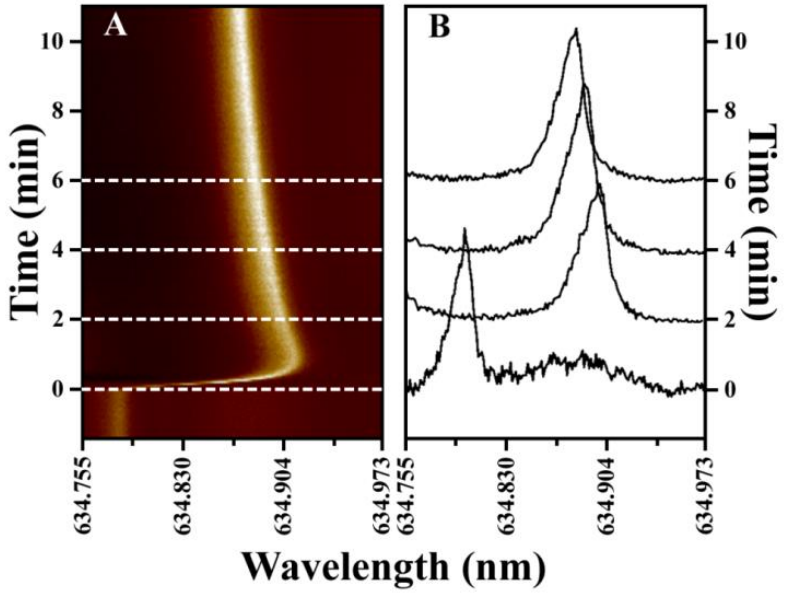

Figure 4.7. (A) Waterfall plot showing the time evolution in the WGM resonance of a 38 μm diameter barium titanate resonator in a 100 μL water droplet. At time zero, a 10 μL spike of saline solution (ΔRIU = +0.002) is quickly injected into the droplet, elevating the refractive index and red-shifting the WGM resonance. The WGM resonance relaxes towards a new equilibrium position as convective mixing in the sessile droplet equilibrates the solution. (B) Selective line cuts from the waterfall plot show the time evolution in the WGM resonance following saline injection. The measured Q-factor is 3.0×10^4.

To characterize resonator response in small sessile droplets, **Fig. 4.8** compares representative WGM shifts with time for two different droplet volumes. **Figures 4.8A** and **B** compare the response of the same WGM resonator in a 100 μL and a 10 μL droplet, respectively, upon injection of salt solution to increase droplet refractive index by 0.002 RIU. Both time traces show an initial maximum shift in the WGM resonance as the injected high index solution interacts with the resonator. These shifts relax towards an equilibrium value as convective currents in the sessile droplets mix the solution.

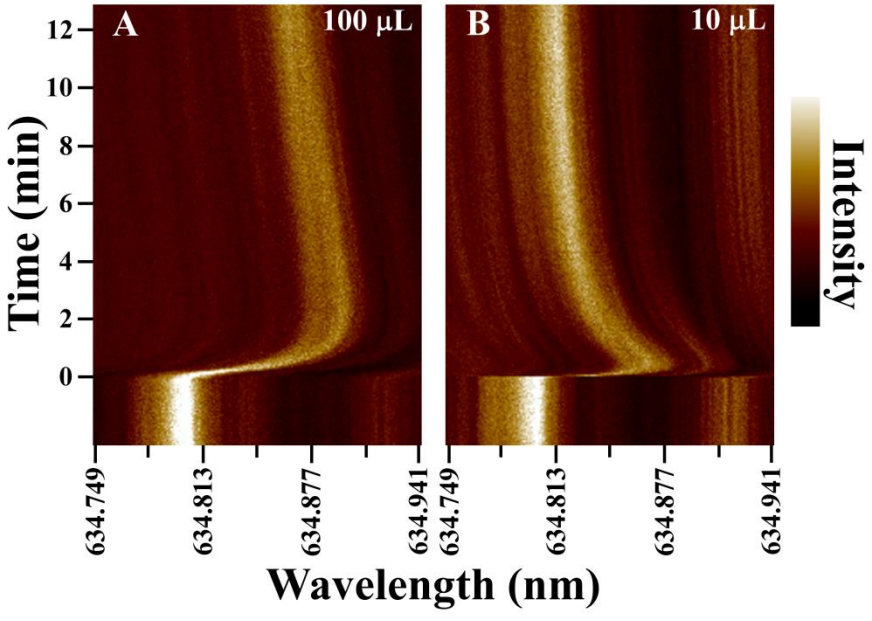

Figure 4.8. Comparison of the WGM response in unstirred 100 µL (A) and 10 µL (B) water droplets following a saline injection to raise the refractive index 0.002 RIU. The same WGM resonator was used in both experiments. Convective mixing in the droplets equilibrates the solution in minutes, with the smaller droplet requiring less time.

Evaporation leads to convective mixing in droplets, which offers an intriguing route for increasing analyte mass transfer to the sensing element. Counter rotating vortices are observed in evaporating droplets that create distinct flow patterns within the drop.[21-25] For multicomponent droplets, such as those used in assays, evaporative associated density gradients also develop within the droplet and can contribute to increasing internal flow velocities.[23, 24] These flow velocities can be orders of magnitude greater than diffusive flow. This offers an intriguing route for increasing mass transport to the sensing surface. However, as illustrated in **Fig. 4.8**, even with these convective flows, complete mixing takes minutes as measured by refractive index changes at the WGM resonator. Even for small droplets (10 µL), the signal in **Fig. 4.8B** requires approximately 10-12 minutes to relax to its new equilibrium value following the refractive index spike. When compared with the evaporation data in **Fig. 4.6**, these mixing rates are not sufficiently fast to avoid complications from evaporation. This suggests that convective mixing in sessile droplets is not adequate and active mixing is required to achieve sufficient mass transfer rates.

4.3.5 Investigating Droplet Mixing: Convective versus Active

Active mixing increases the transport of analyte to a sensor surface.[10] To accomplish this, a 125 μm diameter optical fiber was positioned in the droplet as shown in **Fig. 4.5C**. The fiber was rotated at ~5,000 rpm to vigorously mix the small droplet during the NaCl solution spike. The results are summarized in **Fig. 4.9**, which compares the response time in an unstirred 10 μL droplet with that of a stirred 10 μL droplet using the rotating rod. A significant improvement in sensor response time is measured in the stirred droplet. Both traces show an initial large shift in WGM resonance as the refractive index spike is delivered into the droplet. For the stirred droplet, however, the signal quickly relaxes to the equilibrium value in seconds as efficient mixing equilibrates the droplet following injection.

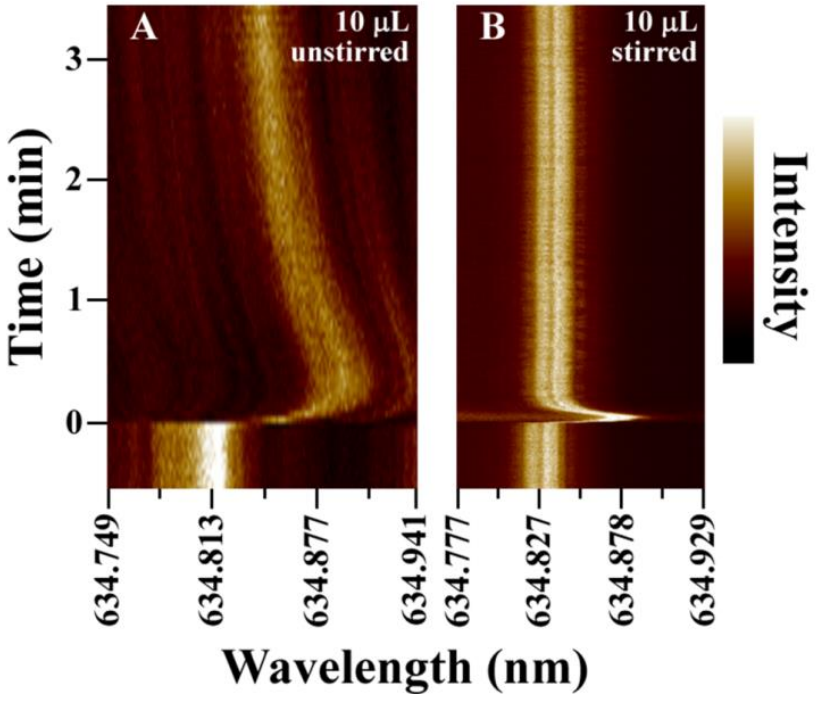

Figure 4.9. Comparison of the WGM response in unstirred (A) and stirred (B) 10 μL nanopure water droplets following injection of saline to increase the refractive index 0.002 RIU. For measurements on actively mixed droplets, a 125 μm diameter glass rod was inserted into the drop and rotated at ~5,000 rpm as shown in **Fig. 4.5C**. With stirring, the WGM resonance establishes the new equilibrium value within seconds of injection.

These initial investigations indicated 10 μL droplets with active stirring are best suited given the 10 minute time window due to evaporation constraints. This optimized droplet system was used in further investigations for the rapid detection of refractive index changes.

4.3.6 Refractive Index Calibration

To validate that active mixing enables reliable sensor response in small droplets, **Fig. 4.10** shows a representative refractive index calibration plot. For these measurements, a 10 μL droplet of nanopure water loaded with 38 μm diameter barium titanate resonators was supported on a hydrophobic Teflon AF surface. While stirring, 1 μL additions of 1.7 M NaCl solutions were spiked into the droplet to increase the refractive index and WGM resonance shifts were tracked in real time. **Figure 4.10** indicates the linear trend (R^2 = 0.995) between the measured resonant wavelength (taken 1 minute after each injection) and the calculated droplet refractive index. Importantly, the entire calibration was completed in less than 10 minutes with a measured limit of detection of 6.2 x 10^{-4} RIU.

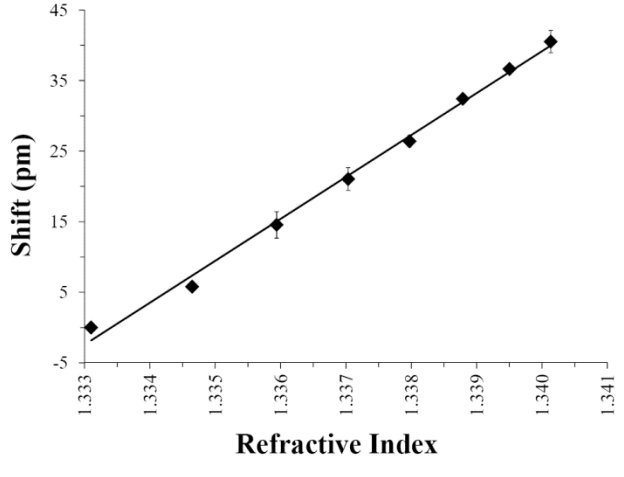

Figure 4.10. Refractive index calibration plot for an unmodified 38 μm WGM resonator in a stirred 10 μL water droplet. Injections of 1.7 M NaCl stock solution were used to increase refractive index. The calibration plot indicates a linear response (R^2= 0.995) and measured limit of detection of 6.2 x 10^{-4} RIU. Error bars represent intra assay variability (N=3).

Using WGM resonators in this small volume system provides a rapid analytical system for the determination of refractive index changes. In order to investigate biosensing in small volumes, resonator surface modifications were required. Real-time binding of streptavidin to BSA-biotin functionalized microspheres were monitored using WGM resonators in small volume droplets. Various functionalization procedures were used in order to optimize surface coverage of the capture molecules.

4.3.7 Microsphere Functionalization for Biosensing

The specificity of a label-free biosensor is achieved by chemical modification of the device's surface. Appropriate capture molecule selection and the quality of the surface functionalization are both key for optimizing the performance of a biosensor.[10] Biotin-streptavidin was used as a model system to investigate surface modification schemes using WGM imaging. Both covalent and non-covalent chemistries were investigated to attach the capture probe, BSA-biotin, to the surface of microsphere resonators. Furthermore, spotting procedures were investigated as a method to optimize surface coverage while reducing reagent volumes required. Using spotting procedures, the amount of reagent required was reduced from 2 mL to 20 μL and minimal agitation of the microspheres occurred during incubation. The same surface chemistry procedure and similar number of spheres were incubated for each modification scheme. In total, five surface modifications were investigated using WGM microsphere resonators.

Three of the investigated methods relied on non-covalent interactions of the capture probe with a charged microsphere surface. For these procedures, microspheres were either plasma cleaned, incubated with APTES, or incubated with poly-l-lysine (see experimental section). Alternatively, two investigated methods used covalent attachment chemistries by spotting or batch processing procedures. Individual assays were completed with each surface modification to determine sensor response.

Post activating the surface with the desired chemistry, spheres were incubated with 2 mg/mL of BSA-biotin for 2 hours for immobilization. For analysis, spheres were placed on a Teflon AF coated slide, immersed in 10 μL of PBS and a 1 μL spike of 1.9 μM streptavidin was injected into the droplet.

For each surface modification, WGM shifts due to biotin-streptavidin binding were monitored in real-time for individual assays, shown in **Fig. 5.11**. Overall, covalent attachment of the capture probe resulted in the largest sensor response. The microspheres which underwent batch processing for the covalent attachment of BSA-biotin (**Fig. 4.11**, filled diamonds) showed the largest sensor response, around 25 pm. The second largest response was observed from the covalent chemistry using spotting procedures (**Fig. 5.11**, filled circles).

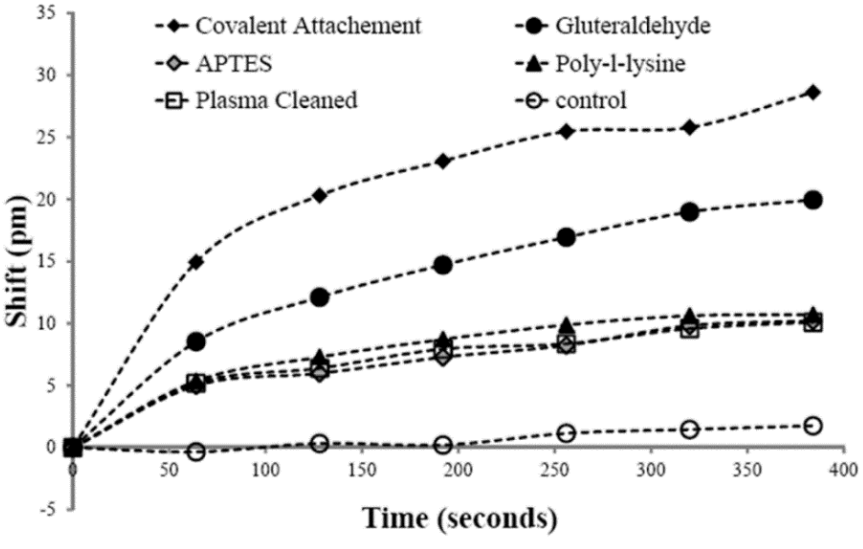

Figure 4.11. Surface functionalization methods were investigated to determine the most effective coverage of capture proteins on the surface of WGM microspheres. For each immobilization method, microspheres were incubated with BSA-biotin (2 mg/mL) for 2 hours, rinsed, then analyzed in 10 μL PBS droplets. I μL injections of 1.9 μM streptavidin were made and resulting WGM shifts were measured. The average shift for each immobilization method is plotted versus time (N = 3).

The three charged microsphere surfaces due to microsphere plasma cleaning, incubation with APTES, or poly-l-lysine, showed similar resonator responses. Plasma cleaned microspheres (**Fig. 4.11**, open squares) had oxidized surface which helped to attract charged functional groups of the capture protein. Similarly, non-covalent interactions of the capture probe with APTES (**Fig. 4.11**, open diamonds) or poly-l-lysine (**Fig. 4.11**, filled triangles) surfaces resulted in sensor response of approximately 10 pm. As

a control, unmodified resonators were investigated and showed minimal to no biding of streptavidin when analyzed, as expected (**Fig. 4.11**, open circles).

The most active surfaces were achieved with the batch functionalized microsphere resonators which covalently attached BSA-biotin to the surface. These results confirmed the use of this chemistry procedure as an optimized surface coverage method. The covalent chemistry procedure was used to functionalize microspheres for further bioassay experiments.

4.3.8 Initial Binding Rates

Having confirmed covalent attachment of proteins leads to the most active sensor surface, initial binding rate studies were carried out in 10 μL droplets using biotin-streptavidin as a model system. For each assay, 38 μm diameter resonators functionalized with biotin were immersed in a 10 μL droplet of PBS. The droplets were mixed with the rotating optical fiber and 1 μL spikes of streptavidin/PBS stock solutions (0-7.6 μM) were quickly injected into the droplet. **Figure 4.12A** compares the time evolution of WGM resonances as a function of streptavidin concentration. Each trace in **Fig. 4.12A** represents multiple, separate assays using different functionalized WGM resonators to compare response times with streptavidin concentration. As expected, the initial rate of change and final equilibrium shift in the WGM resonance increases with increasing concentration of streptavidin added.

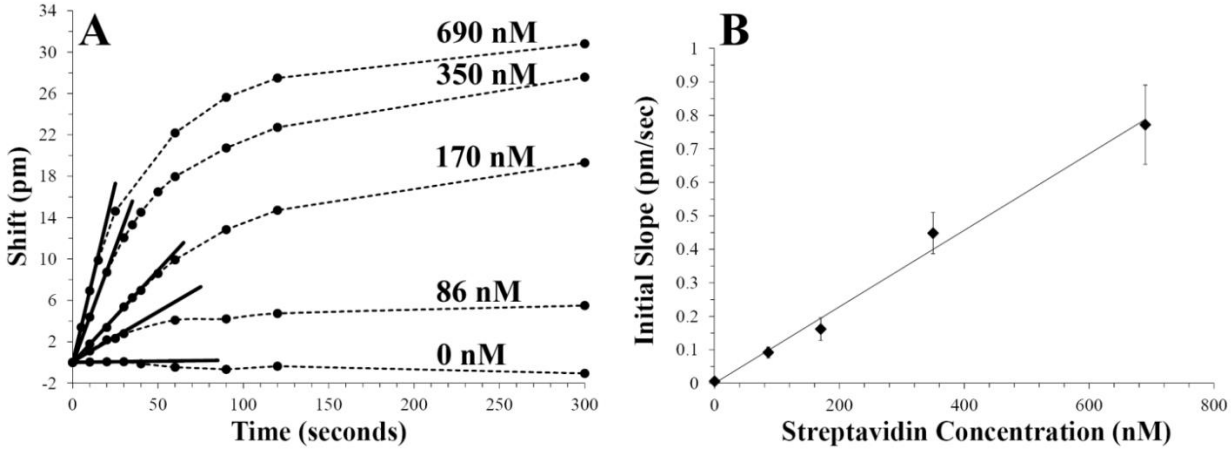

Figure 4.12. (A) For rapid protein quantification, biotin-streptavidin binding rates are measured as a function of streptavidin concentration. Each plot represents multiple, separate assays carried out in a 10 μL PBS droplet using rapid stirring. 1 μL injections of streptavidin/PBS solutions (0-7.6 μM) were quickly made in 10 μL PBS droplets containing BSA-biotin functionalized 38 μm spheres. Continuous measurement of WGM resonant wavelength shifts enables initial binding rates to be accurately quantified as a function of streptavidin concentration. Control experiments using unfunctionalized resonators showed no shifts following injections with 1 μL of 1.9 μM streptavidin/PBS (data not shown). (B) Initial binding rates measured from (A) are plotted versus streptavidin concentration showing the linear trend (R^2= 0.991). Initial binding rates are determined within the first minute following protein injection, enabling rapid quantification in a small volume. Error bars represent inter assay variability at each streptavidin concentration (N = 3).

With rapid stirring, **Fig. 4.12A** shows that WGM shifts reflecting initial binding rates can be quantified in the first 60 seconds following injection. Control experiments using unfunctionalized resonators, moreover, show that non-specific binding or droplet refractive index changes from evaporation do not contribute to the measured signals. Linear fits to the initial slopes in the binding data are shown in **Fig. 4.12A** and the extracted slopes are plotted as a function of added streptavidin in **Fig. 4.12B**. The linear response with protein concentration (R^2 = 0.991) illustrates the utility of this quantitative approach for quickly measuring nanomolar protein concentrations in small volumes.

4.4 Future Directions

Sensing in small volumes opens new opportunities for sample-limited applications. Small volumes combined with active mixing leads to very efficient mass transport of analytes to the sensing surface. This, combined with the favorable geometry and size of WGM resonators, results in rapid analysis times for nanomolar analyte concentrations. To extend these performance metrics, we are interested in utilizing WGM resonators as detectors for on-chip immunosensing. By using the WGM imaging approach, multiplexed detection can be incorporated with small volume systems which would greatly improve on-chip sensing capabilities. Initial investigations were completed to detect IL-6 and IL-10 in small volume droplets using WGM resonators.

4.4.1 Multiplexed Immunoassays in Small Volume Droplets

As discussed in previous chapters, multiplexed detection of serum biomarkers would greatly improve clinical diagnostic capabilities. Furthermore, assays capable of utilizing small volumes and incorporating fluid handling are advantageous for clinical implementation. Cytokines interleukin 6 (IL-6) and interleukin 10 (IL-10) have been reported to be elevated in serum samples of ovarian cancer patients.[36-38] Here, we aim to integrate label-free, multiplexed detection capabilities of WGM imaging with small volume droplets. Initial experiments were completed to detect IL-6 and IL-10 proteins in 10 μL droplets on a hydrophobic surface. Ultimately, these studies provide insight on utilizing WGM resonators as immunoassay sensors in digital microfluidic systems which would reduce costs, time and consumables required for a diagnostic test.

To detect cytokines using WGM resonators, capture antibodies and target antigens were obtained from ELISA kits (BD Biosciences) to ensure strong affinity between the antibody-antigen pairs. Microspheres were functionalized with IL-6 or IL-10 capture antibodies and submerged within a 10 μL PBS droplet on a hydrophobic surface. Injections of stock IL-6/PBS or IL-10/PBS solutions were made

to the droplets and the WGM resonant wavelength shifts were measured. **Figure 4.13** shows linear calibration curves for the detection of IL-6 (circles) and IL-10 (diamonds) in two separate assays.

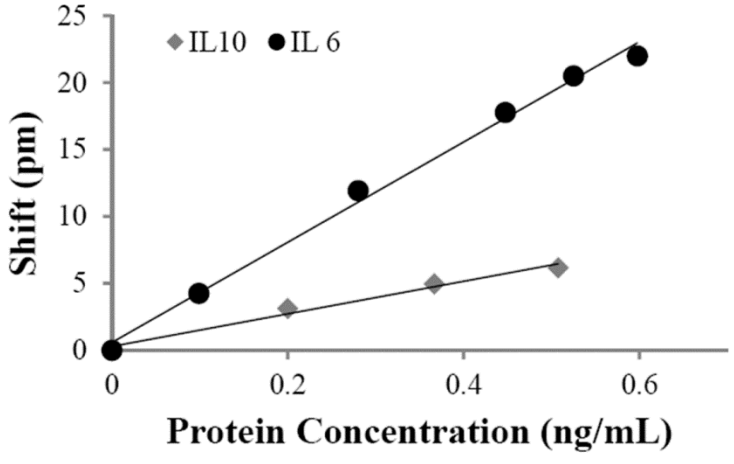

Figure 4.13. IL-6 (circles) and IL-10 (diamonds) were measured in separate WGM assays using functionalized microsphere resonators. IL-6 had a measured detection limit of 12 pm/ng/mL (R^2=0.983) while IL-10 had a measured detection limit of 37 pm/ng/mL (R^2=0.994).

Although the calibration curves were linear, control experiments revealed resonant wavelength shifts may be due to non-specific interactions. Lyophilized antigens provided in the ELISA kits were re-dissolved in PBS to prepare stock solutions (IL-6 2175 pg/mL and IL-10 2200 pg/mL). The lyophilized materials were determined to contain unknown salts, ions, and various proprietary molecules which were utilized by the manufacturer during protein purification. Once re-solubilized, these concentrated molecules altered the refractive index of the PBS droplet due to non-specific surface interactions. To address this issue, IL-10/PBS stock solutions were dialyzed in PBS for 24 hours to help remove impurities.

Figure 4.14 shows WGM shifts of unmodified resonators with the addition of 1 μL of IL-10/PBS stock solutions before (squares) or after (diamonds) dialysis. The results indicate dialysis helped to

remove some impurities because smaller WGM shifts were measured however, longer dialysis times or more extensive purification is required in order to further eliminate non-specific interactions.

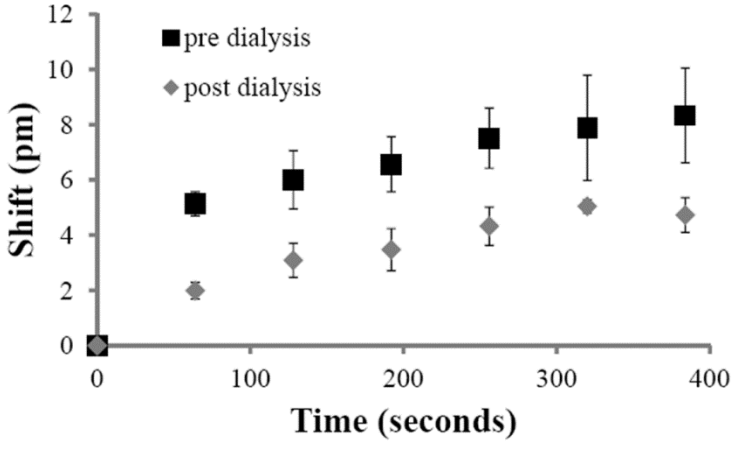

Figure 4.14. Analysis of bulk refractive index changes due to IL-10/PBS stock solutions. Unmodified microsphere resonators were placed in a 10 μL PBS droplet and a 1 μL injection of IL-10/PBS stock solution (2175 pg/mL) pre or post dialysis was made. The WGM shifts indicate a background signal due to bulk refractive index changes in the small volume droplet. IL-10/PBS stock solutions pre dialysis (squares) show WGM shifts up to 8 pm while IL-10//PBS post dialysis (diamonds) show less of a WGM shift around 4 pm. Error bars represent intra assay variability (N=3).

These results highlight a limitation of label-free detection- a vulnerability to false positive results. To address this, future work requires more extensive purification of the antigen solutions, identifying a different protein source, or more extensive blocking procedures for the functionalized microspheres. Importantly, we have demonstrated the ability to overcome non-specific interactions by detecting proteins in complex matrices, such as serum samples (discussed in Chapter 3).[39] Once overcoming non-specific interactions, we aim to utilize microspheres of different sizes within small volume systems for the development of a biosensing scheme which is both practical and accurate.

4.5 Conclusions

Small volume droplet assays utilizing WGM resonators are demonstrated as a promising label-free sensing platform for integration in a variety of miniaturized analytical systems. The geometry and size of WGM microspheres make them well suited for rapid mass transport and small volume analysis. The results presented here show that convective mixing in sessile droplets is not sufficiently rapid to enable nanomolar protein quantification on a time scale competitive with evaporation. Without active mixing, effects of evaporation on droplet volume, ion concentration, and protein concentration can all complicate protein quantitation using WGM resonators. However, active mixing of the small droplets using a small, spinning glass optical fiber is shown to result in rapid mass transfer and efficient sensing on short time scales. With active mixing, sensor response times are reduced to seconds, which enables nanomolar protein quantitation using initial binding rates within the first minute following injection. Lower concentrations requiring longer analysis times will eventually lead to complications arising from droplet evaporation which can be addressed using well-controlled environmental conditions or protective oil layers.

WGM resonators can be easily integrated as detectors in miniaturized analytical systems such as digital microfluidics. Using WGM resonators in droplet assays provides a rapid, on-chip detection scheme capable of multiplexed detection of protein and non-protein targets. We hope to take advantage of the high sensing capabilities and compact structure to expand the implementation of microsphere resonators in miniaturized analytical systems.

4.6 References

1. Srinivasan, V., et al., An Integrated Digital Microfluidic Lab-on-a-Chip for Clinical Diagnostics on Human Physiological Fluids. *Lab Chip* **2004,** *4* (4), 310-315.
2. Choi, K., et al., Digital Microfluidics. *Annu. Rev. Anal. Chem.* **2012,** *5*, 413-440.
3. Sista, R., et al., Development of a Digital Microfluidic Platform for Point of Care Testing. *Lab Chip* **2008,** *8* (12), 2091-2104.
4. Abdelgawad, M.; Wheeler, A. R., The Digital Revolution: a New Paradigm for Microfluidics. *Adv. Mater.* **2009,** *21* (8), 920-925.
5. Abdelgawad, M.; Wheeler, A. R., Low-Cost, Rapid-Prototyping of Digital Microfluidics Devices. *Microfluid. Nanofluid.* **2008,** *4* (4), 349-355.
6. Vergauwe, N., et al., A Versatile Electrowetting-Based Digital Microfluidic Platform for Quantitative Homogeneous and Heterogeneous Bio-Assays. *J. Micromech. Microeng.* **2011,** *21* (5), 1-11.
7. Miller, E. M., et al., A Digital Microfluidic Approach to Heterogeneous Immunoassays. *Anal. Bioanal. Chem.* **2011,** *399* (1), 337-345.
8. Cooper, M. A., Label-Free Screening of Bio-Molecular Interactions. *Anal. Bioanal. Chem.* **2003,** *377*, 834-842.
9. Fan, X., et al., Sensitive Optical Biosensors for Unlabeled Targets: A Review. *Anal. Chim. Acta* **2008,** *620*, 8-26.
10. Hunt, H. K.; Armani, A. M., Label-Free Biological and Chemical Sensors. *Nanoscale* **2010,** *2*, 1544-1559.
11. Luchansky, M. S.; Bailey, R. C., High-Q Optical Sensors for Chemical and Biological Analysis. *Anal. Chem.* **2012,** *84*, 793-821.
12. Patolsky, F., et al., Nanowire-Based Biosensors. *Anal. Chem.* **2006,** *78*, 4260-4269.
13. Kasianowicz, J. J., et al., Nanoscopic Porous Sensors. *Annu. Rev. Anal. Chem.* **2008,** *1*, 737-766.
14. Hwang, K. S., et al., Micro- and Nanocantilever Devices and Systems for Biomolecule Detection. *Annu Rev Anal Chem* **2009,** *2*, 77-98.
15. Dahlin, A. B., Size Matters: Problems and Advantages Associated with Highly Miniaturized Sensors. *Sensors* **2012,** *12*, 3018-3036.
16. Sheehan, P. E.; Whitman, L. J., Detection Limits for Nanoscale Biosensors. *Nano Lett.* **2005,** *5*, 803-807.
17. Squires, T. M., et al., Making it Stick: Convection, Reaction and Diffusion in Surface-Based Biosensors. *Nat. Biotechnol.* **2008,** *26*, 417-426.

18. Joensson, H. N., et al., A Homogeneous Assay for Protein Analysis in Droplets by Fluorescence Polarization. *Electrophoresis* **2012,** *33*, 436-439.
19. Li, L., et al., Superhydrophobic Surface Supported Bioassay - an Application in Blood Typing. *Colloids. Surf. B Biointerfaces* **2013,** *106*, 176-180.
20. Trantum, J. R., et al., Biosensor Design Based on Marangoni Flow in an Evaporating Drop. *Lab Chip* **2014,** *14*, 315-324.
21. Tam, D., et al., Marangoni Convection in Droplets on Superhydrophobic Surfaces. *J. Fluid Mech.* **2009,** *624*, 101-123.
22. Barmi, M. R.; Meinhart, C. D., Convective Flows in Evaporating Sessile Droplets. *J. Phys. Chem. B* **2014,** *118*, 2414-2421.
23. Kang, K. H., et al., Evaporation-Induced Saline Rayleigh Convection Inside a Colloidal Droplet. *Phys. Fluids* **2013,** *25*, 1-21.
24. Savino, R.; Monti, R., Buoyancy and Surface-Tension-Driven Convection in Hanging-Drop Protein Crystallizer. *J. Cryst. Growth* **1996,** *165*, 308-318.
25. Hu, H.; Larson, R. G., Analysis of the Microfluid Flow in an Evaporating Sessile Droplet. *Langmuir* **2005,** *21*, 3963-3971.
26. Ganic, D., et al., Three-Dimensional Evanescent Wave Scattering by Dielectric Particles. *Optik* **2002,** *113* (3), 135-141.
27. Chew, H., et al., Elastic Scattering of Evanescent Electromagnetic Waves. *Appl. Opt.* **1979,** *18* (15), 2679-2687.
28. Ashkin, A.; Dziedzic, J. M., Observation of Optical Resonances of Dielectric Spheres by Light Scattering. *Appl. Opt.* **1981,** *20* (10), 1803-1814.
29. De Angelis, F., et al., Breaking the Diffusion Limit with Super-Hydrophobic Delivery of Molecules to Plasmonic Nanofocusing SERS Structures. *Nat. Photonics* **2011,** *5*, 682-687.
30. Erbil, H. Y., Evaporation of Pure Liquid Sessile and Spherical Suspended Drops: A Review. *Adv. Colloid. Interface Sci.* **2012,** *170*, 67-86.
31. Hu, H.; Larson, R. G., Evaporation of a Sessile Droplet on a Substrate. *J. Phys. Chem. B* **2002,** *106*, 1334-1344.
32. Semenov, S., et al., Droplets Evaporation: Problems and Solutions. *Eur. Phys. J. Spec. Top.* **2011,** *197*, 265-278.
33. Birdi, K. S.; Vu, D. T., Wettability and the Evaporation Rates of Fluids from Solid Surfaces. *J. Adhes. Sci. Technol.* **1993,** *7*, 485-493.
34. Mangel, R. F., Jr.; Baer, E., Evaporation of Water Drops From a Teflon Surface. *Chem. Eng. Sci.* **1962,** *17*, 705-706.

35. Bourges-Monnier, C.; Shanahan, M. E. R., Influence of Evaporation on Contact Angle. *Langmuir* **1995,** *11*, 2820-2829.
36. Nolen, B. M.; Lokshin, A. E., Protein Biomarkers of Ovarian Cancer: the Forest and the Trees. *Future Oncol.* **2012,** *8* (1), 55-71.
37. Edgell, T., et al., Phase II Biomarker Trial of a Multimarker Diagnostic for Ovarian Cancer. *J. Cancer Res. Clin. Oncol.* **2010,** *136* (7), 1079-1088.
38. Amonkar, S. D., et al., Development and Preliminary Evaluation of a Multivariate Index Assay for Ovarian Cancer. *Plos One* **2009,** *4* (2), e4599.
39. Huckabay, H. A., et al., Label-Free Detection of Ovarian Cancer Biomarkers Using Whispering Gallery Mode Imaging. *Biosens. Bioelectron.* **2013,** *45*, 223-229.

Chapter 5

Advantages and Opportunities of Whispering Gallery Mode Microsphere Resonators

5.1 Introduction

Whispering gallery mode (WGM) microsphere resonators are promising detectors for bioanalytical platforms due to their sensitive label-free detection capabilities. By developing novel biosensing schemes using resonators, we have discovered advantages associated with WGM microspheres, as well as analytical challenges and opportunities for improved assay design. This chapter outlines investigations completed in order to optimize WGM imaging by characterizing sensing performance metrics of microsphere WGM resonators.

5.1.1 Advantages of Whispering Gallery Mode Imaging

In previous chapters, we have demonstrated the high degree of flexibility in the design of WGM imaging platforms. Importantly, the WGM excitation and detection schemes can be varied in order to optimize the platform based on the analytical need. For microsphere excitation, we have previously shown WGM resonators can be excited by utilizing the evanescent wave produced by the high numerical aperture of a total internal reflection (TIR) microscope.[1] This excitation scheme limited the number of microsphere resonators which could be excited within the field of view. To overcome these limitations, alternative coupling schemes can be utilized.

Other sources for evanescent coupling include tapered optical fibers, polished fiber tips, or prisms.[2-6] As discussed in Chapter 2, Optical fibers are often utilized to couple light to WGM resonators and can be advantageous for the development of remote, field deployable sensors. Furthermore, tapered optical fibers can provide almost perfect coupling, achieving 99.99% coupling efficiency in previous studies.[2, 7] However, traditional schemes utilizing thin optical fibers (< 3 μm diameter) require tedious and precise alignment which is difficult when working with fragile system components and greatly reduces throughput capabilities.[8] As a more robust system, we demonstrate the advantage of utilizing a Dove prism to evanescently couple light into an array of microspheres, demonstrated in Chapters 3 and 4. While prisms are limited to 80-90% coupling efficiency, the WGM set-up is greatly simplified and more robust.[2] Furthermore, prism coupling is advantageous for the simultaneous excitation of tens to hundreds of WGM microspheres. Given the variety of coupling schemes, an appropriate option can be selected based on the analytical goal. In addition to varying the coupling scheme, the detection of WGM resonances can be optimized and adjusted based on the desired experimental measureable.

The flexibility of detecting resonances using WGM imaging has been demonstrated by utilizing a CCD camera, or alternatively, a single element detector.[9, 10] Using a CCD camera, hundreds of microspheres can be imaged simultaneously. For multiplexed detection, microspheres targeting a variety of antigens can be imaged simultaneously enabling a single assay to achieve high-content detection capabilities. Chapter 3 demonstrates high-multiplexed potential of WGM imaging by analyzing microspheres of different sizes to simultaneously detect proteins in a single sample.[9] Alternatively, rapid, real-time investigations can be made using WGM resonators and a single element detector, as discussed in Chapter 4.[10] Overall, these analytical investigations demonstrate the flexibility of WGM imaging for the development of low cost, high-content sensing platforms. Importantly, all of the discussed WGM imaging platforms utilize microsphere resonators. Microspheres contribute to the high flexibility of WGM imaging and are an advantageous geometry due to their high-Qs, straightforward fabrication, and low costs. In this chapter, we investigate microsphere resonators for the optimization of WGM imaging.

5.1.2 Microsphere Whispering Gallery Mode Resonators

One of the main advantages of WGM microsphere resonators is the immense flexibility these detectors provide in the development of analytical platforms. Microsphere resonators are available in a range of sizes and materials and, since they are formed from melts, have exceptionally smooth surfaces that lead to large quality factors (Q-factors).[11-13] For WGM sensing, microspheres are available in bulk from commercial sources, or can be made individually using straightforward in-house fabrication methods.

Commercially available microspheres, discussed in Chapters 3 and 4, are inexpensive and widely available in a range of sizes and materials. By utilizing pre-made microspheres, fabrication time is decreased and assay throughput is significantly increased. Importantly, microspheres of particular sizes can be purchased in large numbers at low costs. Batches of spheres can be functionalized simultaneously which reduces tedious and individual functionalization requirements. Given these advantages, the majority of our investigations using microsphere WGM resonators have been completed using barium titanate doped glass microspheres (n = 1.93) from Mo-Sci Corporation (Rolla, MO). These commercial microspheres have demonstrated advantages for multiplexed, label-free biosensing applications. Some of the disadvantages associated with commercial microspheres include sphere-to-sphere performance variability. In this chapter, we discuss challenges associated with utilizing batch produced microsphere resonators. To optimize WGM imaging platforms, we investigate alternative microsphere sources.

An alternative approach for microsphere WGM resonators involves producing single, pure silica microspheres using standard melting processes.[2, 3] Microspheres can be fabricated by heating the end of a tapered optical fiber to form a pristine, smooth glass surface. As the taper is heated, surface tension pulls the melted glass tip into a spherical shape, forming a WGM microsphere resonator. The resulting silica microsphere is attached to a fiber stem which allows for manipulation and precise placement of the resonator. Using heating methods, microspheres 10 to 200 μm in diameter are produced.[2] This fabrication method is advantageous for high-Q resonators, however, it greatly limits assay throughput as each individual microsphere requires tedious procedures and multiple steps for formation and

functionalization before utilized as a sensor. Initial investigations of fiber microsphere resonators are presented as well as a discussion of how they can be integrated into novel WGM sensing schemes.

5.2 Materials and Methods

5.2.1 Materials

Barium titanate microspheres were obtained from Mo-Sci Corporation (Rolla, MO). Single mode optical fiber was obtained from Thor Labs (Newton, NJ). All other reagents, unless otherwise noted, were purchased from Fisher Scientific (Hampton, NH) and used without further purification.

5.2.2 Preparation of Microspheres

Barium titanate microsphere resonators (38 μm in diameter) were thoroughly cleaned by rinsing several times with distilled water. Microspheres were stored at room temperature in water prior to use. Fiber microspheres were prepared using single mode optical fiber (630 HP). Fiber was stripped to remove outer jacket coating, cleaned with alcohol and placed in a P-2000 micropipette puller (Sutter Instruments) at the following settings: heat 250, velocity 5, delay 0, and pull 100. A fusion splicer (FSM-40S, Fujikura) is commonly used to align two optical fibers end-to-end and fuse them together using an electric arc. For our purposes, the splicer was used to heat a tapered fiber in order to form a microsphere. The tapered fiber was positioned ~2.5 mm away from the electrodes and heated by manually initiating an arc.

Position of the taper and number of arcs were adjusted to modify the diameter of the fabricated microsphere. **Figure 5.1** shows a resonator ~40 μm in diameter. This size was produced by positioning the tapered fiber ~2.5 mm away from the electrodes. To heat the fiber, the splicer was manually arced two times. The taper was repositioned ~2.5 mm from the electrodes before the second arc was initiated.

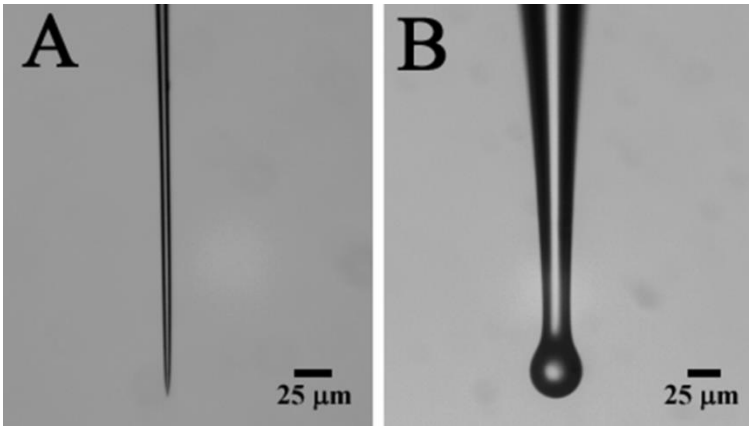

Figure 5.1. Images illustrating the fabrication of a fiber microsphere resonator. (A) Single mode optical fiber was stripped and placed in a P-2000 Micropipette puller to form a thin taper. (B) The taper was heated using an Arc Fusion Splicer. This particular fiber microsphere is ~40 μm in diameter.

Once formed, fiber microspheres were fastened to a metal post using UV adhesive, positioned above the Dove prism and analyzed using an inverted optical microscope (Zeiss Axiovert 100 TV) equipped with a 4x objective (Olympus PlanN, 0.01 NA).

5.2.3 Whispering Gallery Mode Imaging Set-Up

Light from an external cavity diode laser (TLB-6904, Newport Corporation, Irvine, CA) was free space coupled into a Dove prism creating an evanescent field at the center of the prism for launching light into the microresonators. To detect WGMs, scattered light from barium titanate microsphere resonators were imaged on a CCD camera (Cascade 650, Roper Scientific, Tucson, AR). For individual fiber microsphere resonators, scattered light was detected on an avalanche photodiode (APD) (SPCM-200, EG&G). Evanescently scattered light from resonators was collected from below using an inverted optical microscope (Zeiss Axiovert 100 TV) equipped with a 4x objective (Olympus planN, 0.10 NA). Diode laser scanning was controlled using LabVIEW (National Instruments, Austin, TX) or Digital Instruments Nanoscope IIIa.

5.2.4 Refractive Index Assays

Refractive index assays were completed to calibrate the response of barium titanate microspheres and individual fiber microsphere resonators. Microspheres were submerged within aqueous solution and injections of NaCl stock solutions were made to alter solution refractive index.

To preserve the pristine surface of fiber microspheres, it was important to analyze the resonators immediately following fabrication. A camera and video screen were used to monitor the approach of the fiber microsphere to a coverslip placed above the Dove prism in order to prevent unintentional contact with the substrate which may dampen the Q-factor and reduce sensitivity of the resonator.

5.3 Results and Discussion

5.3.1 Characterization of Barium Titanate Microsphere Resonators

While developing WGM imaging, we noticed barium titanate microsphere resonators had a wide range of performance characteristics. Some microspheres had higher Q-factors than others, while some were unable to support a WGM mode resonance for the excitation wavelength range investigated. Furthermore, for sensing, microspheres exhibited a wide range of refractive index sensitivities. This became problematic when analyzing multiple spheres in each assay, as each one required calibration of its response. In Chapter 4, we overcame sensitivity variations by measuring initial binding rates which were consistent from microsphere to microsphere. In this chapter, we completed refractive index assays to better characterize the performance of barium titanate microsphere resonators and investigate performance trends.

Initial investigations were completed to analyze sphere-to-sphere variability of barium titanate microsphere resonators (n = 1.93). Single refractive index assays were performed on a large number on microsphere resonators. For each assay, the Q-factors and refractive index sensitivity of individual microspheres were analyzed. Initial results, shown in **Fig. 5.2**, indicate a wide range of Q-factors observed for microsphere resonators of approximately the same size (38 +/- 3 μm). Q-factor differences

spanned an order of magnitude ranging from 10^3 to 10^4. The distribution of Q-factors is most likely due to imperfections of the microsphere surfaces and slight variability of microsphere diameters.

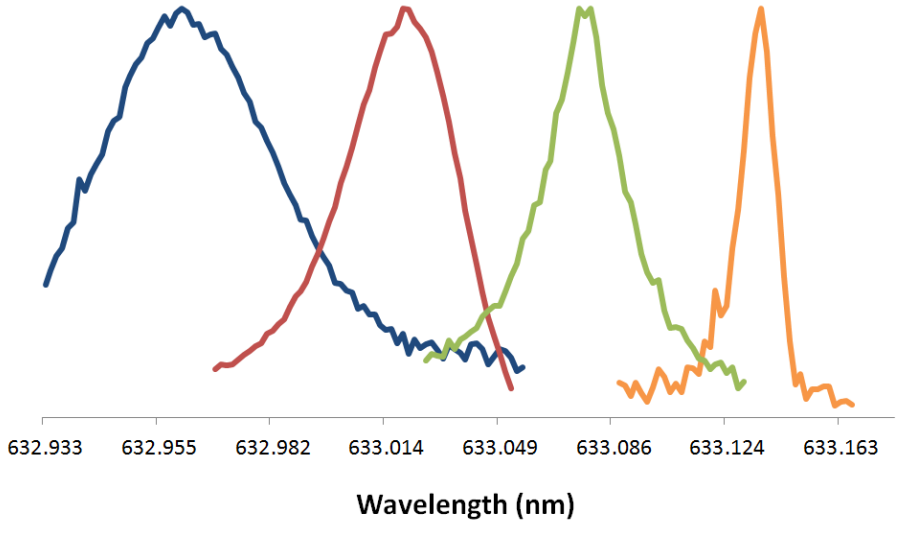

Figure 5.2. Representative Q-factors of various 38 μm diameter barium titanate microsphere resonators ranging from 1 x 10^3 to 6 x10^4. Within a single assay, a range of Q-factors are observed for microsphere resonators due to slight variations in microsphere sizes and surfaces.

During our investigations, we also noticed barium titanate microspheres consistently had better signal to noise and sharper peaks when analyzed in solution versus air. To further characterize sphere-to-sphere performance, microsphere resonant wavelength shifts were plotted as a function of solution refractive index changes. **Figure 5.3** shows corresponding linear calibration curves of 38 μm microspheres in a single assay with each line representing a sphere's response to refractive index changes. In a single assay, refractive index sensitivities ranged from 2 nm/RIU to 12 nm/RIU.

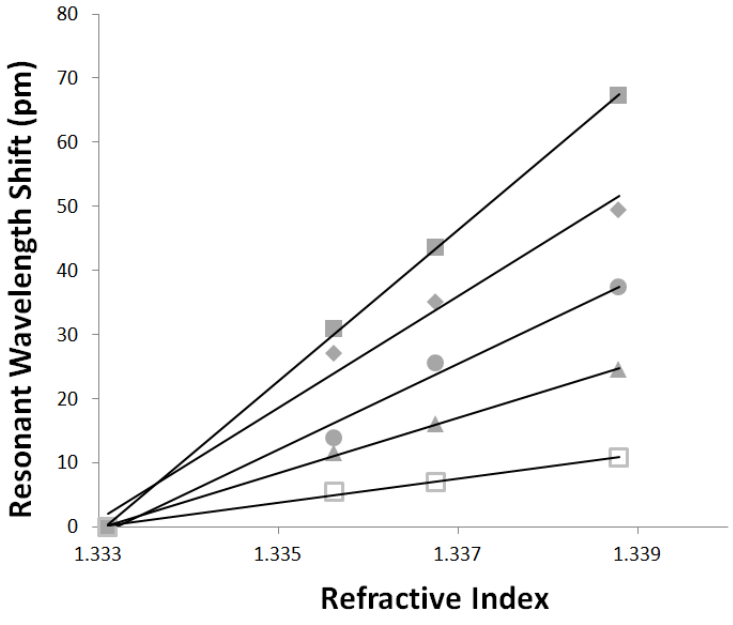

Figure 5.3. Several 38 μm diameter barium titantate microspheres were prepared and analyzed simultaneously in a refractive index assay. Plotted are the linear responses of selected microspheres to solution refractive index changes within a single assay. Refractive index sensitivities ranged from 2 nm/RIU to 12 nm/RIU, indicating variable sensitivities of individual microsphere resonators.

To determine if there was a correlation between an individual microsphere's Q-factor and refractive index sensitivity, **Fig. 5.4** plots the measured performance characteristics for each individual microsphere. Initial results reveal little overall correlation between Q-factors and refractive index sensitivities. Interestingly, some of the higher sensitivities measured correspond to lower Q-factors. Conversely, the highest Q-factors measured had moderate to low refractive index sensitivities. Although somewhat counterintuitive, low-Q resonators have been shown by others to be sensitive to refractive index changes.[14, 15] Measured sensitivities of low-Q microspheres are comparable to surface plasmon resonance capabilities and, in some cases, have shown improved mass sensitivity and lower detection limits.[14, 15]

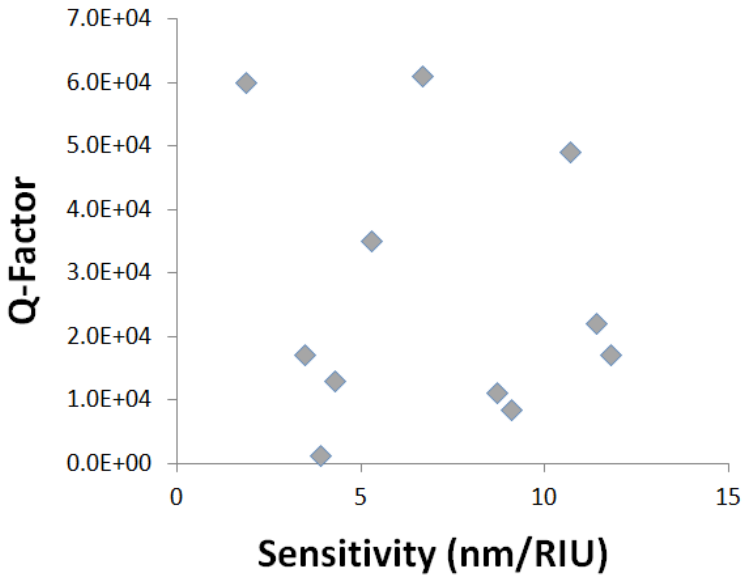

Figure 5.4. Q-factor plotted as a function of refractive index sensitivity for individual 38 μm diameter barium titanate microsphere resonators. No clear trend is observed, however initial results might indicate a relationship between low Q-factors and high refractive index sensitivity.

Overall, the majority of barium titanate microspheres investigated have relatively low Q-factors compared to reported microsphere Q-factors in literature, as large as 10^8-10^9.[13] To investigate microsphere resonators with enhanced performance characteristics, we were interested in alternative sources of microsphere resonators.

5.3.2 Characterization of Fiber Microsphere Resonators

Microspheres were fabricated from single mode optical fiber as described previously. The resulting resonators were analyzed to determine Q-factor and refractive index sensitivity in order to compare performance metrics to those of commercially available barium titanate microsphere resonators. Fiber microspheres were formed using a P-2000 micropipette puller to form a thin taper which was then heated using an Arc Fusion Splicer to form a microsphere. The fiber microspheres were lowered to a glass slide

above a Dove prism for evanescent wave coupling. Microspheres were imaged from below and the evanescently scattered intensity was collected using an APD. **Figure 5.5** compares the high Q-factor of a fiber microsphere to a barium titanate commercial microsphere, ~7 x 10^4. A typical fiber microsphere had a measured Q-factor of ~5 x 10^5. In air, the fiber microspheres consistently achieved Q-factors approximately an order of magnitude greater than barium titanate microspheres.

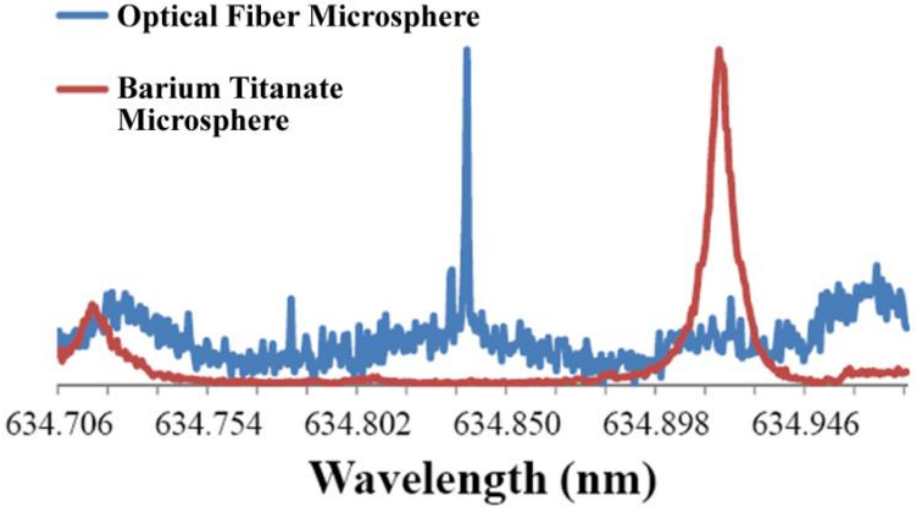

Figure 5.5. Resonant wavelength spectra for fabricated fiber microsphere (blue) and barium titanate microsphere (red) in air. Fiber microspheres typically achieved Q-factors around 10^5 while Q-factors for barium titanate microspheres were typically 10^4.

Additional investigations of the fiber microspheres were completed to characterize performance metrics. It was found that the Q-factors significantly decreased when the fiber spheres were analyzed in water versus air.[16] **Figure 5.6** shows resonant spectra of a single fiber microsphere in air (Q = 4 x 10^5) and in water (Q = 2 x 10^4), where the peak is observed to broaden when submerged in solution.

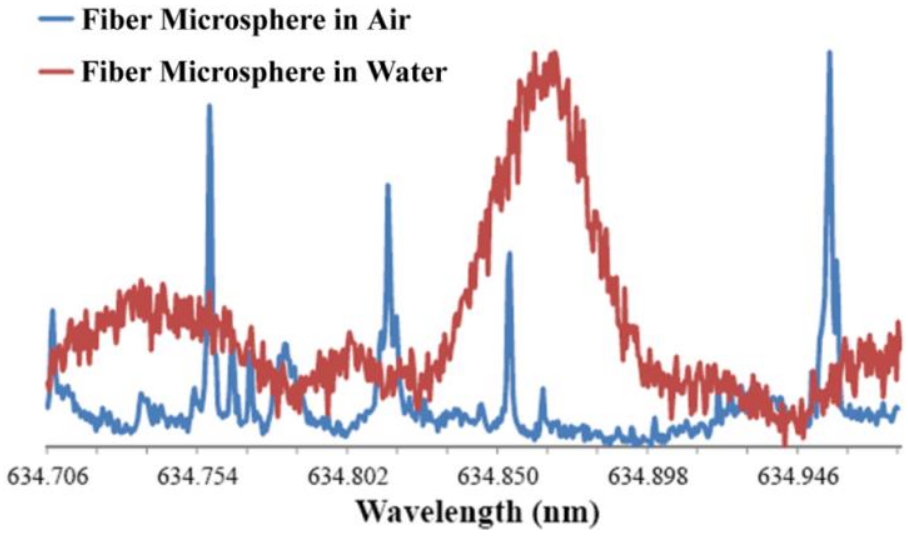

Figure 5.6. Resonant wavelength spectra of a single fiber microsphere in air (blue) and in water (red). The Q-factor significantly decreases when the fiber microsphere is analyzed in water.

Observed peak broadening is likely a result of WGM light loss when the microsphere is in solution. When in solution, the refractive index difference between the microsphere (n ~1.46) and surroundings (n=1.33) is smaller than when in air (n=1.00). Alternatively, this observation was not consistent for high refractive index barium titanate microspheres (n ~1.93) where higher Qs were consistently measured in solution. Moving forward, we can take advantage of these characteristic differences when optimizing the performance of WGM sensing platforms. Sensing characteristics of fiber microsphere resonators were further investigated by analyzing their sensitivity to solution refractive index changes.

For solution refractive index changes, fiber microspheres were immersed in a 10 μL aqueous droplet on a Teflon AF coated glass slide. Additions of NaCl stock solutions were made to increase the solution refractive index. **Figure 5.7A** shows the resonant wavelength shift with increasing solution refractive index and the corresponding calibration curve (R^2=0.995) with a measured sensitivity of ~43 nm/RIU. Although the Q-factors of fiber microsphere were reduced in solution, the measured solution refractive index sensitivity showed an improvement compared to commercially available barium titanate microspheres which ranged from 2 to 12 nm/RIU.

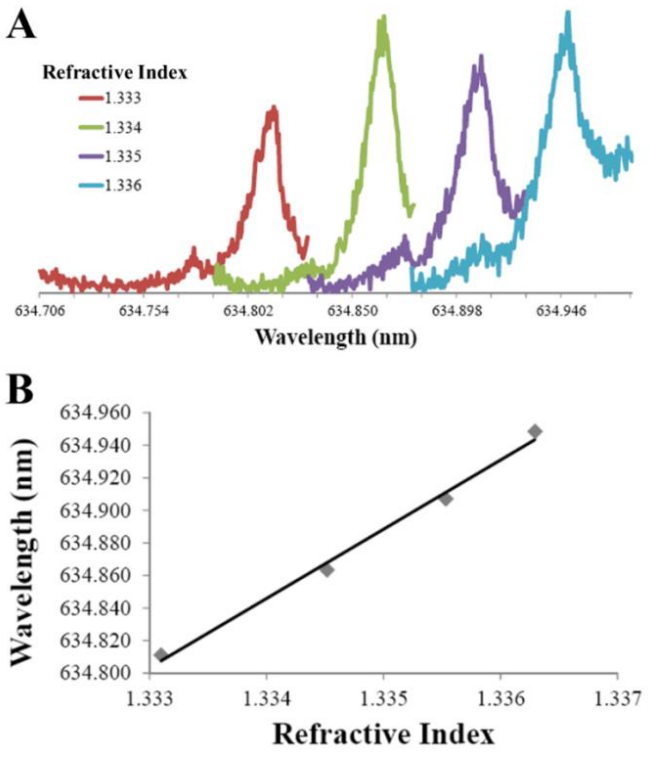

Figure 5.7. Analysis of solution refractive index changes using a fiber microsphere. (A) Spectral shifts indicate the resonant wavelength shifts to longer wavelengths upon the addition of NaCl to increase solution refractive index. (B) The linear calibration (R^2 = 0.995) shows a measured sensitivity of 43 nm/RIU. Fiber microspheres show an increase in refractive index sensitivity compared to barium titanate microspheres (~10 nm/RIU).

Initial results indicate fiber microsphere resonators have improved solution sensitivity compared to barium titanate microsphere resonators. Improved sensitivities and high Q-factors are advantageous for certain sensing schematics. However, throughput and multiplexed capabilities are reduced when using fiber microspheres due to required fabrication steps.

5.4 Conclusions

In this chapter, initial investigations of barium titanate and fiber microspheres were completed. Commercially available microspheres add flexibility and advantages to WGM imaging platform by

reducing fabrication, functionalization and costs associated with the assay. However, only moderate Q-factors and refractive index sensitivities are achieved. Typical Q-factors range from 10^3 and 10^4. Alternatively, microsphere resonators made from heating optical fibers have shown promising performance metrics with impressive refractive index sensitives and improved Q-factors in air. Silica microsphere resonators had a measured refractive index sensitivity ~43 nm/RIU. This sensitivity was greater than measured barium titanate microsphere sensitivities ranging from 2 nm/RIU to 12 nm/RIU. Furthermore, Q-factors around 5×10^5 were measured for fiber microspheres in air. Reduction of the Q-factor was observed when submerged in water. This could be modified by fabricating microspheres from higher refractive index materials. The improved sensing characteristics of fiber microsphere resonators may be advantageous for certain WGM imaging platforms. In future work, we hope to take advantage of these improved characteristics in the development of novel WGM sensing schemes.

5.5 References

1. Huckabay, H. A.; Dunn, R. C., Whispering Gallery Mode Imaging for the Multiplexed Detection of Biomarkers. *Sens. Actuators, B* **2011,** *160* (1), 1262-1267.
2. Ward, J.; Benson, O., WGM Microresonators: Sensing, Lasing and Fundamental Optics with Microspheres. *Laser Photon. Rev.* **2011,** *5*, 553-570.
3. Chiasera, A., et al., Spherical Whispering-Gallery-Mode Microresonators. *Laser Photonics Rev.* **2010,** *4* (3), 457-482.
4. Ilchenko, V. S., et al., Pigtailing the High-Q Microsphere Cavity: a Simple Fiber Coupler for Optical Whispering-Gallery Modes. *Opt Lett* **1999,** *24* (11), 723-725.
5. Spillane, S. M., et al., Ideality in a Fiber-Taper-Coupled Microresonator System for Application to Cavity Quantum Electrodynamics. *Phys. Rev. Lett.* **2003,** *91* (4), 043902/1-043902/4.
6. Gorodetsky, M. L.; Ilchenko, V. S., Optical Microsphere Resonators: Optimal Coupling to High-Q Whispering-Gallery Modes. *J. Opt. Soc. Am. B* **1999,** *16* (1), 147-154.
7. Vernooy, D. W., et al., Cavity QED with High-Q Whispering Gallery Modes. *Phys. Rev. A: At., Mol., Opt. Phys.* **1998,** *57* (4), R2293-R2296.
8. Fan, X., et al., Sensitive Optical Biosensors for Unlabeled Targets: A Review. *Anal. Chim. Acta* **2008,** *620* (1-2), 8-26.
9. Huckabay, H. A., et al., Label-Free Detection of Ovarian Cancer Biomarkers Using Whispering Gallery Mode Imaging. *Biosens. Bioelectron.* **2013,** *45*, 223-229.
10. Wildgen, S. M.; Dunn, R. C., Whispering Gallery Mode Resonators for Rapid Label-Free Biosensing in Small Volume Droplets. *Biosensors* **2015,** *5* (1), 118-30.
11. Vahala, K. J., Optical Microcavities. *Nature* **2003,** *424* (6950), 839-846.
12. Vollmer, F.; Arnold, S., Whispering-Gallery-Mode Biosensing: Label-Free Detection Down to Single Molecules. *Nature Methods* **2008,** *5* (7), 591-596.
13. Hanumegowda, N. M., et al., Refractometric Sensors Based on Microsphere Resonators. *Appl. Phys. Lett.* **2005,** *87* (20), 201107.
14. Himmelhaus, M., et al., Optical Sensors Based on Whispering Gallery Modes in Fluorescent Microbeads: Response to Specific Interactions. *Sensors* **2010,** *10*, 6257-6274.
15. Weller, A., et al., Whispering Gallery Mode Biosensors in the Low-Q Limit. *Appl. Phys. B: Lasers Opt.* **2008,** *90* (3-4), 561-567.
16. Hunt, H. K.; Armani, A. M., Label-Free Biological and Chemical Sensors. *Nanoscale* **2010,** *2* (9), 1544-1559.

Chapter 6

Development of Scanning Resonator Microscopy

Portions of this chapter were previously published in ACS Photonics:
Wildgen, S.; Dunn, R. Scanning Resonator Microscopy: Integrating Atomic Force Microscopy and Whispering Gallery Mode Resonators. ACS Photonics. 2015, 2 (6) 699-706.

6.1 Introduction

In this chapter, we discuss the development of scanning resonator microscopy (SRM) and demonstrate the technique by analyzing various material samples. By integrating microsphere resonators with conventional AFM probe tips, images of sample topography and optical properties can be collected simultaneously for improved refractive index sensing. SRM has the advantage of utilizing a single, unmodified resonator for the label-free analysis of surfaces. Using a single resonator overcomes sphere-to-sphere variation while reducing the chemistry and time requirements of microsphere surface modifications. For biosensing applications, multiplexed, high-throughput capabilities are achieved by integrating a single microsphere with scanning probe microscopy, thus, allowing a single sphere to interrogate a large sample area. Our interest is in the development and validation of SRM which can be applied to the characterization of polymers and materials.

6.1.1 Scanning Probe Microscopy

Scanning probe microscopies (SPM) encompass an ever-expanding suite of techniques capable of probing surfaces with high spatial resolution.[1, 2] These high resolution techniques have provided a depth of knowledge about materials, interfaces, and biomoleuclar surfaces. In general, SPM techniques scan a probe across a sample surface in order to produce an image based on electronic, mechanical, optical, or topographic properties of the material.[2] For the later, atomic force microscopy (AFM) has been demonstrated as a particular robust and widely applicable SPM technique for analyzing sample topography.[3]

6.1.2 Atomic Force Microscopy

Introduced in 1986, AFM is a versatile scanning probe technique for high-resolution imaging of surfaces.[3] AFM measurements on samples from robust solid-state materials to soft biological tissues have been reported in environments ranging from vacuums to aqueous solutions.[4, 5] As shown in **Fig. 6.1**, in AFM a sharp cantilever tip is scanned across a sample surface. A position-sensitive photodiode detector is used to measure deflections of the flexible cantilever probe due to tip-sample forces. Feedback signals adjust the tip-to-sample distance to maintain constant force between the tip and sample surface.

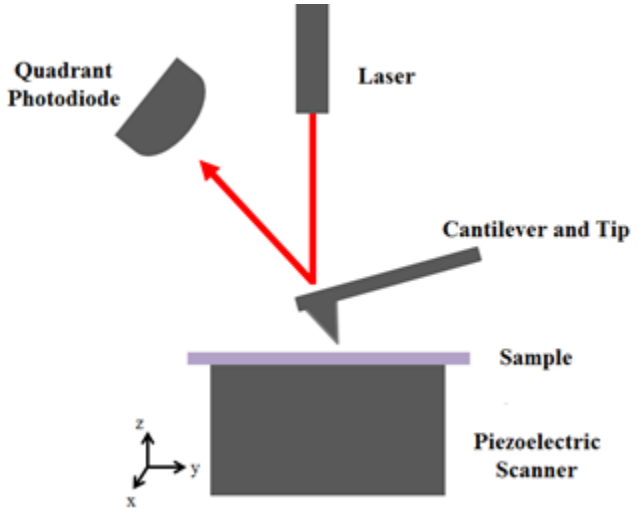

Figure 6.1. Schematic of atomic force microscopy instrumentation. A sharp cantilever tip raster scans a sample attached to a piezoelectric scanner. A laser is deflected from the cantilever surface to a photodiode detector for the adjustment tip height and maintain constant tip-sample force.

Although an extremely robust and well-established technique, alone AFM provides limited information about a sample material by measuring only sample topography. Incorporating additional measurements with AFM, such as chemical, electrical, mechanical or optical signals, allows for more specific information about a sample to be obtained during analysis. By making multiple measurements, topographical features can be correlated to additional properties providing a more thorough understanding of sample materials. A single platform which incorporates combined measurements is known as a hyphenated technique.

Hyphenated approaches couple analysis platforms together in order to provide high-content analysis of samples. AFM has proven to be a particularly flexible platform for developing hyphenated approaches. Since the technique revolves around sensing mechanical forces between the tip and the sample, it affords great flexibility in sample composition and working environment. Moreover, the robust and general mechanism for tip feedback can tolerate significant modifications to the tip, thus, facilitating the incorporation of new sensing mechanisms. Complimentary chemical, electrical, mechanical, and

optical capabilities have been all incorporated with AFM in order to expand analysis capabilities and increase specificity.[6, 7]

6.1.3 Hyphenated AFM Techniques

The most straightforward approach for increasing the capabilities of AFM involves chemically modifying the surface of a conventional AFM tip. In chemical force microscopy (CFM), tips modified with specific functional groups have been used to probe adhesion or frictional forces between the tip and surface of interest.[8, 9] More specific interactions have also been probed with tips functionalized with antibodies or other specific recognition sites.[10] Physically modifying a conventional AFM tip or replacing the tip altogether has enabled additional contrast mechanisms. For example, inspired by the success of scanning electrochemical microscopy (SECM)[11, 12], microelectrodes have been integrated into AFM tips to develop scanning electrochemical-atomic force microscopy (SECM-AFM).[13-16] This enables simultaneous measurement of topography and electrochemical properties at the mesoscale. Variations of this approach have been applied to imaging redox-labeled nanoparticles and, in the life sciences, for studying enzyme activity and cellular oxidation events.[17, 18]

Integrating optical contrast mechanisms with scanning probe microscopy has been a particularly active area of research given the large number of potential applications. For example, metal coated AFM tips have been used to develop tip-enhanced Raman spectroscopy (TERS).[19] Most work in this area, however, has focused on combining fluorescence sensitivity with the high-resolution force mapping. This combination is particularly informative in biological samples where correlations between fluorescently labeled species and surface topography can yield new structural insights. The most successful implementation is near-field scanning optical microscopy (NSOM). In apertureless NSOM, light scattered from a sharpened probe is used to excite fluorescence in the sample, while aperture NSOM uses specially fabricated fiber optic probes to deliver light to the nanometric dimension.[20, 21] This approach provides high-resolution fluorescence and topography information with single molecule detection limits.[22] However, for transmitted light applications where one wishes to probe optical properties such as

refractive index, aperture NSOM has proven problematic. Gap dependent coupling between the tip and sample often leads to artifacts in transmitted light images that are not easily controlled and can dominate the signal.[23] There is, however, great interest in measuring refractive index with high spatial resolution.

Refractive index probes a fundamental parameter of a material and has become increasingly important to map with high spatial resolution given recent developments in photonics and energy applications.[24-26] Refractive index is also commonly used to monitor binding events at surfaces for applications in sensing, screening and diagnostics.[27] Combining refractive index sensing with the high spatial resolution of AFM, therefore, can lead to new approaches for a range of applications including characterizing photonic materials and quantifying binding in high-density surface arrays. Furthermore, unlike fluorescence measurements, refractive index sensing does not require an intrinsic fluorophore or external tag and is not limited by photobleaching.

Combining refractive index sensitivity with AFM has been implemented using both surface plasmon resonance and ellipsometric approaches.[28-31] Ellipsometric approaches are attractive since they enable the complex refractive index to be measured, once suitable models are applied.[31] Often, however, the integration relies on combining two separate measurements onto the same microscope platform. This enables both measurements to be done in the same general area of the sample, but does not easily lead to high-resolution optical information or enable a direct pixel-by-pixel comparison between the optical and topography signals. More integrated approaches have used a conventional AFM probe to perturb an optical field at the sample interface and generate optical contrast.[28] While high-resolution contrast can be measured, this approach can suffer from coupling between optical and topographic information which makes image analysis problematic.

6.1.4 Scanning Resonator Microscopy

In this chapter, we develop scanning resonator microscopy (SRM) which combines refractive index sensing with AFM by integrating a small optical resonator at the end of a conventional AFM probe. Small, dielectric spheres, tens of microns in diameter, are easily attached to AFM probes and have been

used previously in force and optical measurements.[32-35] Here, we use these resonators to sense surface refractive index through changes in their whispering gallery mode resonances. The high Q-factors and narrow spectral linewidth ($\leq$ pm) of microsphere resonators leads to sensitive refractive index detection in a compact structure, well suited for integration with AFM.[36-38]

As discussed in previous chapters, WGM resonators respond to solution refractive index changes. Solutions around the microsphere can be altered to change the bulk refractive index which is measured by a corresponding resonant wavelength shift. This response has been investigated by our group, and many others, as a way to probe local refractive index changes due to binding events on the resonator surface. For biosensing applications, the immobilization of microsphere resonator with AFM has additional advantages. Utilizing an unmodified resonator to investigate various sample surfaces allows for the sensor to be reused which reduces the chemistry requirements and sphere-to-sphere performance variability.

In this chapter, we discuss the development of SRM by immobilizing a WGM resonator at the end of a conventional AFM cantilever allowing for simultaneous mapping of surface refractive index with topography. Calibration plots confirm that the WGM resonance of the tip bound resonator responds linearly with changes in substrate refractive index. The optical resonator also acts as the stylus in contact-mode AFM, enabling surface topographical features to be directly correlated with changes in surface refractive index. Material samples were prepared and analyzed using SRM in order to validate and demonstrate the scanning probe technique.

6.1.5 Scanning Resonator Microscopy for Material Characterization

A variety of material preparation methods were investigated in order to validate SRM. Upon validating the technique, we were interested in applying the imaging approach to the characterization of various material samples. By using the hyphenated AFM technique, materials were interrogated for optical and topographic properties simultaneously. Importantly, the analytical approach provided a non-

destructive, label-free measurement of unmodified surfaces. Specifically, we were interested in using SRM to investigate optical properties of thin polymer films and 2-D materials.

Thin polymer films are rapidly emerging as important materials for photonic applications where refractive index structures can be engineered into the films.[24-26] Devices such as optical waveguides rely on discrete patterning of materials with varying optical properties for efficient confinement of light.[25] Slight modifications of material refractive index can significantly affect the performance of these photonic devices. Furthermore, the optical properties of polymer thin films can vary based on deposition conditions, light exposure, and film thickness.[39] SRM provides a non-destructive analytical tool to measure refractive index properties of photonic devices. To accurately characterize fabrication methods, we hope to extend SRM to the analysis of photoreactive and fluorinated polymer thin films. Additionally, we are interested in investigating fundamental optical properties of materials using SRM.

2-D materials are gaining much interest due to the potential impact in numerous fields including energy, electronics, coatings, and sensing.[40, 41] Interest in graphene has existed for many years, yet optical properties of the material are not fully characterized. Current analysis techniques make it difficult to simultaneously determine graphene height and optical properties. SRM provides a way to overcome this limitation by analyzing graphene height and refractive index with a single approach. In this chapter, we discuss the development and validation of SRM and apply the technique to the analysis of materials including photoreactive polymers, fluorinated polymers and graphene oxide.

6.2 Materials and Methods

6.2.1 Materials

Barium titanate microspheres were obtained from Mo-Sci Corporation (Rolla, MO). Loctite UV curable adhesive was purchased from Cure UV (Delray Beach, FL). AFM cantilevers were obtained from Mikromasch (Lady's Island, SC) and Veeco (Plainview, NY). Glass substrates were obtained from ESCO Optics (Oak Ridge, NJ). LR White resin was obtained from Polysciences, Inc. (Warrington, PA).

Positive photoresist AZ 1518 was obtained from AZ Electronic Materials of EMD Performance Materials (Sommerville, NJ). Teflon AF was obtained from DuPont (Wilmington, DE). Azobenzene polymer poly(Disperse Red 19-p-phenylene diacrylate) (PE-DR 19) was obtained from Sigma-Aldrich (St. Louis, MO). All other reagents, unless otherwise noted, were purchased from Fisher Scientific (Hampton, NH) and used without further purification.

6.2.2 Tip Modification

To fabricate SRM probes, barium titanate microresonators (45, 53 or 63 μm diameter) were attached to the sides of conventional AFM cantilevers (MikroMasch CSC38) using Loctite 3525 UV curable adhesive, **Fig. 6.2**. The AFM cantilever shown is 350 μm long and 32.5 μm wide, with a nominal spring constant of 0.03 N/m (MikroMasch, CSC38).

To attach the resonators to the side of conventional AFM probes, microspheres and a drop of UV adhesive were spread on a PMMA surface. The AFM cantilever was positioned perpendicular to the surface and quickly dipped into the adhesive. Once lightly coated, the cantilever was removed and positioned next to a microsphere. With a resonator fixed to the side, the cantilever was lifted off the surface and UV light (UV75Thor Labs) was exposed to the tip (~30 sec.) to cure the adhesive. The microsphere resonator is positioned on the side of the cantilever in order to leave a pristine path around the sphere to support WGM resonances.

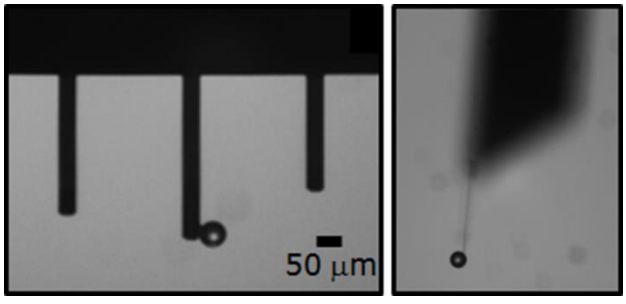

Figure 6.2. Image of microsphere resonator (53 μm diameter) attached to the side of a conventional AFM probe tip (MikroMasch CSC38). By attaching the resonator to the side of the cantilever, a pristine path was left for the recirculation of light along the circumference of the microsphere. It was important to position the microsphere as the lowest point of the probe tip because the cantilevers used still had styluses attached.

The high viscosity (9,500 to 21,000 cP) of Loctite 3525 allowed less glue to be used in order to attach the resonator, minimizing excess coating on the microsphere and cantilever surfaces. Excess adhesive resulted in high background scatter and complicated coupling of light into the WGM resonator.

6.2.3 Scanning Resonator Microscopy Instrumentation

For SRM instrumentation, **Fig. 6.2**, the modified microresonator tip was held in a Dimension AFM head (Digital Instruments) which uses laser light (543 nm) reflected from the end of the tip to generate the feedback signal. The sample is mounted below the tip on a Dove prism, which is held in an x-y closed-loop piezo scanner (Physik Instrumente) that raster scans the sample. The AFM head and sample scanner are mounted on an inverted optical microscope (Zeiss Axiovert 135) using a design similar to the Bioscope AFM (Digital Instruments).

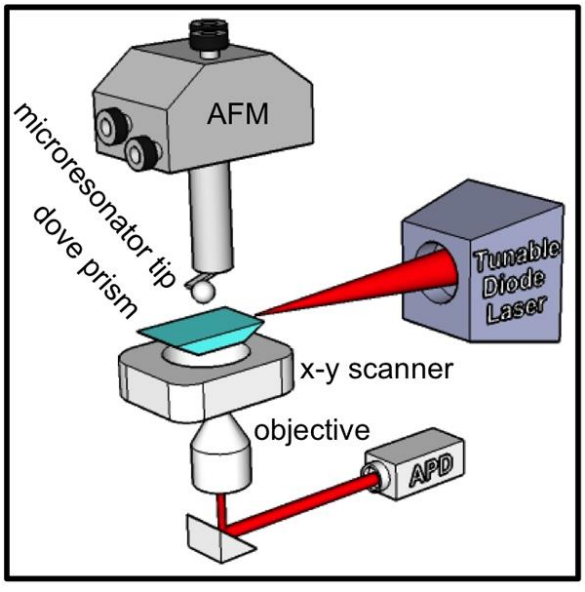

Figure 6.3. Schematic of the SRM set-up with a WGM resonator attached to the side of an AFM cantilever. Light from the modified AFM head provides the feedback signal when the probe is in contact-mode. The sample sits above the Dove prism, both of which are mounted on an x-y closed-loop piezo scanner. Light from a tunable laser is coupled into the Dove prism and, when the resonator is within the resulting evanescent wave, a WGM resonance is achieved.

WGM excitation from a tunable diode laser centered at 635 nm (New Focus Vortex II TLB-7000) is focused into the Dove prism, which refracts the light to the sample interface at an angle leading to total internal reflection. The evanescent field at the sample surface can couple light into the microresonator as the modified AFM tip is lowered into the field. To measure WGM resonances, evanescently scattered excitation from the tip was collected from below with the inverted microscope (Olympus Plan N 4x, 0.10 NA) and detected on an avalanche photodiode (APD) detector (SPCM-200, EG&G). Laser control, sample scanning, tip feedback, and signal collection were all integrated with a modified AFM controller and software (Digital Instruments Nanoscope IIIa).

6.2.4 Scanning Resonator Microscopy Measurements

SRM measurements were completed with the microresonator tip held at the sample surface in contact-mode feedback. For WGM spectral measurements, the tunable laser was scanned through the wavelength range (~270 pm) while the intensity of the evanescently scattered light from the microsphere resonator was collected from below. To calibrate the response of each tip, substrate refractive index was varied as indicated. All calibrations were done without sample scanning while holding the tip in feedback mode on the surface.

For SRM imaging, the diode laser was tuned to the WGM resonance of the tip and held at that particular wavelength during imaging. While the sample was scanned using the x-y piezo sample stage, simultaneous topographic and optical images were collected. All spectral measurements and imaging were carried out at room temperature under aqueous or dry conditions as specified.

6.2.5 Sample Preparation

This section outlines material sample preparation methods used in order to produce an appropriate sample for SRM analysis. Thin, transparent samples with micron features of varying refractive index were necessary to demonstrate SRM capabilities. Preparation of thin polymer films and graphene oxide sheets are discussed.

6.2.5.1 Ultrathin Material Samples

Transmission electron microscopy sample preparation methods were used to prepare thin material samples consisting of optical fibers or glass microspheres embedded in LR White resin. To prepare the samples, resin was added to small cell capsules along with the sample of interest (**Figure 6.4A**). Optical fibers were bundled together using heat shrink wrap prior to encapsulation (**Figure 6.4C**). All pre-polymerized capsules were kept up-right at 4 °C for 24 to 48 hours to remove air bubbles and allow the resin to permeate the sample. The resin was polymerized by heating the capsules to 50 °C for about

24 hours. Once cured, plastic casing was removed and a Dremel was used to carve out a small square section (~1 mm x 1 mm) containing the sample of interest, **Fig. 6.4**.

The sample was positioned in an Ultratome (Leica UC7), aligned with the diamond blade, and thin sections were sliced. Initially, slices 1 μm thick were cut at a rate of 0.6 mm/min. Once complete circular cuts were achieved the section thickness was decreased by ~250 nm. Reduction of the section thickness was repeated until samples 50 to 100 nm thick were achieved. For analysis by SRM samples were collected on glass microscope slides and stored at room temperature.

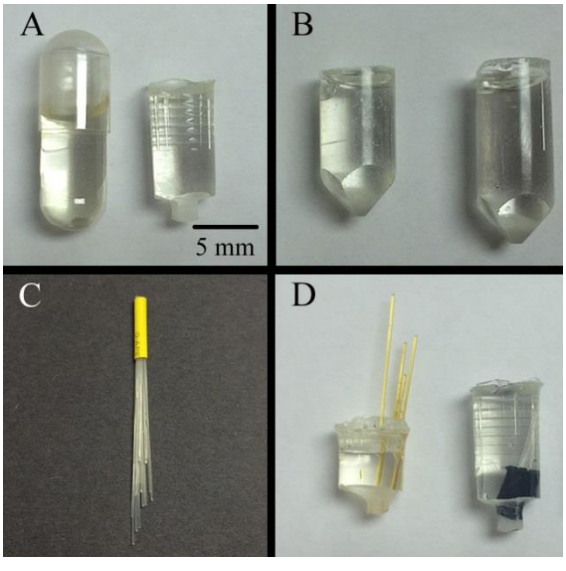

Figure 6.4. (A, B, D) Materials, optical fiber or glass microspheres, were embedded in LR White or EPON resin. Polymerized resin capsules were mounted on an Ultratome and thin slices were removed using a diamond blade. (C) Before embedding single mode optical fiber in resin, fiber bundles were prepared using heat shrink.

6.2.5.2 Positive Photoresist AZ 1518

To prepare AZ 1518 polymer thin films, unmodified AZ 1518 was spin cast (Brewer Science Cee 100) onto clean microscope slides to a thickness of 1-2 microns, as verified using surface profilometry (Tencor Alpha-step 200). Custom photolithography masks were designed in AutoCAD and fabricated by Infinite Graphics, Inc. Films were soft baked (2 min. at 100 °C), aligned with the mask, and then exposed

to 365 nm radiation (ABM Mask Aligner, i-line flood source) to modify the polymer structure. Exposure times varied from 15 to 30 seconds. Following exposure, samples were hard baked (10 min. at 100 °C) to remove residual solvent and increase the refractive index contrast.

6.2.5.3 Amorphous Fluoropolymer Teflon AF

Teflon AF thin films, 1 µl of 1% solution of AF2400 in fluorinated solvent FC40, were spin cast onto clean microscope slides. Films were baked (15 min. at 70 °C) to remove most of the solvent. No further baking steps were taken in order to enhance optical and height contrast of the thin film for SRM imaging.

6.2.5.4 Graphene Oxide Thin Films

High quality graphene sheets require deposition using expensive equipment and techniques, such as chemical vapor deposition.[42] Therefore, graphene oxide is often investigated as an alternative because of its increased solubility and ease of deposition on a variety of substrate materials.[42] Graphene oxide was synthesized from graphite by a modified Hummers method.[42, 43] For the reaction, 0.5 g of $NaNO_3$ was added to 1.0 g graphite in 24 mL of concentrated H_2SO_4 at 0 °C. While vigorously stirring, 3.0 g of $KMnO_4$ was slowly added. The solution was stirred for 60 min. at room temperature. After the formation of a thick paste, an additional 46 mL of water was added and stirred for 15 min. at 98 °C. To stop the reaction, 140 mL of water was added to the solution along with the slow addition of 10 mL of 30% H_2O_2, forming a yellow-brown suspension. The product was washed with 3% HCl until sulfate ions could not be detected with $BaCl_2$. The final product was rinsed with water until a neutral pH was reached, filtered and dried in a vacuum chamber overnight.

Graphene oxide solutions (0.1 mg/mL) were prepared in 50:50 solution of water:methanol and sonicated for ~60 min. Post centrifugation, ~5 µL of solution was pipetted onto clean mica sheets and spin cast at ~5,000 rpm for ~30 sec. Graphene oxide thin films were stored covered at room temperature.

6.2.5.5 Photoreactive Polymer PE-DR 19

Solutions of poly(Disperse Red 19-p-phenylene diacrylate) (PE-DR 19) in chloroform (0.5 mg/mL) were prepared. Heat, sonication and vortexing were used to help dissolve the polymer. Prior to spin casting, solutions were filtered (0.22 μm PTFE syringe filter) and stored at room temperature. Thin films of the polymer were prepared on clean glass slides and baked (15 min. at 60 °C). To alter refractive index of the polymer, the films were exposed to UV light by UV75 Light Gun (Thor Labs) or i-line flood source (ABM Mask Aligner).

6.3 Results and Discussion

By integrating WGM resonators with AFM, we aim to develop a novel scanning probe technique capable of simultaneously imaging topographic and optical properties of a sample. The SRM tip, **Fig. 6.5A**, consisted of a WGM microsphere attached to a conventional AFM probe. Attaching the microsphere to the side of the cantilever allowed a pristine path for WGM resonances.

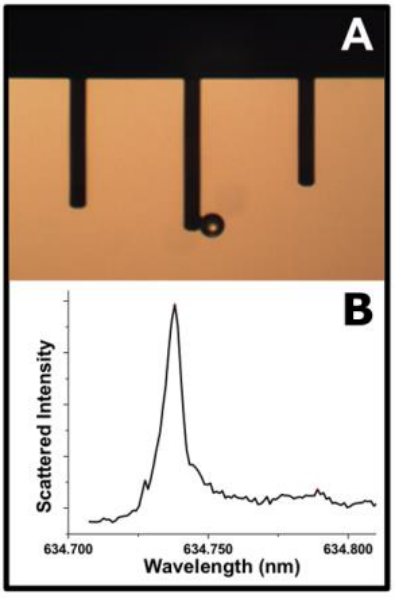

Figure 6.5. (A) Magnified view of AFM cantilever with 45 μm diameter barium titanate microsphere attached on the side. (B) WGM spectrum of the microresonator tip shown in (A). The spectrum ($Q = 1 \times 10^5$) was collected with the tip held in contact-mode at a glass surface under aqueous conditions.

Figure 6.5B shows the WGM spectrum of the modified microresonator AFM tip shown in **Fig. 6.5A**. The WGM resonance was measured while the tip was held in contact-mode feedback at a glass surface under aqueous conditions. Spectra are measured by collecting evanescently scattered light as the wavelength of the tunable diode laser is swept. Typical Q-factors measured for the modified microresonator AFM tips ranged from $5x10^4$ to $1x10^6$. The particular spectrum shown in **Fig. 6.5B**, for example, indicates a measured Q-factor of $1x10^5$ which is likely limited by over-coupling arising from the direct contact between the microresonator tip and sample surface.[44] It was important to validate the modified SRM tip was sensitive to refractive index changes.

Sensitivity of the SRM tip to refractive index was investigated by measuring the SRM tip's response to both solution and substrate refractive index changes. **Figure 6.6** plots the shifts in the WGM resonance as the refractive index of the surrounding solution was systematically increased with sucrose concentration (degrees Brix). A linear red shift (R^2 = 0.997) in WGM resonant wavelength with refractive index is observed in accordance with the expected trend resulting in a detection limit of ~3.7 x 10^{-3} solution RIU.

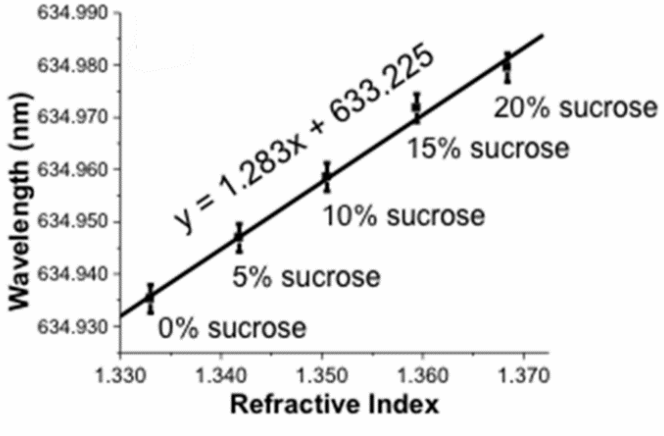

Figure 6.6. Refractive index calibration based on changes in sucrose concentration showing the expected linear trend (R^2 = 0.997) between resonant wavelength and solution refractive index with a measured detection limit of ~3.7 x 10^{-3} RIU. Error bars represent intra assay variability (N = 3).

SRM is a surface imaging technique, therefore, we needed to validate the ability of the microsphere to detect surface refractive index changes given the limited sample-interaction region. Substrates of various refractive index were positioned on the Dove prism which was coated in high index immersion oil. Resulting resonant wavelength spectra were measured. **Figure 6.7** shows resonant wavelength shifts for a SRM tip analyzing different substrate materials in air.

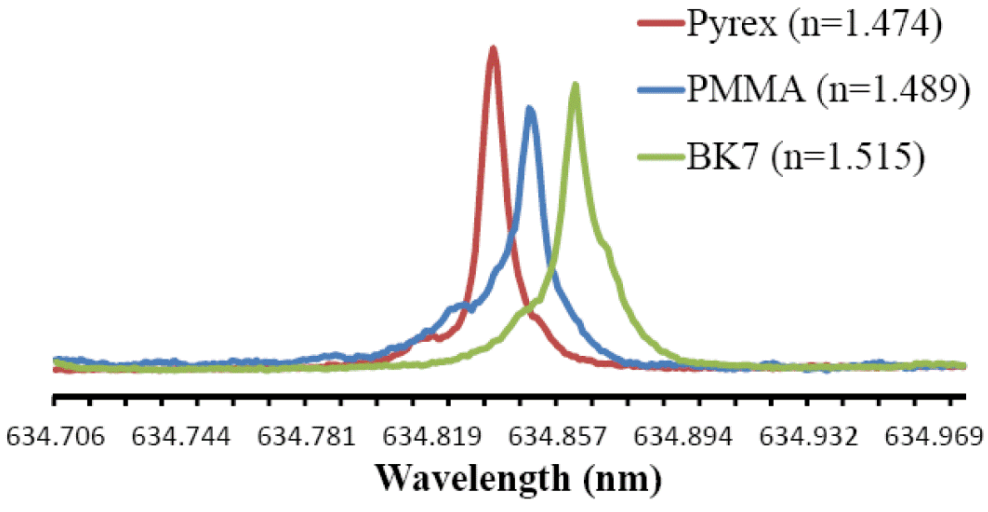

Figure 6.7. Spectral shifts measured for a SRM tip in contact-mode on various substrate samples: Pyrex, PMMA and BK7. The resonant wavelength shifts to longer values with increasing substrate refractive index.

Even though the sensing area is greatly reduced, the measured spectra indicate resonance shifts due to substrates of different refractive index. **Figure 6.8** shows a substrate calibration plot using the same microresonator tip calibrated previously (**Fig. 6.6**). In these measurements, the surrounding bath refractive index was held constant (nanopure water) while the surface refractive index was varied by changing the substrate. **Figure 6.8** shows the linear response (R^2 = 0.987) of the resonator to surface refractive index, albeit with reduced sensitivity and higher detection limit of ~1.5 x 10^{-2} substrate RIU due to the limited region of interaction between the resonator and the surface.

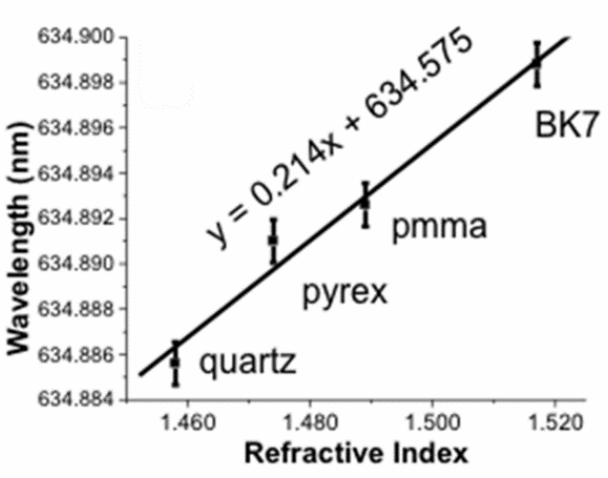

Figure 6.8. Same microresonator tip used in solution, now calibrated using changes in substrate refractive index while holding the surrounding refractive index constant (nanopure water). A linear trend (R^2= 0.987) is observed albeit with a decrease sensitivity resulting in a detection limit of ~1.5 x 10^{-2} RIU. Error bars represent intra assay variability (N = 3).

Having demonstrated that a SRM tip responds to surface refractive index, we focused on imaging refractive index contrast using the hyphenated scanning probe technique. For these measurements, the microsphere resonator will act as both the stylus to sense sample topography in contact-mode feedback and WGM resonator that responds to changes in surface refractive index.

6.3.1 Initial Scanning Resonator Microscopy Imaging

Figure 6.9 shows initial SRM imaging measurements of a cleaned glass microscope slide under aqueous conditions. The topography image in **Fig. 6.9A** reveals a small 36 nm high feature in the middle of the image due to contamination on the otherwise smooth glass surface. This feature corresponds to a large change in intensity observed in the corresponding WGM image. The SRM optical image in **Fig. 6.9B** was measured with the excitation wavelength held constant at 634.842 nm, corresponding to the WGM resonance of the microresonator tip on the glass surface. A large, reversible decrease in the

evanescently scattered light from the microresonator tip is observed in **Fig. 6.9B** as the microresonator tip scans across the feature.

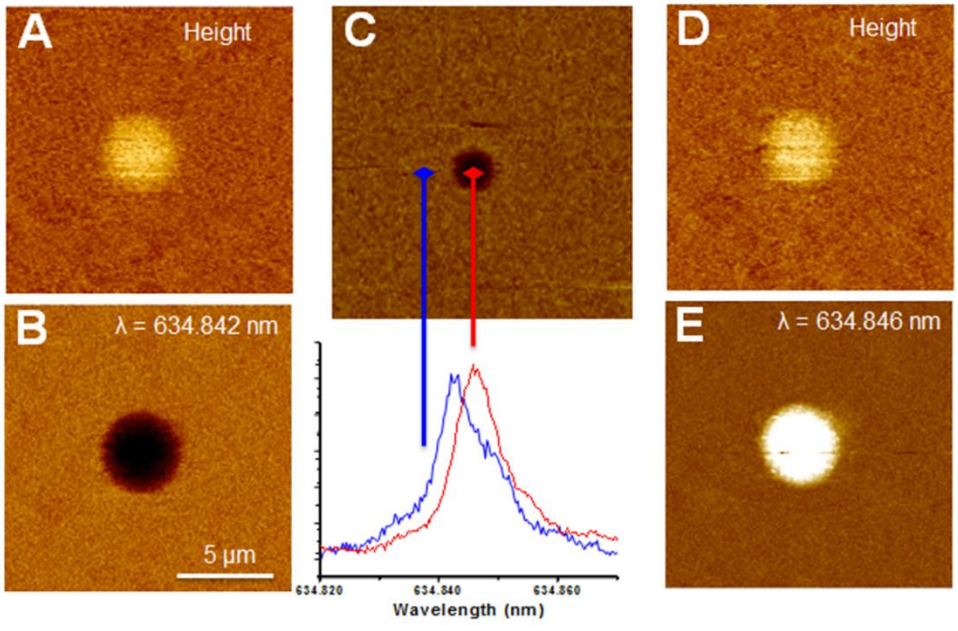

Figure 6.9. SRM topography (A) and optical (B) images (15 µm x 15 µm) of a cleaned glass substrate under aqueous conditions. The excitation wavelength is held constant at 634.842 nm, which corresponds to the WGM resonance of the tip on glass. (C) Spectra collected on and off the feature confirm the intensity decrease observed in (B) arises from a shift of the WGM resonance of the tip. SRM topography (D) and optical (E) images of the same sample region with the excitation now held at 634.846 nm which corresponds to the WGM resonance of the tip on the feature.

To confirm that the WGM contrast seen in **Fig. 6.9B** arises from spectral shifts and not coupling with the surface topography, the microresonator tip was positioned and held at the locations indicated in **Fig. 6.9C** while spectra were recorded. With the tip positioned 10 µm on either side of the feature, the WGM spectrum indicates a resonant wavelength at 634.842 nm. When the tip is centered on the feature, the WGM spectrum red shifts to 634.846 nm, thus, indicating a larger refractive index value than the surrounding glass substrate. These measurements confirm that the intensity contrast measured in **Fig. 6.9B** arises from variations in sample refractive index and not coupling between the topography and

optical signals. This is further confirmed in **Figs. 6.9D** and **E**, where the same sample area is imaged again but with the excitation wavelength tuned to match the WGM resonance of the tip on the feature at 634.846 nm. An increase in evanescent scattering from the tip is now observed at the center of the image as the microresonator tip comes into resonance when it crosses the sample feature. The measurements in **Fig. 6.9** illustrate the surface refractive index sensing capabilities of SRM, which are particularly useful for characterizing materials.

6.3.2 Ultrathin Material Samples

To further validate SRM, thin transparent material samples were prepared using transmission electron microscopy sample preparation methods. Ultrathin samples containing glass microspheres or optical fibers were prepared in LR White resin. For SRM imaging, we were interested in determining if the difference in refractive index of optical fiber core ($n = 1.46$) and cladding ($n < 1.46$) components could be resolved. Additionally, glass samples with known optical contrast were prepared using soda lime ($n = 1.52$) and barium titanate ($n = 1.93$) microspheres.

Sample materials were embedded in LR White resin which permeated the glass material and polymerized forming a hard capsule. Thin slices were removed from the resin capsule using an Ultratome diamond blade. **Figure 6.10** shows samples (~100 nm thick) of optical fibers embedded in resin collected on glass microscope slides.

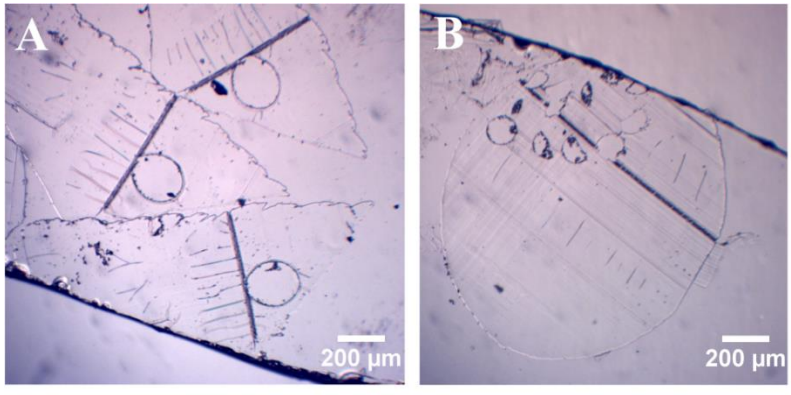

Figure 6.10. Brightfield image of ultrathin samples prepared using an Ultratome. (A) A multimode optical fiber or (B) single mode optical fiber bundle were embedded in resin and sliced thin (~100 nm) using the Ultratome diamond blade. The small circles show where the fibers are within the larger resin sample slice.

This sample preparation method created promising ultrathin samples, however, the samples were unable to achieve discrete optical features necessary to further validate SRM imaging capabilities. When analyzing the thin samples, circular areas corresponding to the embedded optical fibers or microspheres were determined to have variable heights. This may be a result of the resin not fully permeating the glass sample materials during the embedding process. Typically, LR White resins are used with fluid samples such as tissues or cells. To improve the fixation of the glass materials within the resin, longer incubation times or alternative resins should be investigated. Although the sample height was inconsistent, portions of the slices were determined to be an appropriate thickness for excitation of SRM tips.

The ultrathin films allowed for evanescent coupling of light to the SRM microsphere tip. However, resins showed a large amount of scatter from 635 nm light, resulting in a high background for APD detection. This significantly decreased optical sensitivity when imaging refractive index contrast due to changes in WGM scatter intensity. To overcome these difficulties, modifications to the SRM instrumentation can be made. Specifically, the coupling scheme can be modified for fiber excitation of the WGM microsphere. These modifications are further discussed in Chapter 7. To further demonstrate the SRM capabilities, an alternative sample with minimal height and known optical contrast was needed.

Furthermore, we were interested in utilizing SRM to improve the characterization of materials such as thin polymer films.

6.3.3 Positive Photoresist AZ 1518

Thin polymer films are important materials for the development of photonic devices, such as optical waveguides, which rely on patterned refractive index structures. Characterization of thin polymer films would help to improve and optimize fabrication of such devices. AZ 1518 is used extensively in microfabrication applications where thin films are easily fabricated on substrates by spin casting.[45]

To create refractive index test samples, standard photolithography techniques were used to expose thin films of AZ 1518 to UV radiation through the mask shown in **Fig. 6.11A**. AZ 1518 has a reported refractive index of 1.623 (632.8 nm), which shifts to lower values upon exposure to UV radiation as diazonaphthoquinone (DNQ) in the polymer undergoes a series of physicochemical changes that ultimately converts it to a carboxylic acid.[46-48] The final refractive index change in the exposed film depends on the degree of photoactivation and the amount of residual solvent remaining in the film following post exposure baking.[39] Following UV exposure, the films were baked to remove residual solvent but not processed further, leaving smooth polymer films with refractive index features encoded by the mask.

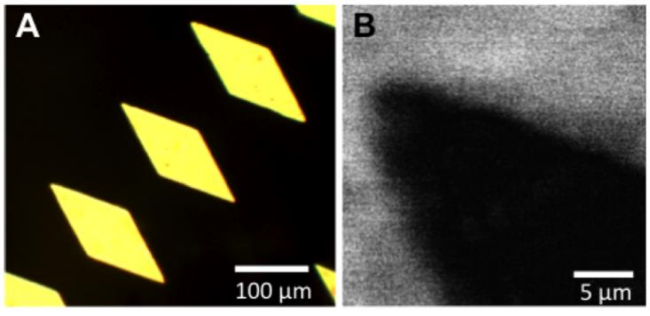

Figure 6.11. (A) Photolithography mask used to pattern thin films of the photoresist AZ 1518 with UV radiation. (B) SRM optical image of a thin polymer film following UV exposure. Scattered intensity decreases in UV exposed regions of the film as the WGM resonance of the microresonator tip shifts due to refractive index changes. Images were collected in air at room temperature.

Figure 6.11B shows a representative refractive index image of the thin film taken with SRM. The particular 45 µm diameter resonator tip used had a Q of $1x10^5$ and measured LOD of ~2 x 10^{-3} RIU. Images were collected while holding the excitation wavelength constant at 634.848 nm, corresponding to the tip resonance in contact with the unexposed regions of the polymer. In **Fig. 6.11B**, a reversible shift in contrast is observed as the microresonator tip scans across the exposed regions of the polymer film, accurately mapping the exposed mask feature. The lower intensity reflects reduced scattering from the microresonator tip as the change in refractive index shifts its WGM resonance. It is important to note that these films were imaged following exposure to UV light without any further development in order to visualize the structures. To gain a more quantitative view of the refractive index differences between the exposed and unexposed regions of AZ 1518 films, spectra were collected in both regions and the resonator was calibrated.

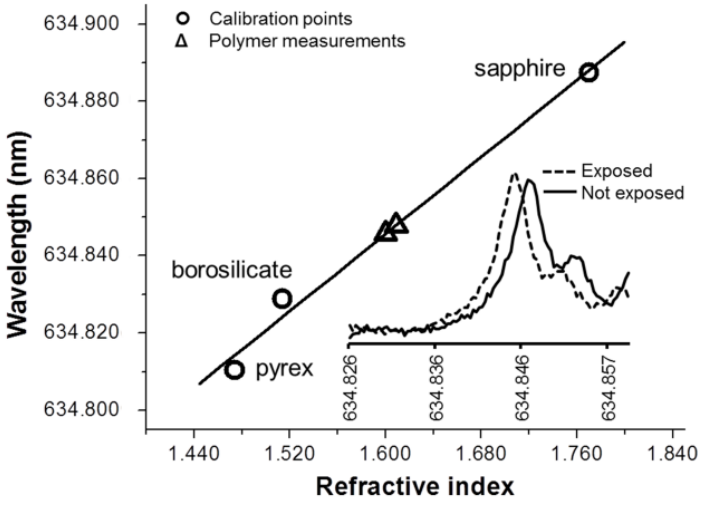

Figure 6.12. Calibration (circles) of the microresonator tip used in **Fig. 6.16** to quantify the changes in refractive index between exposed and unexposed regions of the polymer film (triangles). From this, the measured refractive index of exposed regions is 1.600 and areas not exposed is 1.610. Spectra were collected in air at room temperature.

The calibration plot shown in **Fig. 6.12** was used to calculate the refractive index values for both exposed and unexposed regions of the polymer film based on the measured WGM resonant wavelength of the tip in these regions (inset **Fig. 6.12**). From **Fig. 6.12**, the measured refractive index in unexposed regions is 1.610. This is lower than literature values of 1.623.[46] This difference may reflect residual solvent in the films or unintended exposure of these regions, both of which will lower film refractive index.[39] In exposed regions of the polymer, the measured refractive index is 1.600, reflecting the expected shift to lower refractive index following UV exposure.

To further explore the effect of exposure on AZ 1518 optical properties, a SRM tip was used to quantify refractive index of exposed and unexposed regions of AZ 1518 films. When preparing the samples, UV exposure energy per area was varied. Quantification of spectral shifts revealed increased exposure corresponded to larger refractive index differences (Δn) between unexposed and exposed regions of AZ 1518 thin films. Importantly, the observed trend was found to be repeatable and is

consistent with results measured by interferometry.[47] The results confirm increased exposure corresponds to higher optical contrast between unexposed and exposed regions of AZ 1518 films.

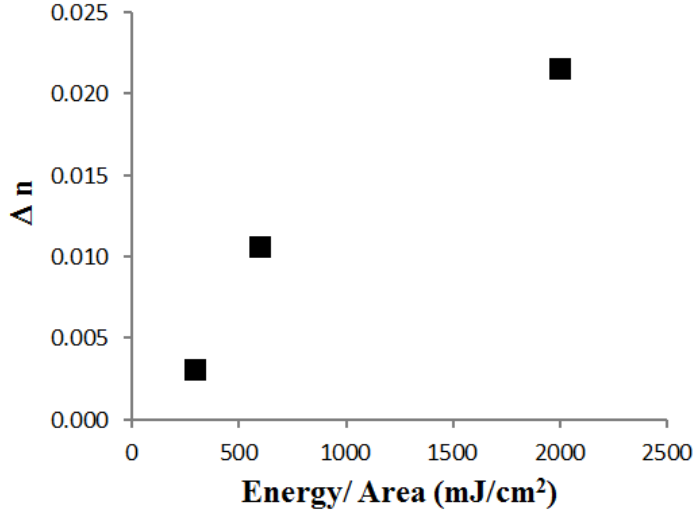

Figure 6.13. Magnitude of the refractive index differences (Δn) between unexposed and exposed regions of AZ 1518 films as a function of exposure (energy/area). The results were found to be repeatable when replicate samples were analyzed by the same SRM tip.

By analyzing AZ 1518 thin films, we demonstrated the capabilities of SRM for optical characterization of photoreactive polymer materials. To continue to investigate the capabilities of SRM, we expanded analysis to fluorinated polymer thin films. These materials are less sensitive to light exposure, thus, have stable optical contrast for investigation using SRM.

6.3.4 Amorphous Fluoropolymer Teflon AF

To further explore the imaging capabilities of SRM, thin films of Teflon AF were investigated. Teflon AF is a class of transparent amorphous fluoropolymers popular in optics and electronic applications due to their low refractive index (n = 1.29), high thermal stability, and robust chemical resistance.[49, 50] A 1% solution of AF2400 resin in fluorinated solvent FC40 was spin cast onto a glass substrate to produce a thin film. The films were baked at 70 °C for 15 min. to remove residual solvent

and imaged dry at room temperature. **Figure 6.14** shows typical SRM optical and topography images of a Teflon AF thin film on glass.

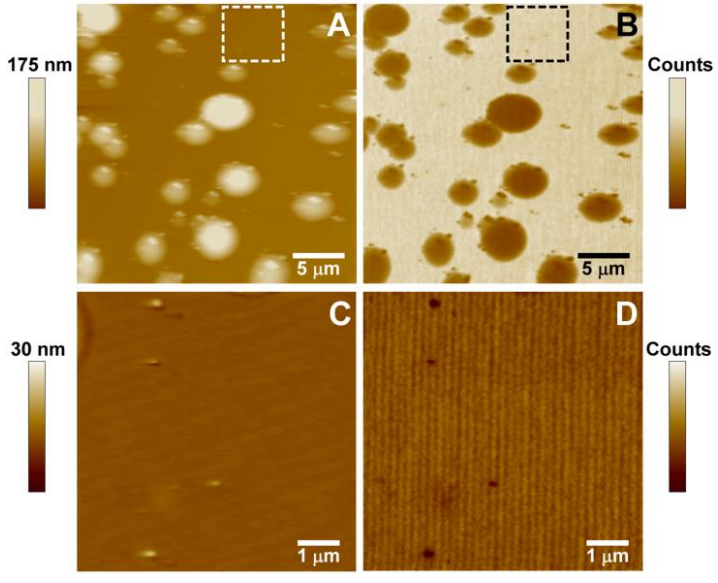

Figure 6.14. Simultaneously measured 28 μm x 28 μm SRM topography (A) and optical (B) images of a thin Teflon AF film in air at room temperature. Three contrast levels are observed in the SRM optical image with the darkest features (largest WGM shift) corresponding to small particles observed alone and within the larger domains. 8 μm x 8 μm SRM topography (C) and optical (D) images extracted from the boxed areas in A and B. Large contrast in the SRM optical signal corresponds to small domains ranging in height from 3 – 30 nm.

The topography image in **Fig. 6.14A** reveals semi-circular domains approximately 50 - 150 nm high. Formation of the domains and film morphology strongly depends on the resin-substrate affinity as well as the substrate surface properties. The corresponding SRM optical image (**Fig. 6.14B**) shows decreased scattering from these features. Close inspection, however, reveals much darker contrast arising from small particles with heights ranging from 3 – 30 nm. These particles are observed decorating the larger domains and isolated in the smooth regions between domains. These particles correspond to large decreases in intensity in the SRM optical contrast even though their height is modest. This is most clearly seen in the expanded regions shown in **Figs. 6.14C** and **D**. The measured particle heights of 9 nm is near

the expected globule size of the polymer particles (6 nm) and the large contrast observed in the SRM optical image is consistent with the low refractive index of the AF2400 polymer.[50]

The smallest measured lateral feature size in the SRM topography and optical images is approximately 300 nm. This provides a reasonable estimate of the SRM resolution using a 45 μm diameter resonator, given the anticipated size of the globular particles (6 nm) is much smaller than the SRM probe.[50] Having demonstrated the potential of SRM, we were interested in applying the technique to study systems with unknown and interesting optical properties.

6.3.5 Analysis of Graphene Oxide Thin Film

Interest in graphene, a single carbon monolayer, has existed over the last five decades due to predicted material properties.[40] Since it was fist isolated in 2004, majority of research has focused on investigating electrical properties of the material.[51] Conversely, optical properties of graphene are one of the material's most unexplored aspects.[40, 52] The little that has been investigated about graphene's optical properties includes inconsistent and variable results. The refractive index of graphene is highly debated with reported literature values ranging from 2.0 to 2.7 (@ 540 nm).[53-55] Optical properties between single and multiple sheets are highly variable, thus the reported discrepancy of material refractive index may be due to difficulties associated with measuring film height and optical properties. Current analysis techniques do not easily allow for the simultaneous determination of graphene height and refractive index. Using SRM, we can investigate both properties of graphene in order to better understand this 2-D material. Initial investigations for thin graphene oxide films on mica were completed.

Prior to analyzing graphene oxide thin films with SRM, samples were investigated using AFM. Graphene oxide solutions deposited at 0.1 mg/mL were found to have small features dispersed evenly throughout the film. Shown in **Fig. 6.15**, features approximately 200 nm wide and 2 nm tall were identified on the mica substrate. Graphene oxide films were determined to be stable as repeated imaging did not alter the feature. Additionally, there was little film to film variability of the graphene oxide features.

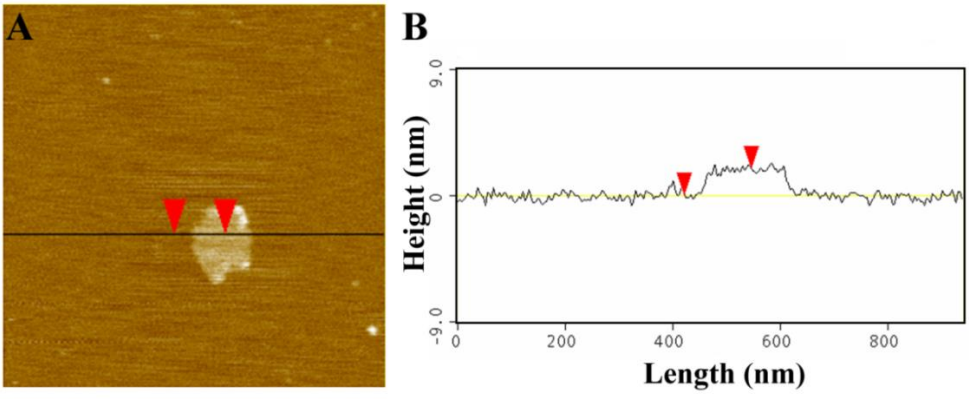

Figure 6.15. Atomic force microscopy (AFM) was used to characterize graphene oxide thin films on mica. (A) AFM image of 0.1 mg/mL graphene oxide spin cast on a mica substrate. (B) A small domain ~200 nm wide and ~2 nm tall is observed through topographic changes. AFM helped to characterize the graphene oxide thin films prior to analysis by SRM.

Once AFM confirmed the presence of small graphene features, we analyzed the thin film material using SRM. Spectral shifts were investigated using a barium titanate modified AFM probe on a clean mica substrate and a graphene oxide (0.1 mg/mL) coated mica substrate, **Fig. 6.16**. A red-shift was observed when analyzing the graphene oxide coated substrate, indicating an increase of surface refractive index due to the presence of the graphene oxide thin film (n ~ 2.0).

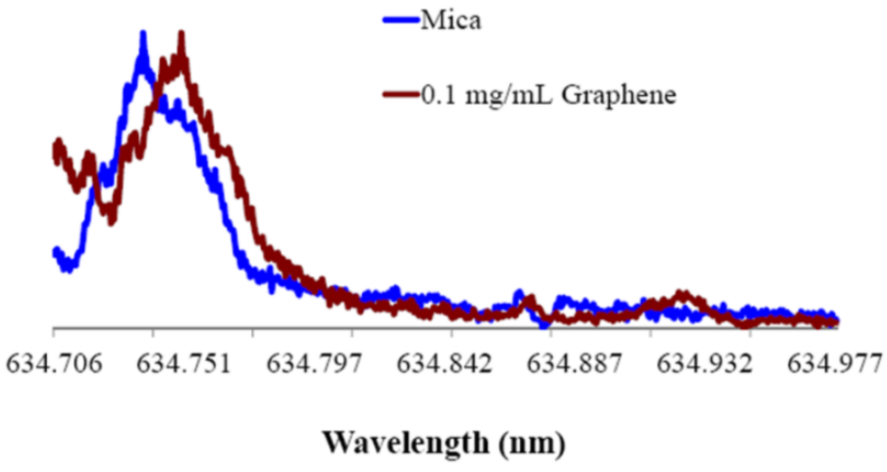

Figure 6.16. Spectral shifts of a barium titanate microsphere tip on a mica substrate (blue) and a 0.1 mg/mL graphene oxide thin film on mica (red). The spectral shift indicates a difference in optical properties between the two samples.

Having confirmed spectral shifts could be measured for a graphene oxide surface, we investigated the height and optical properties of thin films using SRM. **Figure 6.17** shows a SRM image of graphene oxide on mica. The topography image in **Fig. 6.17A** reveals features with similar sizes and distributions observed with AFM (**Fig. 6.15**). Impressively, the corresponding optical image in **Fig. 6.17B** reveals large optical contrast in the SRM signal corresponding to the small features. The optical contrast between the graphene oxide features and mica are expected due to differences in refractive index, ~2.0 and ~1.6 respectively.[53-56] Initial SRM imaging of graphene oxide thin films reveal the smallest measured lateral feature size is approximately 150-200 nm, a slight improvement to what was previously measured for Teflon AF thin polymer films, 300 nm.

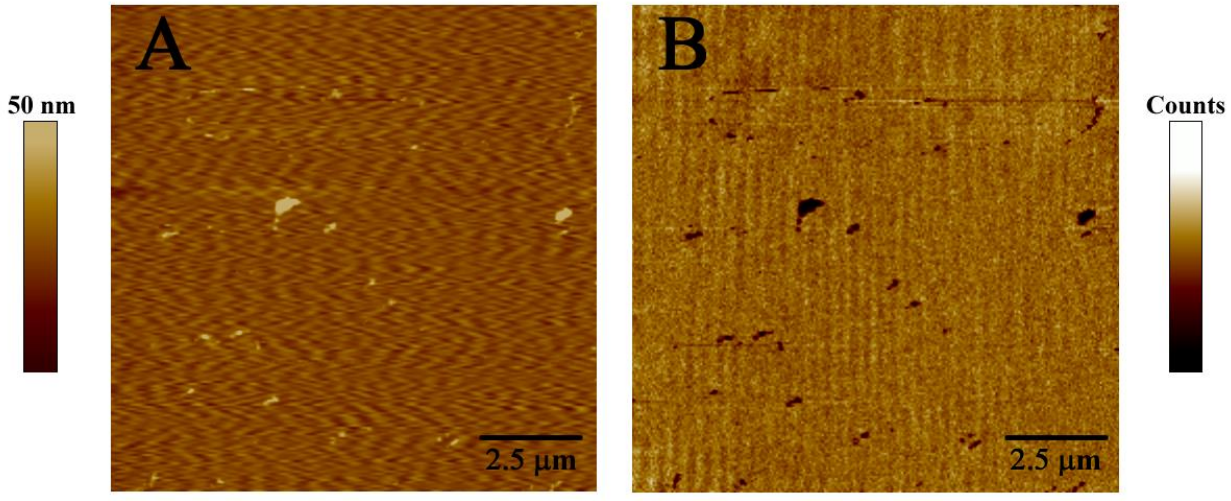

Figure 6.17. SRM images of 0.1 mg/mL graphene oxide on mica. (A) Topographic images reveal small domain features corresponding in size and dispersion to AFM images (**Fig. 6.15**). (B) Optical contrast is observed between the small graphene oxide features (n ~ 2.0) and the mica (n ~1.6) substrate.

Initial investigations reveal SRM imaging of graphene oxide with distinct optical contrast of graphene oxide features. Future investigations will focus on quantifying refractive index of graphene oxide features by calibrating the SRM tip response. Additionally, fabrication of graphene oxide thin films will be optimized to prepare samples of variable heights. Ultimately, we would like to utilize SRM for simultaneous measurements of graphene height and refractive index to better characterize optical properties of this unique 2-D material.

6.4 Future Directions

We have demonstrated the proof-of-concept of SRM for imaging a variety of surfaces. Moving forward, we are interested in expanding these capabilities to other sample types and further developing SRM as a novel analytical tool. In addition to using SRM as an imaging platform, we are interested in investigating the real time response of WGM resonators to probe particular sample areas. By positioning a SRM tip in a region of interest, changes over time can be monitored through the real-time response of

WGM resonant shifts. SRM is well suited for measuring changes over time due to the immobilized resonator probe which can be precisely placed in a region of interest. Furthermore, photobleaching is not a concern when detecting scatter from the SRM tip, which is desirable for monitoring changes over time.

Initial experiments of thin azobenzene polymer films suggest promising results for achieving dynamic measurements using the SRM technique. Ultimately, a scanning probe technique capable of analyzing dynamic sample changes would be an extremely valuable tool for material science as well as biological applications.

6.4.1 Azobenzene Polymers

Photochromic properties of azobenzene are of much interest due to the ability of the molecule to undergo *trans-cis* isomerization when irradiated with UV-visible light.[57] PE-DR 19, for example, has demonstrated large photoinduced index changes ($\Delta n = 0.3$ at 633 nm) due to photoisomerization of azobenzene side groups.[58] Light near or at the absorption peak of azobenzene (~320 nm or ~450 nm) causes the *trans* moieties to undergo a structural change to the *cis* formation, which has significantly different optical properties.[58] To investigate photoisomerization using SRM, PE-DR 19 thin films were prepared.

Samples of dilute PE-DR 19 solutions were spin cast on glass slides to produce clear, smooth surfaces. For spin coating, 10 μL of the polymer solution in chloroform, ~0.5 mg/mL, was pipetted onto a clean glass slide then rotated at ~5,000 rpm. Polymer refractive index changes were investigated by measuring WGM spectral shifts. To confirm reported optical properties of PE-DR 19 thin films, refractive index as a function of exposure time was measured. This was achieved by positioning a SRM tip above various samples to measure the optical properties of the thin films through the determination of the microsphere resonant wavelength. **Figure 6.18** shows as exposure time increased, the measured resonant wavelength decreased, thus, indicating the reduction of film refractive index. Saturation is

observed at high exposure levels. Importantly, these results show a similar trend as Shi, *et. al.* who investigated refractive index changes of PE-DR 19 thin films using ellipsometry.[58]

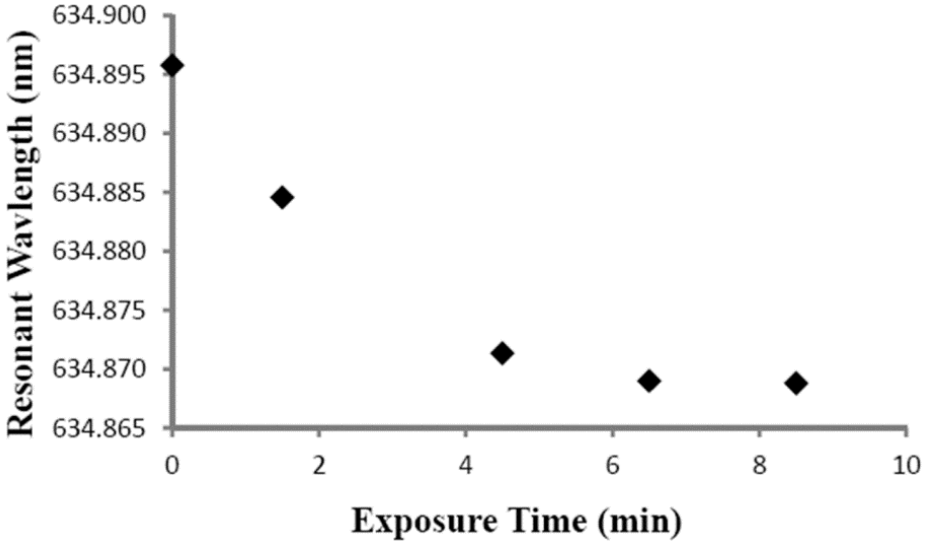

Figure 6.18. Refractive index of PE-DR 19 thin films as a function of exposure time measured using a SRM tip. At low exposure times, the film index decreases rapidly while high exposure leads to film index saturation. These results agree with ellipsometry measurements of PE-DR 19 thin films reported by Shi, *et. al.*[58]

To further probe the photoinduced bifringence of PE-DR19 films, SRM was used to investigate refractive index changes in real-time. For analysis, a PE-DR 19 thin film sample was placed on the Dove prism and the SRM tip was lowered to a particular region of the thin film surface to monitor WGM spectra over time. Continuous spectra were collected using NanoScope IIIa software. Interestingly, PE-DR19 thin films exhibited dynamic behavior of WGM resonances in response to UV light exposure, shown in **Fig. 6.19**. Prior to UV exposure, the measured WGM spectra was determined to be stable over time. At time 0, UV light was exposed to the thin film for approximately 2 min. Post UV exposure, the WGM resonance exhibited a large resonance shift to shorter wavelengths. Gradually, the WGM resonances are seen to shift back to longer wavelengths then stabilize near the original resonant wavelength after about 8 min.

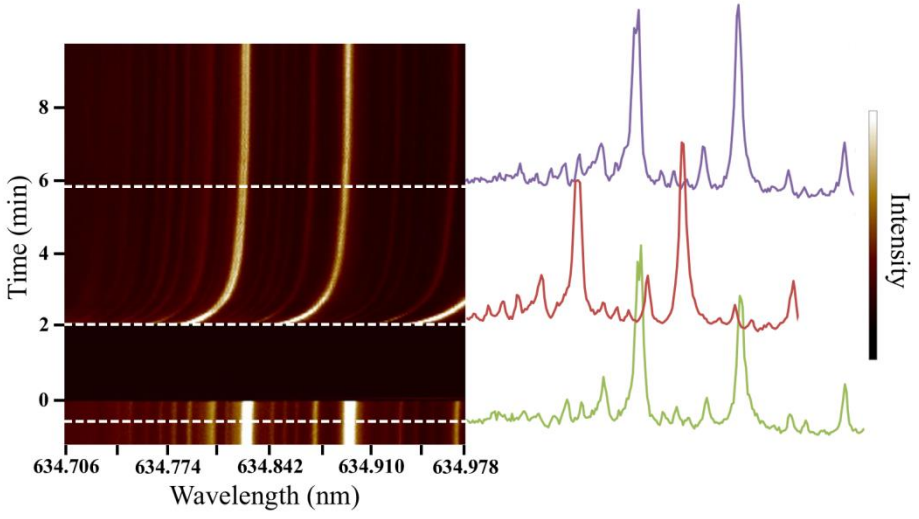

Figure 6.19. Observed dynamic behavior of WGM spectral shifts on PE-DR 19 thin films. For UV exposure, the APD was blocked while UV light was exposed to the sample for ~ 2 min.

This dynamic behavior exhibited by PE-DR 19 may be related to the photoisomerization of the polymer due to UV light exposure. Initial experiments reveal SRM as a promising analytical tool for real-time analysis of dynamic systems. The ability to monitor active sample changes provides a high-content tool to probe fundamental properties of materials. Furthermore, the technique can be applied to monitoring dynamic biological systems such as binding on surfaces.

6.5 Conclusions

Whispering gallery mode sensing is combined with AFM to simultaneously characterize refractive index and surface topography. The preliminary data shown validates SRM and illustrates the flexibility of the approach for characterizing patterned refractive index surfaces. The ability to map these changes with high spatial resolution provides a new, hyphenated tool for material characterization. Furthermore, imaging topography and optical properties of a sample is advantageous for improving understanding of thin polymer films as well as 2-D materials. In addition to achieving high spatial resolution, the SRM probe can be utilized to investigate dynamics with high time resolution. For material samples, this

provides an analytical tool to investigate transitional samples such as photosensitive materials. The capabilities of SRM are desirable for improving characterization and understanding of materials and, provide a valuable tool for investigating biological samples.

6.6 References

1. Cricenti, A., et al., Scanning Probe Microscopy in Material Science and Biology. *J. Phys. D: Appl. Phys.* **2011,** *44* (46), 1-23.
2. Raigoza, A. F., et al., Review: Recent Advances and Current Challenges in Scanning Probe Microscopy of Biomolecular Surfaces and Interfaces. *ACS Appl. Mater. Interfaces* **2013,** *5* (19), 9249-9261.
3. Binnig, G., et al., Atomic Force Microscope. *Phys. Rev. Lett.* **1986,** *56* (9), 930-933.
4. Shao, Z., et al., Biological Atomic Force Microscopy: What is Achieved and what is Needed. *Adv. Phys.* **1996,** *45* (1), 1-86.
5. Giessibl, F. J., Advances in Atomic Force Microscopy. *Rev. Mod. Phys.* **2003,** *75* (3), 949-983.
6. Eifert, A.; Kranz, C., Hyphenating Atomic Force Microscopy. *Anal. Chem.* **2014,** *86* (11), 5190-5200.
7. Flores, S. M.; Toca-Herrera, J. L., The New Future of Scanning Probe Microscopy: Combining Atomic Force Microscopy with Other Surface-Sensitive Techniques, Optical Microscopy and Fluorescence Techniques. *Nanoscale* **2009,** *1* (1), 40-49.
8. Barattin, R.; Voyer, N., Chemical Modifications of AFM Tips for the Study of Molecular Recognition Events. *Chem. Commun.* **2008,** (13), 1513-1532.
9. Frisbie, C. D., et al., Functional Group Imaging by Chemical Force Microscopy. *Science* **1994,** *265* (5181), 2071-2074.
10. Palacio, M. L. B., et al., Protein Conformation Changes on Block Copolymer Surfaces Detected by Antibody-Functionalized Atomic Force Microscope Tips. *J. Biomed. Mater. Res., Part A* **2012,** *100A* (1), 18-25.
11. Amemiya, S., et al., Scanning Electrochemical Microscopy. *Annu. Rev. Anal. Chem.* **2008,** *1*, 95-131.
12. Engstrom, R. C.; Pharr, C. M., Scanning Electrochemical Microscopy. *Anal. Chem.* **1989,** *61*, 1099A-1104A.
13. Derylo, M. A., et al., Parylene Insulated Probes for Scanning Electrochemical-Atomic Force Microscopy. *Langmuir* **2011,** *27*, 13925-13930.
14. Macpherson, J. V.; Unwin, P. R., Combined Scanning Electrochemical-Atomic Force Microscopy. *Anal. Chem.* **2000,** *72*, 276-285.
15. Kranz, C., Recent Advancements in Nanoelectrodes and Nanopipettes Used in Combined Scanning Electrochemical Microscopy Techniques. *Analyst* **2014,** *139* (2), 336-352.

16. Kranz, C., et al., Integrating an Ultramicroelectrode in an AFM Cantilever: Combined Technology for Enhanced Information. *Anal. Chem.* **2001,** *73*, 2491-2500.
17. Huang, K., et al., Probing Individual Redox PEGylated Gold Nanoparticles by Electrochemical-Atomic Force Microscopy. *ACS Nano* **2013,** *7* (5), 4151-4163.
18. Kueng, A., et al., Integrated AFM-SECM in Tapping Mode: Simultaneous Topographical and Electrochemical Imaging of Enzyme Activity. *Angew. Chem., Int. Ed. Engl.* **2003,** *42* (28), 3238-3240.
19. Schmid, T., et al., Nanoscale Chemical Imaging Using Tip-Enhanced Raman Spectroscopy: A Critical Review. *Angew. Chem., Int. Ed. Engl.* **2013,** *52* (23), 5940-5954.
20. Krug, J. T., II, et al., Design of Near-Field Optical Probes with Optimal Field Enhancement by Finite Difference Time Domain Electromagnetic Simulation. *J. Chem. Phys.* **2002,** *116*, 10895-10901.
21. Dunn, R. C., Near-Field Scanning Optical Microscopy. *Chem. Rev.* **1999,** *99* (10), 2891-2927.
22. Betzig, E.; Chichester, R. J., Single Molecules Observed by Near-Field Scanning Optical Microscopy. *Science* **1993,** *262* (5138), 1422-1425.
23. Hecht, B., et al., Facts and Artifacts in Near-Field Optical Microscopy. *J. Appl. Phys.* **1997,** *81* (6), 2492-2498.
24. Boehm, J., et al., Tuning the Refractive Index of Polymers for Polymer Waveguides Using Nanoscaled Ceramics or Organic Dyes. *Adv. Eng. Mater.* **2004,** *6* (1-2), 52-57.
25. Ma, H., et al., Polymer-Based Optical Waveguides: Materials, Processing, and Devices. *Adv. Mater.* **2002,** *14* (19), 1339-1365.
26. Flory, F.; Escoubas, L., Optical Properties of Nanostructured Thin Films. *Prog. Quantum Electron.* **2004,** *28*, 89-112.
27. Fan, X., et al., Sensitive Optical Biosensors for Unlabeled Targets: A Review. *Anal. Chim. Acta* **2008,** *620* (1-2), 8-26.
28. Tranchida, D., et al., Scanning Near-Field Ellipsometry Microscopy: Imaging Nanomaterials with Resolution Below the Diffraction Limit. *Nanoscale* **2011,** *3* (1), 233-239.
29. Servoli, E., et al., Quantitative Analysis of Protein Adsorption via Atomic Force Microscopy and Surface Plasmon Resonance. *Macromol. Biosci.* **2008,** *8* (12), 1126-1134.
30. Chen, X., et al., Degradation of a Thin Polymer Film Studied by Simultaneous in Situ Atomic Force Microscopy and Surface Plasmon Resonance Analysis. *J. Phys. Chem.* **1995,** *99*, 11537-11542.
31. Karageorgiev, P., et al., Scanning Near-Field Ellipsometric Microscope-Imaging Ellipsometry with a Lateral Resolution in Nanometer Range. *Appl. Phys. Lett.* **2001,** *79* (11), 1730-1732.

32. Stuart, J. K.; Hlady, V., Reflection Interference Contrast Microscopy Combined with Scanning Force Microscopy Verifies the Nature of Protein-Ligand Interaction Force Measurements. *Biophys. J.* **1999,** *76*, 500-508.
33. Amini, S., et al., Using the Atomic Force Microscope as a Nanomechanical Partner to Support Evanescent Field Imaging. *Eur. Phys. J.* **2014,** (223), 2023-2033.
34. Butt, H.-J., et al., Force Measurements with the Atomic Force Microscope: Technique, Interpretation and Applications. *Surf. Sci. Rep.* **2005,** *59* (1-6), 1-152.
35. Ghislain, L. P.; Elings, V. B., Near-Field Scanning Solid Immersion Microscope. *Appl. Phys. Lett.* **1998,** *72* (22), 2779-2781.
36. Vollmer, F.; Arnold, S., Whispering-Gallery-Mode Biosensing: Label-Free Detection Down to Single Molecules. *Nature Methods* **2008,** *5* (7), 591-596.
37. Vahala, K. J., Optical Microcavities. *Nature* **2003,** *424* (6950), 839-846.
38. Hanumegowda, N. M., et al., Refractometric Sensors Based on Microsphere Resonators. *Appl. Phys. Lett.* **2005,** *87* (20), 201107.
39. Ficner, S., et al., Refractive Indexes in Thick Photoresist Films as a Function of Bake Conditions and Film Exposure. *Proc. SPIE* **1997,** *3049*, 838-849.
40. Mas-Balleste, R., et al., 2D Materials: to Graphene and Beyond. *Nanoscale* **2011,** *3*, 20-30.
41. Geim, A. K., Graphene: Status and Prospects. *Condens. Matter* **2009**, 1-8.
42. Thouti, E., et al., Optical Properties of Silver Nanoparticles Integrated Graphene Oxide Thin Films on Glass and Silicon Substrates. *Plasmonics* **2015**, Ahead of Print.
43. Yang, B., et al., Direct Electrodeposition of Reduced Graphene Oxide on Carbon Fiber Electrode for Simultaneous Determination of Ascorbic Acid, Dopamine and Uric Acid. *Colloids Surf., A* **2014,** *456*, 146-152.
44. Yariv, A., Critical Coupling and its Control in Optical Waveguide-Ring Resonator Systems. *Ieee Photonics Technol. Lett.* **2002,** *14* (4), 483-485.
45. Mendes, L. A. V., et al., AZ-1518 Photoresist Analysis with Synchrotron Radiation Using High-Resolution Time-of-Flight Mass Spectrometry. *Polym. Degrad. Stab.* **2007,** *92* (6), 933-938.
46. Norwood, R. A.; Whitney, L. A., Rapid and Accurate Measurements of Photoresist Refractive Index Dispersion Using the Prism Coupling Method. *Proc. SPIE* **1996,** *2725*, 273-280.
47. Avila, L. F.; Lima, C. R. A., Dill's Parameter Measure in Liquid Photosensitive Materials via Interferometric Method. *Eur. Polym. J.* **2007,** *43* (5), 2041-2045.
48. Henderson, C. L., et al., Bleaching-Induced Changes in the Dispersion Curves of DNQ Photoresists. *Proc. SPIE* **1997,** *3049*, 585-595.
49. Lowry, J. H., et al., Optical Characteristics of Teflon AF Fluoroplastic Materials. *Opt. Eng.* **1992,** *31*, 1982-1985.

50. Gallyamov, M. O., et al., High-Quality Ultrathin Polymer Films Obtained by Deposition From Supercritical Carbon Dioxide as Imaged by Atomic Force Microscopy. *Langmuir* **2002,** *18*, 6928-6934.
51. Novoselov, K. S., et al., Electric Field Effect in Atomically Thin Carbon Films. *Science* **2004,** *306* (5696), 666-669.
52. Weber, J. W., et al., Optical Constants of Graphene Measured by Spectroscopic Ellipsometry. *Appl. Phys. Lett.* **2010,** *97*, 1-3.
53. Ni, Z. H., et al., Graphene Thickness Determination Using Reflection and Contrast Spectroscopy. *Nano Lett.* **2007,** *7*, 2758-2763.
54. Gray, A., et al., Optical Detection and Characterization of Graphene by Broadband Spectrophotometry. *J. Appl. Phys.* **2008,** *104* (5), 1-8.
55. Wang, X., et al., Strong Anomalous Optical Dispersion of Graphene: Complex Refractive Index Measured by Picometrology. *Opt. Express* **2008,** *16* (26), 22105-22112.
56. Bailey, A. I.; Kay, S. M., Measurement of Refractive Index and Dispersion of Mica, Employing Multiple-Beam Interference Techniques. *Br. J. Appl. Phys.* **1965,** *16* (1), 39-44.
57. Bandara, H. M. D.; Burdette, S. C., Photoisomerization in Different Classes of Azobenzene. *Chemical Society Reviews* **2012,** *41* (5), 1809-1825.
58. Shi, Y., et al., Large Stable Photoinduced Refractive Index Change in a Nonlinear Optical Polyester Polymer with Disperse Red Side Groups. *Appl. Phys. Lett.* **1991,** *58* (11), 1131-1133.

Chapter 7

Towards Investigating Biological Samples Using Scanning Resonator Microscopy

Portions of this chapter were previously published in ACS Photonics:
Wildgen, S.; Dunn, R. Scanning Resonator Microscopy: Integrating Atomic Force Microscopy and Whispering Gallery Mode Resonators. ACS Photonics. 2015, 2 (6) 699-706.

7.1 Introduction

We have demonstrated scanning resonator microscopy (SRM) as a powerful technique for analyzing material samples. In this chapter, we extend SRM analysis to biological samples as there is much interest in developing robust, label-free and high-resolution detection schemes for high-content analysis of native systems. Scanning resonator microscopy has the advantage of utilizing a single, unmodified resonator for the label-free detection of a variety of surfaces. Using a single resonator provides a means to overcome sphere-to-sphere variation while also reducing the chemistry and time required for microsphere surface modifications. In this chapter, we extend the application of SRM to the analysis of bio-surfaces such as protein microarrays, and model cellular membrane systems in order to develop improved label-free tools for biological investigations. Progress on development of SRM for biological samples as well as modifications for future instrument optimization are discussed.

7.1.1 Protein Microarrays

As discussed in previous chapters, common diagnostic strategies rely on quantifying protein biomarkers in bodily fluids such as blood, serum, or urine. Analytical tools developed to help these efforts include microarrays which can be utilized for high-content analysis of proteins in small sample volumes. These miniaturized systems rely on precise microspot patterns on solid supports for the parallel analysis of tens to thousands of proteins.[1, 2]

Fabrication of high-density protein microarrays allow for capture molecules to be printed directly onto a substrate. Using conventional methods, such as photolithography or ink jet printing, a spot size resolution of ~100 μm is routinely achieved.[3, 4] With the development of soft lithography techniques, such as microstamping, spot size resolution of high-density arrays is improving. Hoff, *et. al.* reported nanoscale protein microarrays with a resolution of approximately 75 nm.[5] On-chip detection schemes for high-density protein microarrays rely on fluorescent or chemiluminescencent signals. Due to rinsing and incubation steps, these readout methods increase time and reagents required. Furthermore, the colorimetric signals limit the window of time for quantitative analysis. To overcome these limitations, label-free measurements with sensitive detection capabilities are advantageous for the analysis of protein microarrays. With the numerous advantages of label-free techniques, several label-free schemes have been utilized to analyze protein microarrays including SPR imaging, ellipsometry, and interferometry.[6] We propose to utilize SRM as a sensitive label-free detection scheme for protein microarrays.

Using SRM, label-free detection of microarray surface binding events can be achieved and quantified based on imaging refractive index contrast. The hyphenated scanning probe technique allows for multiple protein microspots to be quantified using a single, unmodified resonator which avoids variable sensor performance due to sensitivity and Q-factor differences between resonators.

7.1.2 Model Membranes for the Investigation of Membrane Structure and Organization

Another biological system we are interested in analyzing by SRM are supported lipid monolayers which provide a model system for studying cellular membrane components. Monitoring cellular membranes is important for evaluating human health. Information about the location, behavior, and amount of certain components provides valuable indicators of early disease states. In particular, cholesterol has been shown to be vital for regulating the physical and biological properties of the mammalian cellular membrane.[7] More than 90% of cellular cholesterol is located within the plasma membrane, thus, for decades, there has been interest in studying its distribution and location which could provide insight on understating indicators of disease.[8] An approach to study cholesterol behavior in cellular membranes relies on modified cholesterol derivatives.

Fluorescent sterol probes are commonly used to study the behavior of cholesterol within lipid monolayers, however, their modified structures may alter the native packing and distributions of cholesterol within the cellular environment. Furthermore, for analytical measurements, certain fluorescent probes suffer from poor optical properties, low quantum yields, and photobleaching. Analog probes with structure and behavior that accurately mimics that of native cholesterol are necessary to improve understanding of cholesterol within lipid membranes.

Fluorinated sterol derivatives provide an alternative probe with less bulky structural modifications. Cholesterol derivatives with atomic fluorine substitutions have been demonstrated to retain domain formation and behavior similar to native cholesterol.[9, 10] Commonly, these fluorinated probes are used for solid state NMR analysis of model bilayer systems. Alternatively, SRM provides a method to image the fluorinated probe through optical contrast between fluorine and surrounding membrane phospholipids. In this chapter, we investigate the potential of SRM as an analytical tool for measuring fluorinated cholesterol in model membrane systems. Sensing fluorinated cholesterol within monolayers would be advantageous for the non-destructive imaging of model membranes in order to better understand the native behavior and role of cholesterol.

Initial SRM results are presented for analysis of bio-surfaces and supported lipid monolayers. With straightforward modifications to the SRM instrument, we believe we can further extend label-free measurements for non-invasive, label-free analysis of whole cell assays.

7.2 Materials and Methods

7.2.1 Materials

Bovine serum albumin-biotin (BSA-biotin), BSA-Alexa 488, streptavidin and SuperBlock (PBS) Blocking Buffer were obtained from Thermo Scientific (Waltham, MA). Sphingomyelin (>99%), and heptafluoro cholesterol (F7-cholesterol; >99%) were obtained from Avanti Polar Lipids (Alabaster, AL). 10x phosphate buffered saline (PBS) (27 mM KCl; 15 mM KH_2PO_4; 1400 mM NaCl; 81 mM Na_2HPO_4) were obtained from MP Biomedicals. Prior to use, 1x PBS solutions were prepared with 0.05% sodium azide (pH 7.35). Glass microscope slides were obtained from Fisher Scientific (Hampton, NH) and were pirhana (70:30 H_2SO_4:H_2O_2) cleaned prior to use. Pirhana solution is extremely dangerous and should only be used in a properly vented hood using appropriate attire and precautions. All other reagents, unless otherwise noted, were purchased from Fisher Scientific (Hampton, NH) and used without further purification.

7.2.2 Protein Coated Surfaces

Pirhana cleaned microscope slides were subsequently rinsed with de-ionized water, ethanol, and toluene. The slides were reacted in 5% (3-aminopropyl)triethoxysilane (APTES) / toluene for approximately 2 hours, rinsed in toluene, ethanol, and finally PBS. The functionalized slides were incubated in 5% gluteraldehyde in PBS for 1 hour. Aldehydes on the surface were reacted with bovine serum albumin (BSA)-biotin which was then incubated with streptavidin. Scanning resonator microscopy experiments comparing bare glass slides with protein coated surfaces were carried out in PBS at room temperature.

7.2.3 Sphingomyelin and Cholesterol Monolayers

Stock solutions of sphingomyelin (25 mg/mL) and fluorinated cholesterol (4 mg/mL) were prepared in chloroform. To prepare Langmuir Blodgett (LB) monolayers, sphingomyelin stock solution was diluted and the desired amount of fluorinated cholesterol was added (3 mol %). For fluorescent imaging, the solutions were doped with ~10^{-4} mol % $DilC_{18}$ reporter dye. Monolayers were dispersed onto a subphase of ultra-pure water (18 MΩcm) in a Langmuir-Blodgett trough (Type 611, Nima Technology, Coventry, England). Once dispersed at the air-water interface, the chloroform was allowed to evaporate for 15 minutes. Compression and expansion cycles were repeated twice to anneal the monolayer. Lipids were compressed and held at the target pressure 8 mN/m for 10 minutes. Monolayers were deposited on clean microscope slides at a deposition rate of 8 mm/min. The supported monolayer samples were analyzed at room temperature in air and water.

7.3 Results and Discussion

7.3.1 Investigations of Protein Coated Surfaces

Protein microarrays are emerging as promising analytical tools due to their high-density arrays of numerous analytes. Scanning resonator microscopy provides a novel detection scheme for imaging protein patterned surfaces. A single, unmodified resonator can be used to quantify surface protein binding events through measured optical contrast. This provides a low cost, high resolution and robust detection scheme for protein microarrays. In order to validate the ability of SRM to characterize protein surfaces, WGM spectral shifts were investigated.

Preliminary experiments were completed to explore the usefulness of SRM for characterizing binding at surfaces. Whispering gallery mode spectra of a SRM tip in phosphate buffered saline (PBS) on a bare glass substrate were compared with that taken on a glass surface coated with protein. For the protein surface, bovine serum albumin (BSA)-biotin was covalently attached to a glass slide, which was then

incubated with streptavidin in PBS. Shown in **Fig. 7.1**, a resonant wavelength shift is measured by a single SRM tip used to analyze the protein and glass sample surfaces.

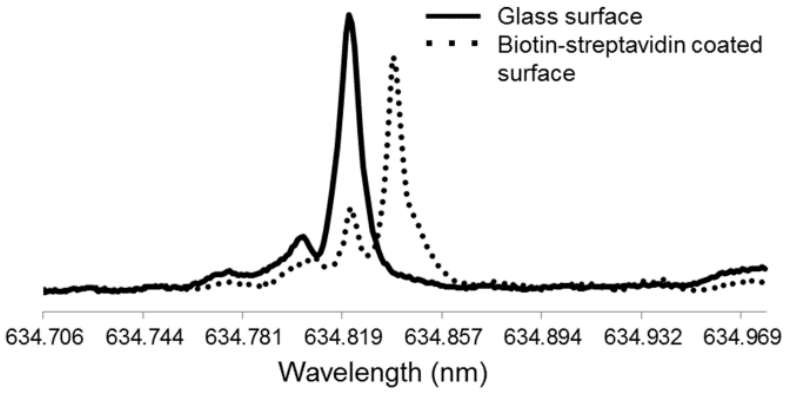

Figure 7.1. Example of reversible shifts in the WGM resonance of a microresonator tip held in contact-mode feedback on a bare glass surface versus a biotin-streptavidin coated surface. Measurements were taken in PBS at room temperature.

Red shifts in the measured WGM resonance are observed on the protein coated surface, consistent with the presence of the biotin-streptavidin complex. The reversibility of the shift was confirmed by repeating the spectral measurement of the resonator on the bare glass substrate. WGM resonators are routinely used in label-free sensing applications and the results shown in **Fig. 7.1** suggest that similar approaches can now be used to monitor binding at surfaces. Advantages of this include the ability to use the same resonator to monitor binding of multiple analytes at various sites, thus alleviating issues in calibration and varying resonator Q-factors. This also demonstrates SRM as a quantitative approach for monitoring binding at high-density surface arrays that does not require the introduction of labels. Importantly, to be applied to protein microarrays, SRM needs to be able to image patterned protein surfaces.

Microstamping, a soft lithography technique, was used to prepare patterned monolayers of fluorescently labeled bovine serum albumin (BSA-A488) on a glass surface. In this technique, an elastomer (PDMS) mold was incubated with proteins and applied with pressure to a glass substrate.[1, 11]

Fluorescence imaging confirmed the patterned attachment of BSA-A488 on the glass surface. SRM was used to image the patterned feature however, no successful images were achieved. Post SRM analysis, fluorescence imaging revealed the microsphere probe had perturbed the BSA-A488 surface, most likely due to probe-sample forces. For more stable patterned monolayers, surface modifications, such as covalent attachment, should be investigated. Future studies are underway to optimize microspot fabrication methods. In addition to protein surfaces, we were interested in analyzing model membrane systems using SRM.

7.3.2 Investigation of Fluorinated Cholesterol as a Probe for Membrane Organization

Cellular membranes play an essential role for a range of biological functions. Cholesterol, a main component of cellular membranes, is an important regulator of lipid membrane organization. Characterizing the specific role and behavior of cholesterol within membranes allows for a better understanding of the contribution and role of membranes in a variety of diseases.[7] Being that this goal has existed for several decades, numerous cholesterol probes have been developed and implemented in membrane studies. A popular method to investigate cholesterol distribution relies on imaging fluorescent cholesterol probes.[12] These probes consist of modified cholesterol molecules for the incorporation of a fluorescent dye molecule. Due to the bulky nature of the conjugated ring systems, many fluorescently labeled probes poorly mimic native molecule behavior. We were interested in utilizing an analog with behavior similar to native cholesterol for accurate studies of membrane systems.

Alternative probes include fluorinated cholesterol molecules. These analogs differ only slightly from native cholesterol structure by atomic substitutions of fluorine in place of hydrogen. Importantly, fluorine substitutions decrease the dielectric constant of a molecule.[13, 14] Due to the relatively minor deviations from cholesterol's native structure, fluorinated cholesterol probes are desirable analytical tools for studying cellular membranes. Initially, fluorinated probes were developed for solid state F^{19} NMR studies for the determination of orientation within model bilayer systems.[10, 15, 16] Through NMR investigations, fluorinated probes have been determined to maintain the domain forming activity similar to that of native

cholesterol in sphingomyelin bilayers.[9] By using SRM imaging, we can detect fluorinated probes due to their optical contrast providing a novel tool for the investigation of model membrane systems. **Figure 7.2** shows the structure of heptafluoro cholesterol, a particular cholesterol probe, and sphingomyelin which were both used in initial investigations.

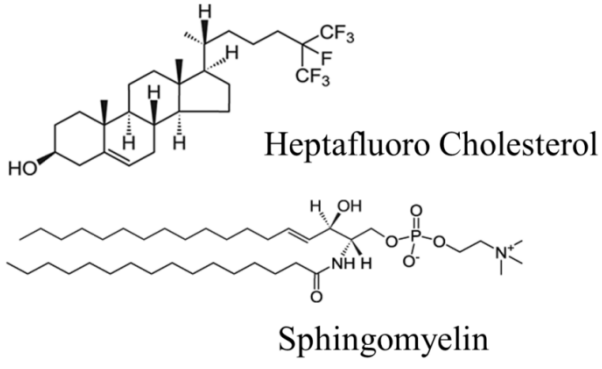

Figure 7.2. Structures of the heptafluoro cholesterol and sphimgomyelin which were used for the preparation of LB monolayers. For SRM imaging, the fluorinated cholesterol helped to increase the optical contrast between the sterol and lipid molecules.

Cholesterol, a rigid molecule, consists of a series of fused rings, a polar head group and a non-polar tail. Lipid monolayers with cholesterol rich domains were prepared at 3 mol % heptafluoro cholesterol in sphingomyelin and deposited onto glass substrates at 8 mN/m.[17] For fluorescence imaging, $DilC_{18}$ reporter dye was incorporated in the monolayer. **Figure 7.3** shows a typical fluorescence image of the prepared LB sphingomyelin monolayer doped with 3 mol % fluorinated cholesterol in air. Based on previous studies of the monolayer system, the dark, branched features approximately 10 μm in diameter indicate the cholesterol rich domains.[17]

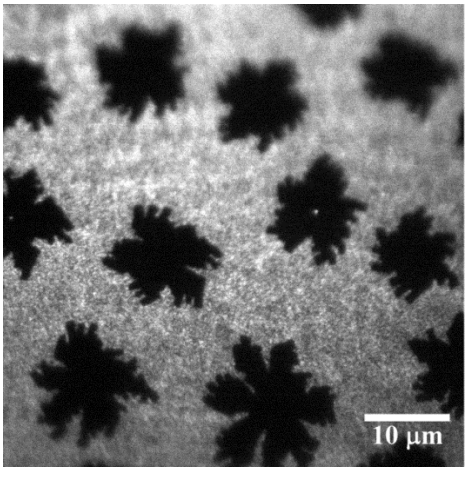

Figure 7.3. Fluorescence image of sphingomyelin with 3 mol% heptafluoro cholesterol deposited at 8 mN/m. $DilC_{18}$ was doped into the lipid solutions (10^{-4} mol%) as a reporter dye. Image was collected at room temperature in air.

To determine the exact location of the fluorinated cholesterol probe, SRM imaging was used. Due to the presences of seven fluorine atoms on the cholesterol tail group, the molecule will have a lower refractive index than surrounding hydrocarbon lipids.[13, 14] Orientation of the cholesterol probe within the supported model membrane allowed for direct analysis of the fluorine modified tail group by SRM. By using a SRM tip, the location of fluorinated molecule within the monolayer can be imaged through optical contrast. **Figure 7.4** shows the simultaneous topography and optical images collected for a sphingomyelin/fluorinated cholesterol LB film in water. Small and large circular features with corresponding height and optical contrast were observed.

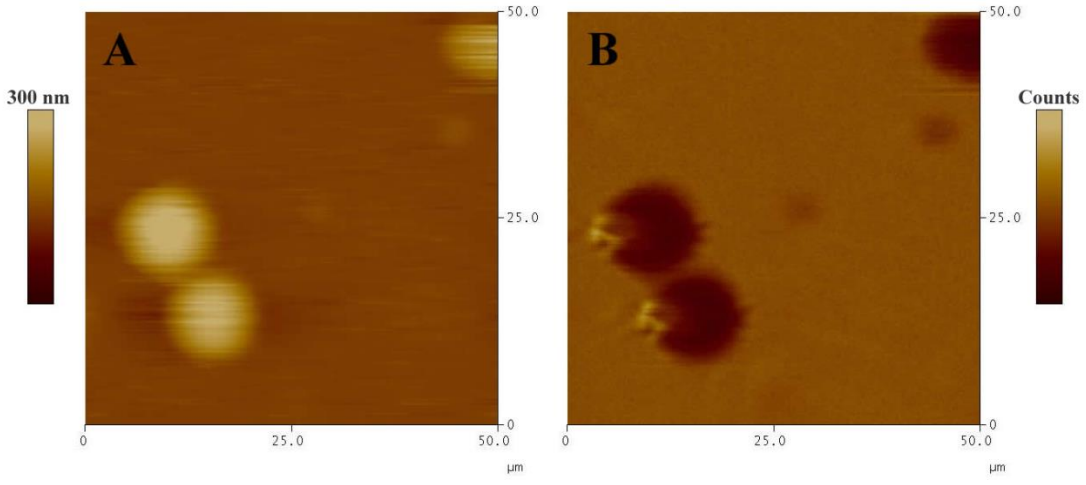

Figure 7.4. SRM analysis of sphingomyelin with 3 mol % fluorinated cholesterol monolayer in water. (A) Topography images reveal circular spots corresponding to large height changes, ~200 nm as well as smaller features around ~30 nm tall. (B) Similar features were observed in the optical imaged.

Upon further analysis, the feature heights in **Fig. 7.4A** did not correspond to the expected monolayer topography. In **Fig. 7.4A**, the bright features correspond to ~200 nm heights, while the dimmer spots correspond to ~30 nm heights. These measured heights are orders of magnitude larger than what is expected for a monolayer, ~1-2 nm. To understand what was occurring, fluorescence images of LB films in water were collected. Shown in **Fig. 7.5**, the monolayer in water has different features than previously observed (**Fig. 7.3**). Fluorescence images reveal reorganization of the lipid monolayer under aqueous conditions.

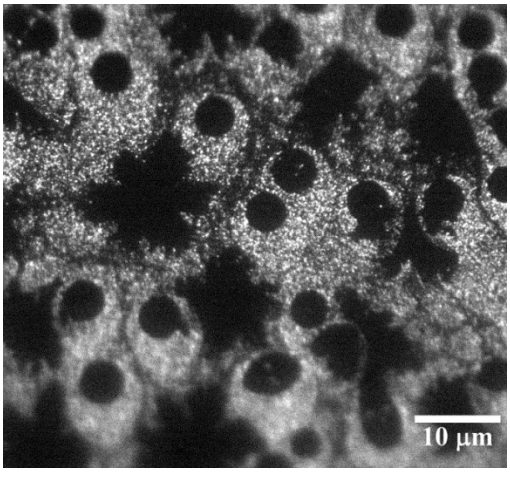

Figure 7.5. Fluorescence image of sphingomyelin with 3 mol% heptafluoro cholesterol deposited at 8 mN/m. $DilC_{18}$ was doped into the lipid solutions (10^{-4} mol%) as a reporter dye. Image was collected at room temperature in water.

Although no longer an accurate mimic of a cellular membrane, **Fig. 7.5** reveals circular features similar to the measured SRM images. The large feature heights might be a result of lipid reorganization due to hydration effects. Due to observed reorganization, the model system was determined to be unstable under aqueous conditions. When deposited on glass, lipid polar head groups interact with the substrate, exposing the hydrophobic tails to the environment. Therefore, when introduced to water, the monolayer becomes unstable resulting in reorganization or collapse of the monolayer system. In future work, bilayer systems will be used to address stability issues. Stable bilayer systems using vesicle formation or Langmuir-Blodgett/ Langmuir Shaffer deposition methods will be investigated.

Scanning resonator microscopy was demonstrated as a promising analytical tool for the investigation of model membrane systems. In addition to utilizing a cholesterol probe which exhibits native behavior, the label-free approach overcomes limitations of fluorescent based probes as photobleaching is not a concern.

7.4 Future Directions

In this chapter we have presented initial results and demonstrated the potential of SRM for the analysis of a variety of biological sample types including protein microarrays and model membranes. SRM provides a novel analytical tool for improved detection capabilities which we hope to apply to high-content analysis of cellular systems. There is much interest in determining optical properties of tissues and cells for the improvement of diagnostic as well as drug discovery screening assays.[18-22] Furthermore, straightforward modifications can be made to the SRM instrument design in order to increase sample types and applicability.

7.4.1 Cell-Based Assays

At the cellular level, non-invasive and real-time measurements are advantageous for basic research as well as applied studies. Label-free optical analysis of live cells has been demonstrated as a promising technique for determining cellular disease states as well as for improving pharmaceutical analysis.[18-20] Cell-based assays are an important component of the pre-clinical drug discovery process.[21] Label-free cellular assays provide a non-invasive measurement of live cells which does not require over-expression of protein. This provides a native cellular environment for drug development studies. Furthermore, label-free techniques are desirable for real-time analysis of dynamic cell systems.

Tissue and cell-based assays have also been demonstrated as promising clinical diagnostic tools.[22] Studies have indicated cancerous cells have a refractive index of 1.39 to 1.40, while the refractive index of normal cells is 1.35 to 1.37.[23, 24] Importantly, initial SRM detection limits ~10^{-2}-10^{-3} RIU demonstrate the ability of the technique to distinguish between healthy and diseased cells.[25] Furthermore, Puricelli, *et. al.* have recently demonstrated the ability of colloidal probes to analyze topographic and mechanical properties of living PC12 cells.[20] Their work demonstrates the ability to probe live cells using a modified SRM tip. Given the optical contrast of live versus diseased cells, we believe SRM is a promising technique to apply for label-free analysis and quantification of cellular disease states.

Scanning resonator microscopy is well suited to meet the desired label-free cell-based assay needs in a single platform. As a non-invasive, label-free platform SRM has high-temporal resolution capabilities as well as high-spatial resolution. Initial investigations of materials and biological samples demonstrate impressive surface sensitivities which are more than enough to distinguish reported optical contrast of these biological systems. Furthermore, modifications of the SRM instrumentation can improve sensing capabilities and performance.

7.4.2 Fiber Microsphere Resonators for Improved Sensing Capabilities

As discussed in Chapter 5, fiber microspheres have the advantage of achieving high Q-factors in air. Furthermore, in solution the fiber spheres showed a large improvement in solution refractive index sensitivity compared to commercially available barium titantate microspheres. We are interested in applying high sensitivity fiber resonators to measuring surface refractive index changes.

To determine substrate sensitivities, fiber microsphere resonators were analyzed in air using different refractive index substrates. The high Q's of the fiber microspheres in air allowed for small spectral shifts to be easily resolved, as shown in **Fig. 7.6**. The particular resonator analyzed in **Fig. 7.6** had a Q-factor of 5×10^6 and a measured sensitivity 0.16 nm/substrate RIU.

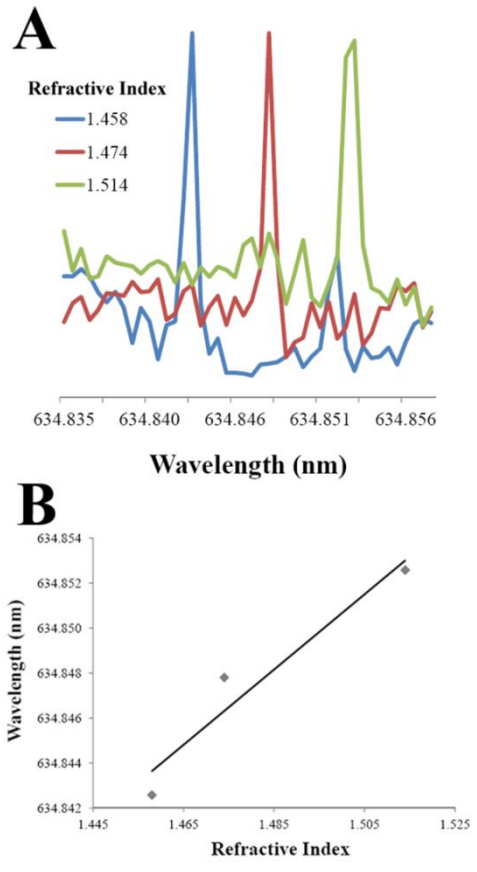

Figure 7.6. Substrate refractive index calibration of a fiber microsphere in air. (A) Spectral shifts indicate the resonant wavelength shifts to longer wavelengths with substrates increasing in refractive index. (B) The linear calibration (R^2 = 0.930) shows a measured sensitivity of 0.16 nm/ solution RIU.

Moving forward, fiber microspheres can be integrated in WGM sensing platforms, including SRM. The low throughput of fiber microsphere functionalization means it is not advantageous for biosensing platforms which require a high number of microspheres. However, SRM relies on a single, sensitive microsphere probe. The high Q-factors and sensitivity to substrate refractive index changes of the fiber microsphere resonators are desirable performance metrics for improving SRM optical imaging capabilities. Future work to integrate fiber microsphere resonators with SRM instrumentation will be completed in order to optimize SRM performance. Additional adjustments can be made to optimize SRM instrumentation.

7.4.3 Further Optimization of Scanning Resonator Microscopy

The surface refractive index sensing capabilities of SRM are far from optimized, with literature WGM applications reporting 10^{-7} RIU sensitivity.[26] Going forward, straightforward modifications to the SRM probe, coupler and data acquisition can easily increase the performance metrics of SRM.

SRM tip modifications are key for improving surface sensing capabilities. The high-Q fiber microspheres show promise for improved surface sensitivity. Increased surface sensitivity would improve SRM imaging resolution. The integration of fiber microspheres with AFM cantilevers is not trivial and will require creative modifications however, modifications could have a great impact on the SRM performance metrics. Fastening microspheres to tipless AFM cantilevers, moreover, will enable smaller resonators to be attached, thus increasing spatial resolution. Losses in the resonator cavity eventually limit the ultimate diameter possible, but resonators microns in diameter can still support WGMs.[27, 28]

Integrating an evanescent coupler that rides with the resonator tip will enable measurements on opaque samples and samples with large topography changes. This would also completely decouple the topography and optical signals and enable the coupler/resonator gap to be tuned towards the critical coupling condition, where resonator Q is maximized.[29]

To further improve imaging sensitivity, phase sensitive detection will be incorporated for the detection of WGM shifts. Using a lock-in amplifier, our group has demonstrated a two-fold improvement in refractive index sensitivity and detection limits around 10^{-6}-10^{-7} RIU (unpublished data). Integrating phase sensitive detection allows for accurate spectral shifts to be quantified at each image pixel. Modifications to the probe, coupler and data acquisition will increase the sensitivity and flexibility of the SRM approach, which opens new opportunities for characterizing a variety of surfaces and materials.

7.5 Conclusions

Scanning resonator microscopy is a promising analytical tool for interrogating biological samples. Initial results indicate the ability of a SRM tip to identify a protein modified surface even though the sample interaction area is greatly reduced compared to tradition WGM biosensing schemes. With further development, SRM can be utilized for label-free analysis of protein microarrays. Furthermore, we have demonstrated initial results of SRM imaging fluorinated cholesterol probes in model membrane systems. Fluorinated probes minimize system alterations and more accurately mimic cholesterol distribution than fluorescent probes. Because fluorine reduces the refractive index of the molecule, SRM can be used to map the location and distribution of cholesterol probes. Applying SRM to model membranes provides a new analytical tool for investigating the behavior and function of cellular membranes. Overall, SRM holds much potential for biological applications.

7.6 Summary

We are interested in developing label-free sensing schemes utilizing WMG optical resonators. The high sensitivity and compact size of glass microsphere resonators provide flexibility in the design and implementation of novel analytical assays and instrumentation. The development of new analytical tools is important for addressing needs in early detection and disease diagnostics.

In Chapters 3 and 4, we discuss the development of WGM fluorescence imaging approach for improved biosensing capabilities. For multiplexed detection, three putative ovarian cancer biomarkers were detected simultaneously by using different sphere sizes to target proteins of interest. This label-free approach for multiplexed sensing holds great promise for improving clinical diagnostic capabilities. Imaging multiple resonators in a single assay allows for high-content analysis. Hundreds of microspheres can be easily incorporated in small volume droplets, thus extending the application of WGM resonators as detectors in sample-limited applications. Within these small volume systems, real-time measurements of protein binding provide rapid analysis platforms for miniaturized analytical systems. The small size and

label-free detection capabilities allow resonators to be integrated as detectors in a variety of miniaturized analytical platforms and tools, such as digital microfluidic systems and protein microarrays.

In Chapters 6 and 7 we developed SRM as a promising new tool for analyzing both material and biological samples. By immobilizing a single resonator on an AFM tip, we have developed a hyphenated scanning probe technique. The techniques ability to simultaneously measure optical and topographic properties of a sample is extremely advantageous for investigating new materials and for probing biological samples. SRM was used to image thin polymer films with interesting optical properties including AZ 1518 and Teflon AF. SRM can be applied for non-invasive photonic investigations of biological samples including high-density protein microarrays and cell-based assays. The label-free approach and scanning capabilities could be easily applied to imaging biologic systems, while the high sensitivity of the resonators provides quantitative analysis capabilities. SRM results obtained to date have been achieved with instrumentation in its initial development phase. Modifications of the system would improve refractive index sensitivity, simplify WGM excitation, and increase imaging resolution. Overall, we have developed a variety of analytical techniques based on WGM sensing using small, glass optical microcavities. Platforms presented provide label-free, sensitive, and high-content advantages for sensing and biosensing applications.

7.7 References

1. Truskett, V. N.; Watts, M. P. C., Trends in Imprint Lithography for Biological Applications. *Trends Biotechnol.* **2006,** *24*, 312-317.
2. Chang, T.-Y., et al., Large-Scale Plasmonic Microarrays for Label-Free High-Throughput Screening. *Lab Chip* **2011,** *11* (21), 3596-3602.
3. Tsarfati-BarAd, I., et al., Miniaturized Protein Arrays: Model and Experiment. *Biosens. Bioelectron.* **2011,** *26* (9), 3774-3781.
4. Goudar, V. S., et al., Photoresist Functionalisation Method for High-Density Protein Microarrays Using Photolithography. *Micro Nano Lett.* **2012,** *7* (6), 549-553.
5. Hoff, J. D., et al., Nanoscale Protein Patterning by Imprint Lithography. *Nano Lett.* **2004,** *4* (5), 853-857.
6. Ray, S., et al., Label-Free Detection Techniques for Protein Microarrays: Prospects, Merits and Challenges. *Proteomics* **2010,** *10* (4), 731-748.
7. Maxfield, F. R.; Tabas, I., Role of Cholesterol and Lipid Organization in Disease. *Nature* **2005,** *438* (7068), 612-621.
8. Goluszko, P.; Nowicki, B., Membrane Cholesterol: A Crucial Molecule Affecting Interactions of Microbial Pathogens with Mammalian Cells. *Infect. Immun.* **2005,** *73* (12), 7791-7796.
9. Matsumori, N., et al., Fluorinated Cholesterol Retains Domain-Forming Activity in Sphingomyelin Bilayers. *Chem. Phys. Lipids* **2011,** *164* (5), 401-408.
10. Kauffman, J. M., et al., Fluorocholesterols, in Contrast to Hydroxycholesterols, Exhibit Interfacial Properties Similar to Cholesterol. *J. Lipid Res.* **2000,** *41* (6), 991-1003.
11. Kane, R. S., et al., Patterning Proteins and Cells Using Soft Lithography. *Biomaterials* **1999,** *20* (23/24), 2363-2376.
12. Maxfield, F. R.; Wustner, D., Analysis of Cholesterol Trafficking with Fluorescent Probes. *Methods Cell Biol.* **2012,** *108* (Lipids), 367-393.
13. Hougham, G., et al., Influence of Free Volume Change on the Relative Permittivity and Refractive Index in Fluoropolyimides. *Macromolecules* **1996,** *29* (10), 3453-6.
14. Hougham, G., et al., Polarization Effects of Fluorine on the Relative Permittivity in Polyimides. *Macromolecules* **1994,** *27* (21), 5964-71.
15. Ulrich, A. S., Solid State 19F NMR Methods for Studying Biomembranes. *Prog. Nucl. Magn. Reson. Spectrosc.* **2005,** *46* (1), 1-21.
16. Matsumori, N., et al., Orientation of Fluorinated Cholesterol in Lipid Bilayers Analyzed by 19F Tensor Calculation and Solid-State NMR. *J. Am. Chem. Soc.* **2008,** *130* (14), 4757-4766.

17. DeWitt, B. N.; Dunn, R. C., Interaction of Cholesterol in Ternary Lipid Mixtures Investigated Using Single-Molecule Fluorescence. *Langmuir* **2015,** *31* (3), 995-1004.
18. Yanase, Y., et al., Surface Plasmon Resonance for Cell-Based Clinical Diagnosis. *Sensors* **2014,** *14* (3), 4948-4959.
19. Mejard, R., et al., Optical Biosensing for Label-Free Cellular Studies. *TrAC, Trends Anal. Chem.* **2014,** *53*, 178-186.
20. Puricelli, L., et al., Nanomechanical and Topographical Imaging of Living Cells by Atomic Force Microscopy with Colloidal Probes. *Rev Sci Instrum* **2015,** *86*, 033705.
21. Xi, B., et al., The Application of Cell-Based Label-Free Technology in Drug Discovery. *Biotechnol. J.* **2008,** *3* (4), 484-495.
22. Wang, Z., et al., Tissue Refractive Index as Marker of Disease. *J Biomed Opt* **2011,** *16* (11), 116017.
23. Yanase, Y., et al., Detection of Refractive Index Changes in Individual Living Cells by Means of Surface Plasmon Resonance Imaging. *Biosens. Bioelectron.* **2010,** *26* (2), 674-681.
24. Liang, X. J., et al., Determining Refractive Index of Single Living Cell Using an Integrated Microchip. *Sens. Actuators, A* **2007,** *133* (2), 349-354.
25. Wildgen, S. M.; Dunn, R. C., Scanning Resonator Microscopy: Integrating Whispering Gallery Mode Sensing with Atomic Force Microscopy. *ACS Photonics* **2015,** *2* (6), 699-706.
26. Hanumegowda, N. M., et al., Refractometric Sensors Based on Microsphere Resonators. *Appl. Phys. Lett.* **2005,** *87* (20), 201107.
27. Quan, H.; Guo, Z., Analyses of Whispering-Gallery Modes in Small Resonators. *Journal of Micro/Nanolithography, MEMS and MOEMS* **2009,** *8* (3), 033060-7.
28. Guo, Z., et al., Near-Field Gap Effects on Small Microcavity Whispering-Gallery Mode Resonators. *J. Phys. D: Appl. Phys.* **2006,** *39*, 5133-5136.
29. Yariv, A., Critical Coupling and its Control in Optical Waveguide-Ring Resonator Systems. *Ieee Photonics Technol. Lett.* **2002,** *14* (4), 483-485.

Chapter 8

Appendix: Chemistry Functionalization, Data Analysis, and Instrumentation

This appendix section is written as a guide for current and future lab members with tips and tricks included for reference. This section includes step-by-step instructions and guidelines for surface functionalization of barium titanate microspheres and data analysis procedures including determining resonant wavelength values and processing results of numerous microspheres in each assay.

8.1 Functionalization of Barium Titanate Microspheres

To chemically attach fluorescent dye molecules and/or proteins to the surface of Mo-Sci glass microspheres, the following step-by-step functionalization procedure was followed.

1. Place the desired size and amount of microspheres in a new 4.0 mL glass vial and cap with a Teflon lined lid.
2. Rinse the spheres in a 10% Contrad 70 Liquid Detergent solution 3 times, rinsing with deionized water in between. ("Rinse" means to sonicate, shake lightly, and vortex while making sure spheres are freely moving within each solvent and solution used.)
3. Complete a final rinse with deionized water.
4. For barium titenate spheres, immerse spheres in H_2O_2 for approximately 10 minutes.
5. Rinse with deionized water. Remove water.
6. Rinse spheres with 3.0 mL of 200 proof ethanol 3 times. Remove ethanol.

7. Rinse spheres with 3.0 mL of toluene, making sure spheres do not stick to the sides of the glass vial. If spheres are adhering to the sides, use a pipette to gently rinse the spheres off the side of the glass and vortex lightly. Remove toluene, add 3.0 new mL of toluene and continue to make sure spheres are mobile. Remove toluene.
8. Prepare a 5% solution of (3-aminopropyl)triethoxysilane (APTES) in toluene.
9. Rotate spheres in 5% APTES in toluene overnight, at least 6-8 hours. Make sure the vial is rotated during the incubation period by utilizing a battery powered rotator, or electric rotator.
10. After rotating overnight, remove mobile spheres and place into a new 4.0 mL glass vial.

To covalently attach an amine terminated dye to the surface of the glass spheres:

11. Rinse spheres in toluene 3 times. Remove toluene.

12. Rinse spheres in 200 proof ethanol 3 times. Remove ethanol.

13. Rinse spheres in 0.1M sodium bicarbonate buffer.

14. Add 10-50 μL of 1 mg/mL Alexa 633 dye (aliquots stored in -80 °C freezer). Be sure to cover the glass vial in foil to prevent photobleaching. Rotate spheres for 1-2 hours.

15. Rinse sphere in 0.1 M sodium bicarbonate buffer to remove unattached dye. Store functionalized spheres in 200 proof ethanol.

Covalently attach antibodies or proteins molecules:

11. Rinse spheres in toluene 3 times. Remove toluene.

12. Rinse spheres in 200 proof ethanol 3 times. Remove ethanol.

13. Rinse sphere in deionized water. Remove water.

14. Rinse spheres in Phosphate Buffer Saline (PBS).

15. Rinse spheres in 6% v/v glutaraldehyde in PBS and rotate for several hours.

16, Rinse spheres in PBS 3 times.

17. Add antibodies or protein (2-10 μg/mL) to attach via surface aldehyde groups. Rotate spheres overnight at 4 °C. Rinse in PBS.

18. Rinse spheres in 0.1 M sodium bicarbonate buffer. Add 10-50 μL of 1mg/mL Alexa 633 dye (aliquots in -80 °C freezer). Be sure to cover the glass vial in foil to prevent photobleaching. Rotate spheres for 1-2 hours.

19. Rinse sphere in 0.1 M sodium bicarbonate buffer to remove unattached dye. Store functionalized spheres in 200 proof ethanol.

20. To block reactive groups on the sphere surface add 3.0 mL of StartingBlock Blocking Buffer and tumble for approximately 15 minutes. Rinse spheres with PBS 3 times.

8.2 Data Analysis Methods and Techniques

8.2.1 Transferring NanoScope Files for Analysis in Excel

When collecting spectra using AFM NanoScope IIIa software, the following procedure can be used to transfer files and analyze the results.

1. Save the spectra file as ACSII text file from AFM NanoScope Software.
2. Transfer the ASCII file to a USB.
3. On your computer, open excel.
4. In a new excel worksheet, select import the data file as a text file.
5. In the open file menu, select show all data types.

6. Select your NanoScope file and use the wizard to import the data.
7. Delete text explaining the capture settings because you are only interested in the intensity values from the original file NanoScope file.
8. Based on the NanoScope settings, such as Scan Size, you can determine your range of data. For example, for a scan size of 350 volts, the entered voltage range would be -175 to 175. Enter the min and max values adjacent to the corresponding intensity values, highlight these cells as well as the blank cells inbetween to fill in values evenly.
9. Use the calibrated wavelength and voltage as shown below in figure 8.1 to convert voltage to wavelength values. Plot wavelength (x) vs. intensity (y).

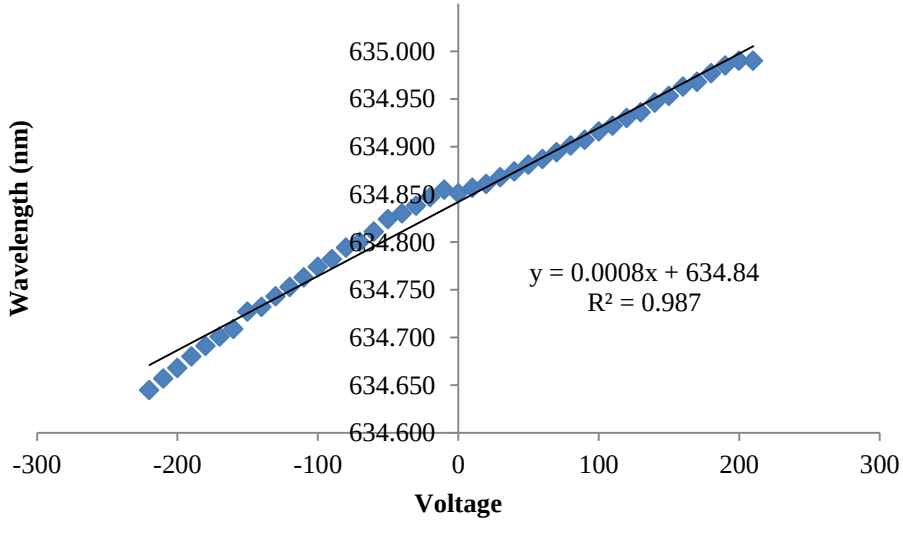

Figure 8.1. Calibration plot for tunable Vortex TLB-6904 laser (Newport Corporation). Wavelength measured using the Burleigh Interferometer.

8.2.2 Analyzing Multiple Resonators Using Image J

The following instructions outline the process used to analyze multiple spheres within a single image using Image J. The process is not limited to this method, but hopefully this outline provides some tips and hints for future lab members to further develop and investigate Image J analysis of multiple microspheres.

Z Project:

(Image> Stack> Z Project)

-DON'T CROP IMAGE prior to analysis

-Select Average Intensity, slice 1-150

-Makes a single image

Threshold:

(Image> Adjust> Threshold)

-Make sure particles are larger than 1 pixel

-Select a section using the shape tools (ex. Circle), then analyze particles

-Makes a binary image

Analyze Particles:

(Analyze> Analyze particles)

-Settings: 0-Infinity, 0.00-1.00, Nothing, X Summarize, X Add to manager, X Exclude on edges, X include holes

-Labels and adds particles to ROI manager

ROI manager:

(Analyze> tools> ROI Manager)

-Add coordinates of good peaks found by plot z axis profiler

-Open plot z-axis profile, select live view

-Select stack image, highlight coordinates in ROI manager, measure and view z-axis profile, keep good spectra, rename to "sphere #"

-Save ROI as a zip file

-More> Multi Measure: spread sheet of all added rectangle areas

-Analyze> Set Measurements> Check Mean Grey Value

-More> Save

Plot Z axis Profile:

(Image> Stacks> Plot Z axis Profile)

-Live button to analyze rectangle areas in real time

-Edit> Options> Profile Plot Options>

-Settings: Check: Interpolate line profiles, draw grid lines, width 450 pixels, height 200 pixels

Time Series Analysis:

(Plugins> Time Series Analyzer V3)

-Highlight all coordinates in ROI

-Select Get Total Intensity

-Transfer table of values to excel for analysis

Open New stack:

-Apply ROI coordinates to new image

-Time Series Analyzer> Get Total Intensity